BARRIERS OF PROTONATION REACTIONS OF ORGANOMETALLICS

Dissertation

for the award of the degree

"Doctor rerum naturalium" (Dr. rer. nat.)

of the Georg-August-Universität Göttingen

within the doctoral program "Chemistry"

of the Georg-August University School of Science (GAUSS)

submitted by

Rene Kevin Rahrt

from Friesoythe

Göttingen, 2023

Thesis Committee

Prof. Dr. Konrad Koszinowski, Institut für Organische und Biomolekulare Chemie, Georg-August-Universität Göttingen, Germany

Prof. Dr. Ricardo Mata, Institut für Physikalische Chemie, Georg-August-Universität Göttingen, Germany

Prof. Dr. Richard O'Hair, School of Chemistry, University of Melbourne, Australia

Members of the Examination Board

Reviewer: Prof. Dr. Konrad Koszinowski, Institut für Organische und Biomolekulare Chemie, Georg-August-Universität Göttingen, Germany

Second Reviewer: Prof. Dr. Ricardo Mata, Institut für Physikalische Chemie, Georg-August-Universität Göttingen, Germany

Further Members of the Examination Board

Prof. Dr. Manuel Alcarazo, Institut für Organische und Biomolekulare Chemie, Georg-August-Universität Göttingen, Germany

Prof. Dr. Dietmar Stalke, Institut für Anorganische Chemie, Georg-August-Universität Göttingen, Germany

Prof. Dr. Martin Suhm, Institut für Physikalische Chemie, Georg-August-Universität Göttingen, Germany

Prof. Dr. Philipp Vana, Institut für Physikalische Chemie, Georg-August-Universität Göttingen, Germany

Date of the Oral Examination: 01.08.2023

Declaration

I hereby declare that I have written the present thesis under the supervision of Prof. Dr. Konrad Koszinowski independently and without impermissible help from other parties. I confirm that I used no other than the herein referenced source materials and aids. No part of the thesis has been submitted for the award of any other degree or diploma prior to this date.

Göttingen, 12.06.2023

_____

Rene Rahrt

Danksagungen

Parts of the results presented in this thesis have been published in:

Gas Phase Protolysis of Trisarylzincate Anions
R. Rahrt, K. Koszinowski, *J. Phys. Chem. A* **2021**, *125*, 51, 10725–107333.

C versus O Protonation in Zincate Anions: A Simple Gas-Phase Model for the Surprising Kinetic Stability of Organometallics
R. Rahrt, K. Koszinowski, *Chem. Eur. J.* **2023**, e202203611.

Parts of the research data presented in this thesis have been published in:

Göttingen Research Online Data Repository (GRO.data), Koszinowski Group Dataverse, Rahrt Dataverse, Protonation of Organometallics Dataverse
R. Rahrt, K. Koszinowski
URL: https://data.goettingen-research-online.de/dataverse/rahrt-01

qmbench – challenges for numerical quantum chemistry, ProtokinX database
R. Mata, A. Poblotzki, A. Knoll, P. Großkopf, B. Hein-Janke, N. Lüttschwager, R. Rahrt, K. Koszinowski
URL: https://qmbench.net/databases/protokinx

Abstract

Protonation reactions are entirely understood for simple organic and inorganic molecules and there are elaborated concepts to describe such acid-base reactions in both the solution and gas phase. For organometallic species, however, there is no such deep understanding. Thus, this dissertation about the barriers of protonation reactions of organometallics applies the concepts and methods of physical organic chemistry to organometallic species to elucidate their intrinsic reactivity towards protonation and assess the effects at play.

For this purpose, mass-selected organometallic species were subjected to ion-molecule reactions with proton donors ROH (R = CF_3CH_2, CF_2HCH_2, CFH_2CH_2, HCO) in a three-dimensional quadrupole-ion trap mass spectrometer at T = (310±20) K. Kinetic measurements of these reactions allowed for the determination of experimental bimolecular rate constants k_{exp}. In addition, the proton-transfer reactions were computed quantum-chemically using DFT (ωB97X-D3/def2-TZVP) and coupled-cluster methods (DLPNO-CCSD(T)/cc-pV[T;Q]Z) and simulated kinetically by carrying out Master-equation calculations based on statistical rate theory. Thereby, the theoretical bimolecular rate constants k_{theo} were obtained. From the interplay of experiment and theory the intrinsic reactivity of the organometallic species towards protonation was inferred. Moreover, the experimental rate constants served as the reference data to benchmark the performance of quantum-chemical methods to predict the barrier heights associated with the protonation of organometallics.

For the example of closed-shell organozincate anions R_3Zn^- (R = Me, Et, aryl) the prototypical reaction mechanism for the protolysis reactions of organometallic species in the gas phase was investigated. For the enthalpy at 0 K, ΔH_0, a double-well potential consisting of three distinct reaction steps was found: first, the formation of the pre-reactive complex, second, the actual proton transfer from the acidic site of the proton donor to the basic site of the organometallic ion and, last, the dissociation of the product complex into the products. The first reaction step could be described fairly well with the capture theory by Su and Chesnavich. The proton transfer was modelled in accordance with classical RRKM theory. The reaction barrier of the proton-transfer step was found to depend on the reaction energy $\Delta_r H_0$, i.e. an increasing exothermicity of the protonation reaction lowers its activation barrier $\Delta H^{\ddagger}_0$. The dissociation of the product complex occurred easily.

By varying the nature of the substituents of the organozincates Et_2ZnX^- (X = H, Et, OH, F, Cl), it was found that such bases X^-, to which Eigen referred as normal (e.g. X = OH), reacted at the collision-rate limit. The reactivity emerges from the formation of hydrogen bonds between the proton donor and acceptor which mediate the proton transfer. In marked contrast, Eigen non-normal bases such as aryl or alkyl moieties (C bases) that are typical in organometallic species react surprisingly slow in proton-transfer reactions. Despite their higher basicity, such bases feature unusually high intrinsic barriers; i.e., their kinetic behavior and thermochemical properties are opposed. The finding could help to understand why some organometallic transformations such as Negishi cross coupling are feasible within protic media.

As the agreement between the measured experimental rate constants k_{exp} and the predicted theoretical rate constants k_{theo} was excellent, the quantum-chemical calculations of the protonation barriers were found to achieve chemical accuracy.

Moreover, the protolysis reactions of the open-shell (S = 2) organoferrate anions R_3Fe^- (R = Ph, Mes) were investigated within the Fe-MAN challenge which stands for "Ferrates – Microkinetic Assessment of Numerical quantum chemistry". From the poor agreement of the experimental and theoretical rate constants, k_{exp} and k_{theo}, it became evident that usual quantum-chemical methods (e.g. PNO-LCCSD(T)-F12/def2-TZVP//ωB97X-D3/def2-TZVP) are still challenged with the accurate prediction of barrier heights for such open-shell organometallic systems. Thus, more experimental reference data for future benchmarking endeavors is required.

List of abbreviations

Abbreviation	Meaning
2D	Two-dimensional; two dimensions
3D	Three-dimensional; three dimensions
AC	Alternating current
CC	Coupled cluster
CCSD(T)	Coupled cluster with single, double and perturbative triple excitation
CRM	Charged residue model
DC	Direct current
DLPNO	Domain-based local pair natural orbital
DOF	Degree of freedom
EDG	Electron-donating group
EGME	Energy-grained Master equation
EI	Electron ionization
ESI	Electrospray ionization
EWG	Electron-withdrawing group
FCI	Full configuration interaction
FT	Fourier transform
IEM	Ion evaporation model
ICR	Ion cyclotron resonance
ILT	Inverse Laplace transform
IMR	Ion-molecule reaction
GA	Gas-phase acidity
GB	Gas-phase basicity
GD	Glow discharge
LFER	Linear free energy relationship
m/z	Mass-to-charge (ratio)
ME	Master equation
MS	Mass spectrometry
MS^1	Mass spectrometry with 1 mass-spectrometric step
MS^n	Spatial or temporal tandem mass spectrometry with n steps
NPA	Natural population analysis
PA	Proton affinity
PCET	Proton-coupled electron transfer
PES	Potential-energy surface
QCC	Quantum-chemical calculation
QIT	Quadrupole ion trap
RF	Radio frequency
RRK	Rice, Ramsperger, Kassel; statistical rate theory based on the model of Rice, Ramsperger and Kassel
RRKM	Rice, Ramsperger, Kassel, Marcus; RRK statistical rate theory extended by the theory of Marcus
TS	Transition state; transition structure
TST	Transition state theory

Table of contents

1 Introduction

1.1 Motivation

1.1.1 Protonation reactions in chemistry

Protonation, i.e. the attachment of a proton to another atom, is one of the simplest processes in chemistry. Protonation takes place in many synthetically relevant reactions. Sometimes, it is desired in order to mediate chemical reactions by means of acid-base catalysis. In other cases, proton-transfer reactions are unwanted as they hamper or even prevent chemical reactions.

Chemists regularly add acids to their reaction mixtures to facilitate reactions. One classical textbook example is the acid-catalyzed ester hydrolysis, in which the acid protonates the oxygen atom of the carbonyl group, thereby increasing the electrophilicity of the carbonyl carbon atom. In the next step of the reaction, the carbonyl carbon is attacked by water to form a cationic tetrahedral intermediate. After the proton is shifted, the alcohol is released. At last, the proton attached to the carbonyl oxygen is abstracted, concluding the catalytic reaction. Another example is the addition of water or alcohols to alkenes. The protonation of one vinylic carbon atom activates the substrate, so that a carbenium species forms. Thereafter, the nucleophile attacks at the positively charged carbon to give the protonated product. Deprotonation is the final step closing the reaction.[1]

In organometallic chemistry, protonation reactions are an ambivalent phenomenon. On the one hand, they can be necessary in catalytic reactions. For example, the Ackermann group described the C–H activation of arenes and alkenes by cobalt(III) catalysts. Therein, proto-demetalation is required in the last step of the reactions to re-generate the catalytically active species.[2]

On the other hand, organometallics which often feature basic substituents (e.g. alkyl or aryl moieties) must be handled under the strict exclusion of water or other protic substances in many cases. Otherwise, their protolysis will render the wanted reaction impossible. Recent advances, however, show that some organometallic reactions are feasible even within protic media.[3–6] For instance, Capriati and co-workers reported on successful Negishi cross-coupling reactions using organozinc compounds under aerobic and protic conditions. Apparently, the transmetalation reaction was not prevented by the protolysis of the organozinc species.[7]

Given that protonation reactions are so important in chemistry, they have been the topic of scientific investigations for a long time. By studying protonation and deprotonation reactions, in other words acid-base chemistry, for more than two centuries, researchers discovered many principles in physical and physical organic chemistry. There, simple inorganic and organic molecules were studied.[8]

Given the recent interest in the protonation of organometallics, those concepts and methods will be applied to this research topic.

1.1.2 Acids, bases and their reactions

1.1.2.1 Protonation reactions in solution

Chemists knew that substances can react acidic or alkaline since the 18th century. However, they held different views about the reasons of the observed reactivity. It was Arrhenius who proposed a first unifying description of acids and bases in 1887. He stated that, in aqueous solution, acids produced *hydrogen ions*. In this picture, *hydrogen ion* included all kinds of hydrated hydrogen ion containing species. According to Arrhenius, bases were substances that gave hydroxide ions in solutions of water. In the neutralization reaction, hydrogen ions and hydroxide ions reacted with each other and water formed.[8–10] Later, the pH was introduced as a measure for the activity of hydrogen ions $a(H^+_{(aq.)})$ in aqueous solution (Equation 1):[9]

$$\text{pH} = -\log_{10} a\left(H^+_{(aq.)}\right) \qquad\qquad \text{Equation 1}$$

However, as the Arrhenius concept is limited to water as a solvent, a more general characterization of acids and bases became necessary.[8–10]

In 1923, Brønsted and Lowry defined acids to be proton donors and bases to be proton acceptors. In this definition, the proton referred to the actual H^+ ion and no longer to hydrogen ions in various forms dependent on the solvent. Within the Brønsted-Lowry concept, acid-base reactions are processes in which a proton is transferred from the acid to the base. The acid AH donates the proton to the base B giving the corresponding base A^- and acid BH^+, respectively (Scheme 1).[8,9,11]

$$\text{AH} + \text{B} \rightleftharpoons \text{A}^- + \text{BH}^+$$
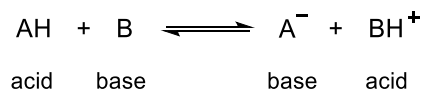
acid   base   base   acid

Scheme 1: Acid-base equilibrium according to the Brønsted-Lowry concept. The proton, H^+, is transferred from the proton donor (acid) AH to the proton acceptor (base) B.

Within the Brønsted-Lowry concept, the acidity of an acid AH is described by its tendency to donate protons. In solution, one can quantify the acidity via the dissociation equilibrium of the acid (Scheme 2).[9]

$$\text{AH} + \text{solvent} \rightleftharpoons \text{A}^- + \text{solventH}^+$$
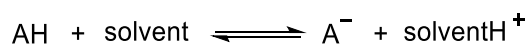
Scheme 2: Dissociation equilibrium of the acid AH in solution. The extent of the dissociation characterizes the acidity of AH.

Based on the law of mass action and the activities *a* of reactants and products, the acidity is measured as the dissociation or acid constant K_a if the activity of the solvent is included therein (Equation 2):

$$K_a = K \times a(\text{solvent}) = \frac{a(\text{solventH}^+) \times a(A^-)}{a(\text{AH})} \qquad\qquad \text{Equation 2}$$

More often, the acidity is given in terms of the pK_a, which is the negative decadic logarithm of K_a. The lower the value of the pK_a is, the more acidic is the proton donor. Analogously, the basicity can be quantified via the base constant K_b and pK_b.[9]

With his new concept of acids and bases, Brønsted revisited ideas of earlier findings of Arrhenius and Ostwald who found that, in cases of acid catalysis, the catalytic effect of an acid somehow depended on its acidity. In lack of a suitable concept of acids and bases, they were not able to quantify that correlation. However, Brønsted and Pedersen achieved exactly that in 1924, when they published their study on the catalytic decomposition of nitramide. Therein, they proposed the so-called Brønsted relation or Brønsted catalysis law. The catalytic rate constant k depends on the dissociation constant $K_{a,AH}$ with the sensitivity parameter α ($0 < \alpha < 1$). Later, statistical corrections with regards to the number of acidic and basic sites, p and q, respectively, were added. For acid catalysis, the Brønsted relation is formulated in Equation 3 and visualized in Figure 1. A similar relationship is possible for base catalysis.[11–13]

$$\log \frac{k}{p} = \alpha \times \log \frac{q \times K_a}{p} + \text{constant} \qquad \text{Equation 3}$$
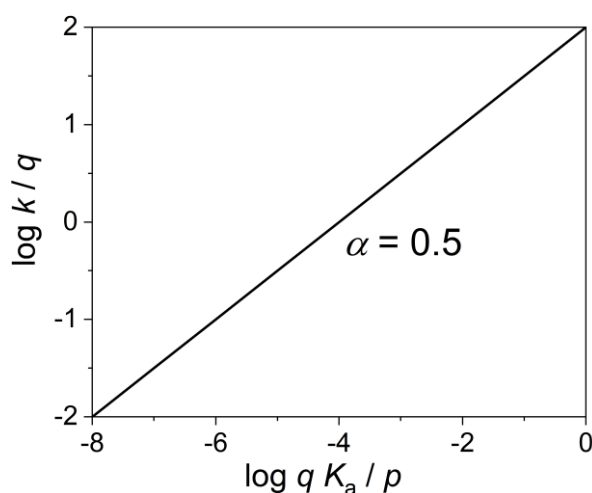
Figure 1:   Brønsted relation for an acid-catalyzed reaction. The logarithmic rate constant of the reaction is linearly dependent on the logarithmic acidity constant of the added acid. The Brønsted parameter α is defined as the slope and indicates the correlation of the rate constant with the dissociation constant. According to reference [14].

In the beginning of the 1930s, chemists were aware of the connection between the thermochemistry and the kinetics of chemical reactions. Phenomenologically they found that, within one set of reactions, increasing exothermicity (endothermicity) accelerates (decelerates) the reaction process. This knowledge was later systematized into the Bell-Evans-Polanyi principle and the Hammond-Leffler postulate. The former states that the activation barrier for a reaction depends on the reaction energy of the same reaction. The latter generalizes that principle and finds that transition structures in energetic proximity to the reactants (products) also resemble the reactants' (products') geometry. Such transition states were classified as early (late) as they occur in the beginning (end) of the reaction process.[14–17]

Based on the observations for one type of reaction, Hammett stepped on new ground by correlating the equilibrium constants (rate constants) of <u>one</u> set of reactions with the equilibrium constants (rate constants) of *another*. He studied the alkaline hydrolysis of *para*- and *meta*-substituted ethyl benzoates and found a linear dependence of the logarithmic reaction rate on the logarithmic acidity constant of the corresponding benzoic acid. Hammett systematized those results into the Hammett equation given in Equation 4:

$$\log\frac{k_X}{k_H} = \rho \times \log\frac{k_X^0}{k_H^0} = \rho \times \sigma \qquad \text{Equation 4}$$

k_X and k_H are the rate constants for the hydrolysis reactions of the X-substituted and H-substituted benzoates. k_X^0 and k_H^0 are the rate constants of the reference reaction, which is the dissociation reaction of the corresponding carboxylic acids in water at 298 K. The proportionality factor ρ is a measure of how sensitive the (hydrolysis) reaction is towards the change in the acidity of the benzoic acid derivatives.[15,18–20]

The logarithm of the ratio of the equilibrium constants for the dissociation reactions, K_X^0/K_H^0, was defined as the Hammett parameter σ, which is a specific value for each *meta*- or *para*-substituent X. The Hammett parameter quantifies the extent of the dissociation of the substituted benzoic acid derivative relative to the reference system benzoic acid. Thus, substituents, which increase the acidity of the substituted derivative over that of the reference, give positive Hammett parameters ($\rho > 0$). And substituents that decrease the relative basicity of the substituted derivative have negative Hammett parameters ($\rho < 0$). In other words: The value of the Hammett parameter correlates with the ability of substituents to withdraw or donate electron density. Electron-withdrawing groups (EWG) such as –Cl, –CF$_3$ or –NO$_2$ show positive Hammett parameters and electron-donating groups (EDG) such as –NMe$_2$, –OMe or –Me negative values.[14–16,21,22]

The Hammett equation is one major cornerstone of physical organic chemistry and built the fundament for many more such linear free-energy relationships (LFER). As the Hammett parameter ascribes to the effect of a certain structural motif on the reactivity of the molecule, the Hammett equation is also the starting point of structure-reactivity relationships.[14–16]

The next stage in the investigation of protonation reactions was largely carried by the research of Eigen in the 1960s. Amongst other, he studied the nature of the hydrated hydrogen ion ($H^+_{(aq.)}$) in aqueous solution and found it to be in the form of the hydronium ion H_3O^+ (primary hydration) or $H_9O_4^+$ ($H_3O^+ \cdot 3\ H_2O$; secondary hydration). These Eigen ions, in conjunction with the Zundel cation ($H_5O_2^+$, $H_3O^+ \cdot 1\ H_2O$), supported the Grotthuss hypothesis of the "proton jumping" mechanism that rationalized the unusually high electrical conductivity of protons in water.[23,24]

Furthermore, Eigen invented the method of relaxation spectrometry and used it for the kinetic study of "immeasurably fast reactions"[25] of acids and bases. For his invention and discoveries, Eigen was awarded the Nobel prize in 1967.[25] Up to then, chemists were restricted in their kinetic studies of protonation reactions because they could not resolve the time dependence for fast reactions approaching the diffusion limit (bimolecular rate constant $k \approx 10^{10}\ M^{-1}\ s^{-1} = 10^{-11}\ cm^3$ molecule$^{-1}\ s^{-1}$) and, thus, could only measure slower reactions of rather weak acids with rather weak bases. By applying the new relaxation measuring procedures, it became feasible to determine rate constants of a much broader range up to the diffusion limit.[23,25–27]

Eigen classified two types of acids and bases in aqueous solution. The first kind is referred to as "normal" acids and bases. These systems are characterized by the proton transfer being diffusion controlled if the pK_a difference is large enough. Once the acid and base are sufficiently close to one another, the proton is transferred instantaneously. Such "normal" acids and bases usually feature free electron pairs and protic hydrogen atoms and, thus,

form hydrogen bonds. These strong intermolecular interactions promote the proton transfer. Typical "normal" acids and bases have –OH, –NH$_2$ or –SH functional groups.[23,25–27]
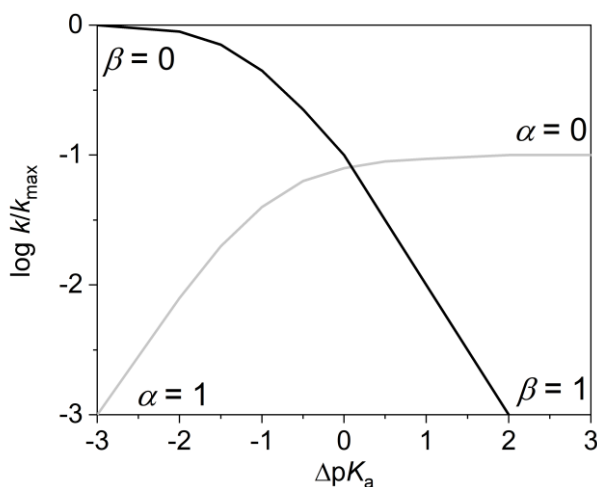

Figure 2:   Eigen plot in normal acid-base systems for neutral acids AH and neutral bases B (gray line) and charged acids BH$^+$ and bases A$^-$ (black line). Correlation of the logarithmic normalized rate constant k/k_{max} with ΔpK_a = $pK_{a,acceptor}$−$pK_{a,donor}$ where k_{max} corresponds to the rate constant at the diffusion limit. For large pK_a differences, the logarithmic rate constant depends linearly on ΔpK_a and the Brønsted parameters α and β are 1 if the rate constant is not yet governed by the diffusion control where α and β converge towards 0. According to references [23,27].

The ideal correlation of the rate constant k and the difference in the pK_a values (ΔpK_a) for normal acid-base systems is given in Figure 2. Such Eigen plots show a linear free energy relationship (LFER) between the rate constant for the proton transfer k and the thermodynamic driving force ΔpK_a if the rate constant is not yet governed by the diffusion limit k_{max}. In the former regime, the Brønsted parameters α and β are equal to 1 whereas they converge towards 0 in the latter. Additionally, the Eigen plot reveals that the proton transfer reactions involving two charged species (acid BH$^+$ and base A$^-$; black line) are typically faster than the reaction of two neutral species (acid AH and base B; gray line) as a consequence of the stronger intermolecular interactions.[23,25–27]

The second class of acid-base systems differ in that their protonation reactions are significantly slower than the diffusion limit indicating that not the encounter of the reactants but the actual proton transfer is the rate-limiting step. In this regard, they are considered "non-normal". Their low reactivity towards protonation is rationalized by the missing ability to form hydrogen bonds. Many C–H acids and C bases belong to this class.[23,25–27]

On the grounds of Brønsted's, Hammett's and Eigen's work, Jencks studied the mechanisms of general acid-base catalysis of chemical and enzymatic reactions. In more detail, he was interested in distinguishing whether reactions occur in a stepwise or concerted fashion. Based on the idea of More O'Ferall, Jencks visualized the reaction progress in two-dimensional (2D) contour plots later known as More O'Ferall-Jencks diagrams. In the case of an acid-catalyzed nucleophilic addition to a carbonyl center, three borderline mechanisms for the reaction initiation are conceivable (Figure 3):[28]

A–H

A⁻

$-C-$ with O⁻, Nu⁺

H–O, $-C-$, Nu⁺

C–Nu (vertical axis)

X–H–A (horizontal axis)
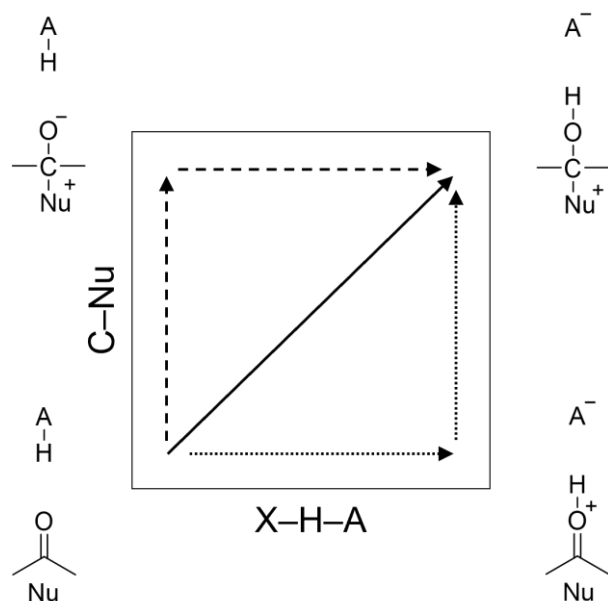
A–H

A⁻

O (carbonyl), Nu

H–O⁺, Nu

Figure 3: Schematic More O'Ferall-Jencks diagram for the acid-catalyzed addition of a nucleophile to a carbonyl center. Two stepwise (dashed and dotted line) and one concerted (solid line) mechanisms are conceivable. See text for more information. According to reference [28].

- Stepwise 1 (dotted line): The acid will first protonate the carbonyl oxygen, so that an ionic intermediate forms. In the second step, the nucleophile will attack the protonated substrate at the carbonyl center and form the new bond.
- Stepwise 2 (dashed line): The nucleophile first attacks the substrate at the carbonyl carbon giving a zwitterionic tetrahedral intermediate. Only afterwards, the acid protonates the carbonyl oxygen atom.
- Concerted (solid line): The protonation of the carbonyl oxygen and the nucleophilic attack at the carbonyl carbon proceed simultaneously.

Jencks postulated that the concerted mechanism would only occur if it is energetically more favorable than the stepwise ones. The prerequisite would be that the reactive site undergoes a large change in its acidity (basicity) which renders an unfavorable proton transfer favorable.[28,29]

Over the course of the next years, Jencks deepened his research about reaction mechanisms in terms of their transition structures. Specifically, he characterized transition states within the framework of the Bell-Marcus-Hammond-Polanyi-Thornton-Leffler (Bema Hapothle) effects and he coined the term of the "imbalance" of transition structures. Such imbalances occur in transition state, in which two (or more) processes with regard to the reaction coordinate take place, but are out of synchronization. Structure-reactivity relationships often fail in such cases.[28,30]

The best known example of an imbalanced transition state was found for the so-called nitroalkane anomaly. For a series of *para*- and *meta*-substituted arylnitromethanes the rates of deprotonation by different bases were measured in solution. The Brønsted β value was determined by changing the basicity of the proton acceptor (different substituents of the base). In a similar manner, the Brønsted α value was obtained from varying the acidity of the proton donor (different *para*- and *meta*-substituents at the aryl moiety of the acid). It was found that the Brønsted β and α value deviate from each other significantly. The observed behavior of the C–H acids drastically differed from that of Eigen normal acids.[31] Those findings were explained by the imbalance of the transition state: The transfer of the

proton (geometric change) is faster than the delocalization of the negative charge into the nitro group (electronic change).[28,32]

Bernasconi found the imbalance of transition states in proton-transfer reactions involving C–H acids to slow down the reaction rate. In his "principle of non-perfect synchronization",[32] he connected the lack of synchronization of concurrent processes in the transition state to high intrinsic barriers.

The concept of intrinsic barriers stems from Marcus' theory of electron transfer,[33] which had been applied to proton-transfer reactions earlier.[34,35] Within the Marcus theory, the activation barrier for the electron (proton) transfer $\Delta G^{\ddagger}$ depends on the thermochemical driving force $\Delta_r G$ as well as the reorganization energy λ (Equation 5):[33]

$$\Delta G^{\ddagger} = \frac{(\Delta_r G + \lambda)^2}{4\lambda} \qquad\qquad \text{Equation 5}$$

As such, the Marcus theory demonstrates the connectivity of the reaction kinetics and thermochemistry. There are two regimes: the Marcus-normal regime, in which the activation barrier decreases quadratically with increasing exothermicity ($-\Delta_r G < \lambda$), as well as the Marcus-inverted regime wherein the barrier heights are again increasing for very high reaction energies ($-\Delta_r G > \lambda$). Although, the dependence of $\Delta G^{\ddagger}$ on $\Delta_r G$ is *quadratic*, the relation is the basis of many *linear* free energy relationships because for small energy changes a straight line is a good approximation to the parabola.

The intrinsic barrier is defined as the activation energy that is associated with a thermoneutral elementary reaction. Thus, it is an inherent property of a chemical species towards a certain type of reaction. High intrinsic barriers result in low intrinsic rate constants and, thus, often cause low intrinsic reactivity.[33,36]

Bernasconi's principle states that intrinsic barriers are increased if factors, which stabilize the products, develop late and/or factors that stabilize the reactants are lost early over the course of the reaction. Such stabilizing (destabilizing) factors include resonance effects, hydrogen bond interactions or solvation.[32,37–39]

Current research, especially in the context of proton-coupled electron transfer (PCET) reactions, aims to include the quantum nature of protons into the full picture of proton transfer. For instance, Costentin and Savéant analyzed self-exchange proton-transfer reactions at carbon, nitrogen and oxygen sites. They found that the non-adiabatic character of the proton-transfer step causes the exceptionally low intrinsic reactivity of carbon acids and bases towards protonation. Thus, the reaction rate of C protonation is dominated by the proton tunneling through the activation barrier. This is in distinct contrast to Eigen normal acids and bases with nitrogen and oxygen donor and acceptor sites as their protonation (deprotonation) proceeds adiabatically and without major tunnelling. The authors re-connect these findings back to the concept of imbalanced transition states by Jencks and Bernasconi.[40,41]

1.1.2.2   Protonation reactions in the gas phase

The study of protonation reactions in solution gave much knowledge about acid-base chemistry and proton transfer. If one aims to investigate the peculiar reactivity of one specific species without any solvation or aggregation effects, i.e. its intrinsic reactivity, studies in the gas phase are necessary. Researchers usually realize better control over the species of interest and the reaction conditions in gas-phase experiments. Often, techniques of mass spectrometry (MS) are used in such studies as they allow for the selection of specific chemical species in the form of their ions via their mass-to-charge (m/z) ratio.[42,43–45] 1

Early studies focused on the thermochemical properties of gaseous acid-base reactions. In order to characterize the strength of an acid as a proton donor, the gas-phase acidity (GA) was defined as the Gibbs energy, $\Delta_r G°$, for the dissociation reaction of the acid AH in the gas phase under standard conditions (Scheme 3).[13,46]

$$AH \longrightarrow A^- + H^+$$
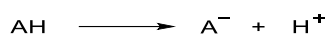
Scheme 3:   Dissociation of the acid AH in the gas phase. The Gibbs energy associated with the reaction is defined as the gas-phase acidity.

In a similar manner, the gas-phase basicity (GB) is defined as the negative of *the Gibbs energy*, $\Delta_r G°$, for the protonation of the base B. Another important measure is the so-called proton affinity (PA) which is the negative of the *enthalpy* change, $\Delta_r H°$, of the afore-mentioned reaction (Scheme 4).[13,46]

$$B + H^+ \longrightarrow BH^+$$

Scheme 4:   Protonation of the base B. The reaction poses the reference for the definition of the gas-phase basicity which is the negative of the Gibbs energy of the protonation reaction.

Hundreds of reactions were probed and lots of thermochemical data were acquired. Many of those are nowadays curated by and provided through the database of the National Institute of Standards and Technology (NIST) of the United States of America.[47]

For decades, chemists have been investigating the mechanisms and dynamics of proton-transfer reactions in the gas phase. Often, protonation was studied alongside nucleophilic substitution reactions, which is the favorite model reaction of gas-phase physical (organic) chemists.

Bierbaum and DePuy investigated the reactions of organic anions with neutral substrate molecules in the gas phase. From such ion-molecule reaction (IMR) experiments, they determined various thermochemical properties of multiple chemical species, e.g. alkoxides or the deprotonated anions of nitroalkanes. Moreover, they probed the association of the reactants as well as the lifetime of thus formed encounter complexes in ion-molecule reactions involving proton transfer in hydrated ions.[48,49]

Since the late 1970s, Brauman conducted studies about the proton-transfer reactions of organic anions. In addition to oxygen acids and bases, he probed the reactivity of C–H acids (and C bases) such as alkanes, arenes and dienes (and their corresponding anions). His findings were groundbreaking in many ways. First, Brauman confirmed that the reaction profile (or reaction pathway), i.e. the 2D representation of the potential-energy surface

---

1 For more information about the various mass-spectrometric methods used, consult section 1.2.1.

(PES) along the reaction coordinate, poses a double-well potential in terms of the enthalpy, ΔH, as it does for the nucleophilic substitution. In the beginning, the reactants form an encounter or pre-reactive complex. Next, the proton is transferred and the reaction proceeds from the pre-reactive to the product complex via the transition state (TS) which is associated with the central barrier $\Delta H^{\ddagger}$. Finally, the product complex dissociates into the products. Protonation reactions typically were either thermoneutral ($\Delta_r H = 0$) or exothermic ($\Delta_r H < 0$) (Figure 4).[50]
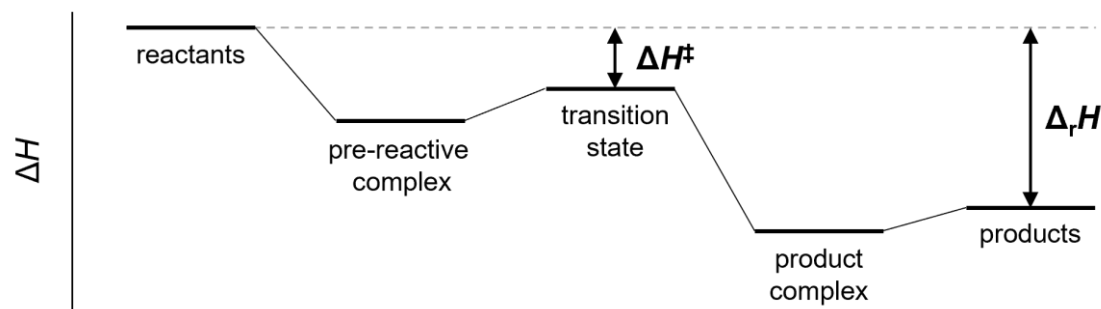

Figure 4: Double-well potential of a proton-transfer reaction in the gas phase.

Further, Brauman and Lim extensively modelled the kinetics of such proton-transfer reactions by applying the statistical rate theory according to Rice, Ramsperger, Kassel, and Marcus (RRKM) and achieved sufficient agreement between experimental and theoretical rate constants. Brauman and coworkers corroborated their approach by conducting state-dependent kinetic studies. The rates of protonation reactions were found to depend on the translational, rotational and electronic state of the reactants.[51–55]

Last, Brauman's research substantiated Eigen's terms of normal and non-normal acids and bases. The proton transfer between alcohols and alkoxides (normal acids and bases) was found to proceed at the collision rate limit (bimolecular rate constant $k \approx 10^{-9}$ cm^3 molecule^{-1} s^{-1}).[56] In distinct contrast, protonation reactions featuring C–H acids or C bases (non-normal acids and bases) occurred significantly slower.[53,57,58] In this regard, Farneth and Brauman elaborated:

> "As suggested by solution results, there may be a substantial 'intrinsic' barrier to proton transfers involving delocalized ions [carbanions; note from the author], which results from loss of resonance energy in the transition state due to a requirement for charge localization. This barrier can be circumvented if proton transfer can occur without disruption to the delocalized system, as for example to oxygen lone pairs. This picture is consistent with solution-phase observations of fast proton transfers to oxygen, but slow transfers to carbon in enolate anions, even though the thermochemistry favors carbon protonation."[57]

Many of the aforementioned results are not specific for anions, but were also found in cationic systems as demonstrated by Uggerud. He investigated the reactivity of (hydrated) organic cations towards protonation and nucleophilic substitution in the gas phase.[44,59]

Gronert expanded the scope of proton donors and acceptors for gas-phase ion-molecule reactions. Apart from oxygen and carbon acids and bases, he also studied the intrinsic reactivity of acids and bases featuring hydrogen, nitrogen, fluorine, silicon, phosphorus, and chlorine sites. Mostly from theoretical investigations of (near-)identity proton-transfer reactions employing quantum-chemical calculations (QCC) and structure-reactivity relationships, Gronert determined the intrinsic barriers for proton transfer involving those acids and bases. He found that the potential-energy surfaces for non-identity protonation reactions can be represented sufficiently well by the hybridization of the corresponding

identity reactions, i.e. the PES of non-identity reactions can be obtained from the weighted average of the two matching identity reaction profiles. For some cases, driven by the exothermicity of the reaction, the central barriers become vanishingly small and, so, the double-well potential changes into a one-well potential. Gronert moreover discovered that the intrinsic barriers for second-row elements (Si, P, Cl) are larger than for first-row elements (N, O, F) and that the intrinsic barriers for carbon acids and bases are anomalously high.[60–63]

Following up on his solution-phase results, Bernasconi applied his principle of non-perfect synchronization to protonation reactions in the gas phase. He performed quantum-chemical calculations for the proton transfer from and to a broad range of carbon acids and bases featuring several functional groups and structural motifs. In many cases, resonance effects were found to be the major contribution to the transition state imbalance causing exceptionally high intrinsic barriers.[64–68]

Over the course of the last two decades, the detailed understanding of gas-phase reaction dynamics progressed vastly. Most of the development was achieved for nucleophilic substitutions featuring reactants with few atoms. However, the methodologies developed for these systems are likely to be applied to proton-transfer reactions in the future. For example, Wester studied the dynamics of gaseous anions reacting with neutral substrates in both experiment and theory. He advanced the kinetic modelling beyond statistical rate theory by performing trajectory calculations on highly accurate potential-energy surfaces. Thus, non-statistical behavior was included into the calculation of rate constants.[69,70]

1.1.3 Protonation of organometallics

As is apparent from both solution- and gas-phase studies, carbon is assigned a special role in proton-transfer reactions. C–H acids (C bases) possess remarkably high intrinsic barriers and, thus, the deprotonation (protonation) of them is unusually slow in comparison to acids (bases) featuring reactive sites based on, for instance, nitrogen or oxygen. With the words of Eigen, carbon acids and bases do not behave normally. But how is the situation for organometallics, in which C bases are present in the form of stabilized carbanions bound to a metal center?

Whereas the protonation of simple inorganic and organic molecules had received much attention over the last century, the reactivity of organometallic compounds towards protonation was investigated with less intensity. While the former studies focused on the details of the physical chemistry at play, the latter investigations were often carried out just to probe the reactivity in a qualitative or semi-quantitative manner.

In solution, chemists mostly investigated organometallic compounds featuring hydride, carbonyl or alkyl/aryl substituents as they are of most synthetic relevance (or were at that time). All residues reacted in the expected fashion.

The addition of an acid to metal hydrido complexes resulted in the protonation of the hydride and the release of H_2. At low temperatures, the newly formed dihydrogen was found to reside at the metal center and, so, the protonation reaction was reversible.[71,72] Further experiments were performed with metal carbonyl and acyl complexes. In such species, the proton was either attached to the carbonyl oxygen atom or the corresponding hydrido carbonyl complex formed.[73,74] Upon treatment with acids, metal alkyl/aryl complexes were

protolyzed, i.e. the carbon moiety was protonated and the respective alkane/arene released.[72,73,75]

Gas-phase investigations of the reactivity of organometallics towards proton transfer were largely realized by mass-spectrometric techniques and, partly, in conjunction with computational methods.[2] In the 1970s, Beauchamp studied the protonations of metallocene and carbonyl complexes. Although, he determined their rate constants and gas-phase basicities, the protonation site and mechanism could not be elucidated.[76–78]

Triggered by major advances in mass spectrometry, the preparation and characterization of gaseous organometallic ions became much more feasible. Consequently, a lot of studies on the behavior of organometallic species towards protonation were conducted. In this context, special mention should be made of O'Hair's work. Between 2003 and 2021, O'Hair and coworkers published numerous papers in which proton-transfer reactions involving various organometallic ions are described. Often, the reactions of alkyl/aryl metalates with water (or an alcohol) were analyzed. The recurrent reaction scheme was the protolysis of the alkyl/aryl substituent to give the corresponding hydroxide (or alkoxide)-containing metalate and the alkane/arene (Scheme 5).[79–81]

$$L_nMR^- + H_2O \longrightarrow L_nM(OH)^- + RH \qquad R = alkyl, aryl; L = ligand$$
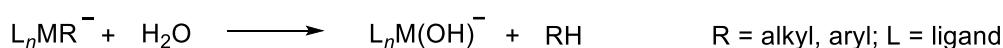
Scheme 5: Typical protolysis of alkyl/aryl metalate by water in the gas phase. Water protonates the alkyl/aryl substituent. As a result, the alkane/arene forms and the hydroxide remains attached to the metal center.

Additionally, metal hydride complexes were probed and, in line with expectations, the hydride protonation was observed.[82] Moreover, the protolysis reactions of vanadium oxo species with methanol were probed which resulted in the release of water.[83]

---

[2] The experimental and computational methodologies will be elaborated on in section 1.2.

1.2   Methods

1.2.1   Mass spectrometry

Mass spectrometry (MS) is an analytical technique to study chemical species. As it was used as the main experimental method for this dissertation, it will be elaborated on below. This section is largely based on the textbook by Gross.[84]

In MS, analytes are ionized and transferred into the gas phase. The gaseous ions are then investigated based on their mass-to-charge (m/z) ratio. The m/z ratio gives information about the elementary constitution of the analyte. More sophisticated MS experiments allow for the insight into the structure of the analytes. MS is also a powerful tool to probe the intrinsic reactivity of the analytes as it allows for the selection of a specific chemical species via its m/z ratio. This mass selection is crucial to determine whether the observed reactivity does stem from the analyte itself or merely results from environmental effects such as solvation, aggregation or chemical equilibria. The latter point is especially relevant for the investigation of organometallics as these species usually are involved in complex Schlenk-type equilibria.[84,85]

Mass spectrometers generally consist of three elementary components: the ion source, the mass analyzer and, finally, the detector. The ion source produces the analyte ions which are analyzed for their m/z ratio in the mass analyzer. Eventually, the analyte ions reach the detector that transforms their charge into an electric current. These signals are processed in a computer to give the mass spectrum which is the plot of the absolute or relative signal intensity against the m/z ratio.

Mass spectrometers are usually classified based on the ion source as well as the mass analyzer. Given the scope of this dissertation, the elaborations on mass spectrometry shall be limited to the ion sources and mass analyzers that were common in the study of protonation reactions.[84]

1.2.1.1   Ion sources and ionization methods

There are dozens of different ionization method in MS. Typically, gaseous ions for protonation studies were prepared by electron ionization, glow discharge and electrospray ionization.

Electron ionization (EI) is the oldest ionization methods in mass spectrometry and pioneered the broad application of mass spectrometers in chemical analytics in the 20th century.[84] In the research of gas-phase protonation reactions, it was used, for instance, by Beauchamp for his studies on metallocenes and carbonyl metal complexes in the 1970s.[76–78,86]

In electron ionization, high-energy electrons (typically 70 eV) are produced which bombard the gaseous sample in the ion source. This collision leads to the explusion of an electron from the analyte M and, thereby, produces positively charged analyte ions M[+]. Often, the analyte ion M[+] dissociates into smaller fragments m_i^+ because of the excess energy that was introduced during the impact (Scheme 6). Therefore, EI is considered a so-called "hard" ionization method.[84]

$$M + e^- \longrightarrow M^+ + 2\,e^- \longrightarrow m_i^+ + 2\,e^-$$
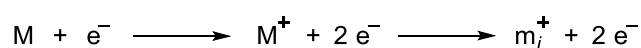
Scheme 6:   In electron ionization, fast electrons collide with the analyte molecule M and give positively charged analyte ions M[+] and its fragments m_i^+.

The very frequent fragmentation of the analyte is both advantageous and disadvantageous at the same time. On the one hand, it helps to elucidate the structure of the analyte and allows for the determination of fingerprint fragments to compare to MS libraries, but, on the other hand, it also prevents the analyte to be studied in its intact form.[84]

Electron ionization bears further advantages and disadvantages. Another benefit of EI is its sensitivity, i.e. even small amounts (or low concentrations) of the analyte are sufficient to produce detectable ion intensities. However, as the sample needs to be gaseous, the applicability of EI is limited to gases and volatile substances. The sample requirement for gases makes EI prone to various kinds of sample introduction. One of the most frequent is the connection of an EI mass spectrometer to a gas chromatograph.[84]

Another ion source that was employed in the context of gas-phase protonation reactions is the glow discharge (GD) source. During the 1980s, Bierbaum and DePuy made extensive use of this hard ionization method.[49,87] As there are multiple variants of the method throughout the history of glow discharge, only the working principle is explained.

The ion source is filled with Ar and charged with the analyte. By the application of an electric field (few mA; 500 to 2000 V), the argon is discharged and, so, a low-energy plasma forms which serves as the source of primary ions Ar^+, excited atoms Ar^* and electrons e^-. These particles undergo reactions with the analyte and in various secondary processes, such as electron ionization or charge transfer, the analyte is ionized. Since the region of the gas discharge is called "afterglow" due to the characteristic emission of the excited argon atoms, the GD ionization is also referred to as "afterglow" method.[84]

The GD ion source is relatively universal for a broad range of samples and easy to maintain. However, it tends to give isobaric contaminations in the mass spectrum. In order to overcome this issue, GD ion sources commonly are coupled to high-resolution mass analyzers. In the past, they were often connected to magnetic sector-field or ion cyclotron resonance mass analyzers.[84]

With the afore-mentioned ionization the scope of chemical species under scrutiny in gas-phase protonation reactions was limited to stable and small inorganic and organic molecules. Since the late 1990s and early 2000s, electrospray ionization (ESI) allowed for great advances in this regard. ESI is a "soft" ionization technique and, with its advent, it became more and more feasible to produce intact gaseous ions of less stable analytes such as organometallics.[84,85] [3] For instance, O'Hair and co-workers routinely applied ESI for the experiments on proton-transfer reactions of organometallic species in the gas phase. They electrosprayed precursor ions and subjected them to gas-phase fragmentation to produce reactive organometallic species which underwent ion-molecule reactions with neutral substrate molecules.[45,90]

In the 1980s, electrospray ionization was further developed by Fenn and co-workers based on the work of Dole from 1968.[91,92] Due to the groundbreaking character, Fenn was awarded the Nobel prize for the new ionization method in 2002.[93] ESI usually does not ionize analytes in the sense that neutral molecules are transformed into charged species but rather transfers already ionic analytes from the solution into the gas phase. Often, the sample solution is treated with an acid (a base) as an additive to produce charged analyte

---

[3] Recent investigations address the question of how mild electrospray ionization (ESI) is and many working groups study the internal energy distribution of analyte ions with the help of so-called "thermometer ions".[88,89] In fact, the author of this dissertation spent much of his undergraduate studies developing new such thermometer ions and investigating the energy-uptake of analyte ions within mass spectrometers.[89]

species. They form via protonation (or deprotonation) reactions either within the sample vessel or in so-called microdroplets during the electrospraying process. At the end of the process, single gaseous analyte ions are given.[84]

As this ionization method was extensively used for this dissertation, it will be explicated in detail. First, the instrumental setup of the ion source will be addressed. Thereafter, the microscopic processes of the electrospray ionization and ion formation will be explained.
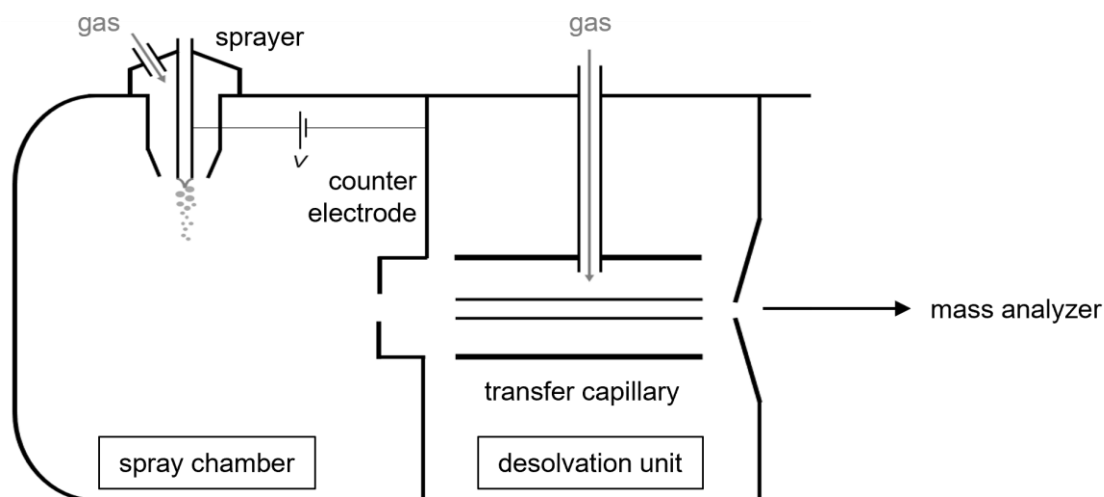

Figure 5:   Schematic representation of a typical electrospray ionization (ESI) source. In the spray chamber, the sample solution is electrosprayed at ambient pressure. The resulting microdroplets are transferred into the desolvation unit. Eventually, desolvated analyte ions leave the transfer capillary and are focused towards the mass analyzer.

Modern ESI sources combine two instrumental stages. In the spray chamber, an aerosol of the sample solution is produced. This stage is run at atmospheric pressure. Thereafter, the analyte ions are freed from solvent in the desolvation unit at reduced pressures.[84]

Initially, the sample solution is injected into the ion source at flow rates of a few hundred µL h^{-1}. The sample solution is then electrosprayed. This electrospray is generated by the application of high voltages (several kV) to the spray capillary. Often, the spraying is assisted by a sheath or nebulizer gas (<1 bar). Charged microdroplets are then electrically accelerated towards the interior of the mass spectrometer. The counter electrode features an orifice through which the charged particles enter into the desolvation unit against a stream of heated gas (dry gas). An electric bias voltage (approx. 20 V) causes the solvated analyte ions to pass a heated transfer capillary made of glass. Eventually, bare analyte ions form and are focused into to the mass analyzer, e.g. by a nozzle-skimmer or ion-funnel configuration. The former setup is rather outdated, the latter is more modern as it allows for higher ion transmission and thus better signal intensities (Figure 5).[84]

As the processes of electrospraying and ion formation are complex, they should be elucidated in more detail. In principle, the formation of bare analyte ions within the ESI source includes three phases. First, the electrospray of the sample solution is produced. Second, the microdroplets shrink until, third, singular desolvated ions are released.[84,94]

If an electrolyte-containing solution is exposed to high-voltage electric fields, charge separation occurs and, based on the chosen polarity, cations or anions are enriched at the surface of the liquid. As a consequence, the meniscus of the solution is distorted into an oval, and the effective strength of the electric field increases even more. The phenomenon

is repeated until the critical field strength is reached. At this point, the so-called Taylor cone forms that ejects a jet of the sample solution. However, this jet is not stable and breaks down into charged microdroplets. Given their same polarity, the microdroplets drift away from each other due to Coulomb repulsion and, so, the jet transforms into a spray.[84,94] The microdroplets have typical diameters of a few micrometers and contain large excesses of cations or anions. As solvent evaporates from the microdroplets, the charge density at their surfaces rises. Eventually, the Coulomb repulsion will overcome the surface tension of the droplets. At this Rayleigh limit, nanodroplets are ejected from the microdroplet. According to the mechanism of droplet jet fission, this nanodroplet formation happens in an analogous fashion to the jet-spray formation at the Taylor cone – and not as a Coulomb explosion. The process is repeated over and over again. Finally, droplets featuring diameters of less than 10 nm form. These small nanodroplets contain only very few analyte ions and solvent molecules.[84,94]

There are two main models that explain how single analyte ions come into existence from these small nanodroplets. In the charged residue model (CRM), the small nanodroplets are assumed to further shrink by continuous loss of solvent molecules until only one single analyte molecule remains. During this shrinkage, the residual charge within the nanodroplet is transferred to the analyte and, thus, ions form by protonation or adduct formation. Therefore, the CRM is often applied to rationalize the ion formation for large biomolecules or macromolecules M, as (multiply) protonated species MH^+ (MH_n^{n+}) or metal adducts, such as MNa^+, are often observed in their ESI mass spectra.[84,94]

In contrast, the ion evaporation model (IEM) postulates that the bare analyte ions form by evaporation from the highly charged surface of nanodroplets. As the nanodroplets decrease in size, the distance between the analyte ions at the droplet surface is also reduced. At some critical field strength, single analyte ions are evaporated off the small nanodroplet. The IEM is able to account for the effects that different ESI conditions (e.g. dry gas pressure or temperature) exert onto the observed species. Moreover, it can explain the different ESI efficiencies of analyte ions through their varying surface activities. The IEM is usually employed to describe the ion formation for small molecules such as common organic and organometallic ions and, thus, is most relevant for this dissertation.[84,94]

1.2.1.2   Ion traps and gas-phase reactivity studies

In MS, there are many types of mass analyzers such as time-of-flight (TOF) and Fourier-transform ion cyclotron resonance (FT-ICR) analyzers, magnetic sector fields and quadrupole ion traps. However, for the study of intrinsic reactivities mass analyzers featuring tandem mass spectrometry (MS^n) capabilities are required. Tandem mass spectrometry allows for the combination and subsequent conduction of n mass-spectrometric experiments in one instrument. MS^n can be carried out either in a spatial fashion (e.g. in quadrupole time-of-flight configurations) or in a temporal manner. FT-ICR and quadrupole ion trap mass spectrometers feature extensive possibilities for such temporal tandem mass spectrometry. Their big advantage is that the mass-spectrometric experiments can be conducted within the same instrumental component preventing the need for complex and demanding multi-component spectrometers to be built.[84]

In FT-ICR instruments, the ions are stored in static magnetic fields and analyzed with help of dynamic electric fields. As a result of the Lorentz effect, moving ions that are exposed to a magnetic field start circulating in the plane orthogonal to the applied field. Anions rotate

clockwise and cations counter-clockwise around the axis. The circulation of the ions is described by the cyclotron frequency f_c in Equation 6:[84]

$$f_c = \frac{B}{2\pi} \times \frac{z}{m}$$

Equation 6

For a defined magnetic field strength B, the cyclotron frequency f_c is specific for each mass-to-charge (m/z) ratio.[84]

For the actual mass analysis and detection of the ions, they are coherently excited by electric fields that change with radio frequency (RF). This resonant excitation causes the radius of the circular motion around the axis to increase. Eventually, the radius of the ion motion almost equals the radius of the ICR cell. The image current that the ions induce by passing the detector is measured as a function of the time. As the measured signal depends on the applied resonance frequency, the assignment of the signals to the mass-to-charge ratio of the respective ions is possible. The signal is then Fourier transformed from the time domain into the frequency domain. At last, m/z ratios are calculated based on the determined frequencies and the mass spectrum can be constructed.[84]

Commercially available FT-ICR mass spectrometers often employ an instrumental configuration referred to as Penning trap. They feature very high mass resolutions (10^4-10^5) and mass accuracies ($<10^{-3}$ u). However, as they need strong magnetic fields (typically 7 or 9.4 T), they are instrumentally demanding and require a lot of maintenance.[84] Therefore, they became rare over the last decades. Nowadays, another kind of ion trap is more common: quadrupole ion traps.[84]

The popularity of quadrupole ion traps emerges from their easy handling and instrumental robustness. Modern quadrupole ion trap mass spectrometers typically are desktop devices, require only high vacuum in the order of 10^{-5} mbar and are financially affordable. However, these benefits come with a price: Quadrupole ion trap mass spectrometers only provide rather poor resolution and their mass range is rather limited ($m/z < 2000$).[84] In the past, quadrupole ion trap mass spectrometers were frequently used to study the reactivity of gaseous ions.[45,90] Therefore, the types of quadrupole ion traps are explained in the following.

There are two types of quadrupole ion traps: the linear ion trap (LIT) and the 3D quadrupole ion trap (QIT). Both instrumental configurations make use of dynamic electric fields to store the ions. In order to understand the working principles behind quadrupole ion traps, it is necessary to understand the behavior of ions within electric radio-frequency quadrupole potentials. The physics of ions passing through a linear quadrupole mass filter is a good starting point for that purpose.
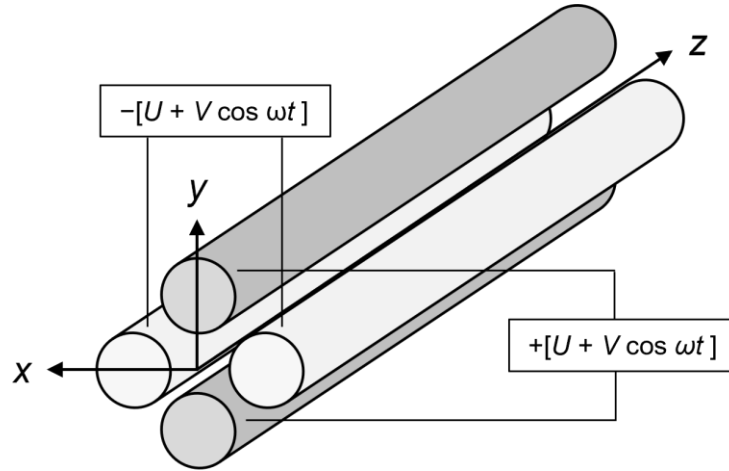
Figure 6: A linear quadrupole mass filter consists of four rods where two electrodes are pair-wise held at the same potential. Ions are centrally confined by changing the AC component with some radio frequency. According to reference [84].

A linear quadrupole mass filter is made of four rods with hyperbolical or circular cross sections. To the rods changing electric potentials are applied in such a way that the rods of the same polarity are always opposite of each other. In more detail, the electric potential Φ is the sum of a direct current (DC) component U and an alternating current (AC) component V which is changed with the radio frequency ω as a function of the time t (Figure 6, Equation 7):[84]

$$\Phi = U + V \cos \omega t \qquad \qquad \text{Equation 7}$$

Ions that enter the linear quadrupole mass filter along the z-axis will be attracted by the rods of the opposite polarity and repelled by those of the same polarity in the xy plane. If the electric potentials are changed sufficiently fast, the ions are stabilized on their way through the linear quadrupole.[84]

The physics of such stable ion trajectories through a dynamic electric quadrupole field are mathematically described by the Mathieu equations. The conditions for stable trajectories of an ion with a certain m/z ratio are given by their solutions and characterized via the Mathieu parameters a and q where r_0 is the distance between the center of the xy-plane and the rods (Equation 8):[84]

$$a = \frac{4U}{r_0^2 \times \omega^2} \times \frac{z}{m}, \quad q = \frac{2V}{r_0^2 \times \omega^2} \times \frac{z}{m} \qquad \qquad \text{Equation 8}$$

Solutions to the Mathieu equations can be visualized in stability diagrams (Figure 7). Ions can only pass the quadrupole if their masses on the working line, which is the ratio of the Mathieu parameters a and q, lie within the stable regime. The working line ($a/q = 2U/V$) is adapted for different m/z by changing the ratio of the DC and AC component U and V. The steeper the working line and the smaller Δq is, the higher is the achieved resolution.[84]

Linear quadrupoles mass filters can be run either as ion guides if only ions with m/z higher than a certain threshold value are stabilized or as mass analyzers when an entire range of m/z is scanned by tuning the working line for different mass-to-charge ratios one after another.[84]
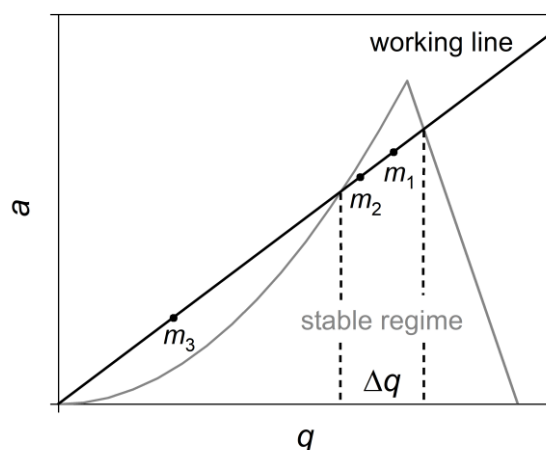
Figure 7:   Stability diagram for trajectories within a linear quadrupole mass analyzer. The working line, which is the ratio of the Mathieu parameters a and q, is tuned by changing the AC voltage component V. Only ions with m/z ratios on the working line that lie within the stable regime (m_1 and m_2) pass the quadrupole mass filter, others (m_3) do not. According to reference [84].

To come from linear quadrupole mass filters to ion traps, trapping potentials must be applied at the ends of the linear quadrupole configuration. In that way, the ions are confined by the quadrupole rods in the xy-plane and by the end plates in the z-direction.[84]

Linear ion traps (LIT) are run in three phases. First, they are charged with ions by applying zero potential at one end and a trapping potential at the other. Second, the ions are stored when the trapping potential is applied to both end plates. A buffer gas (He) is introduced to cool the ions and, thus, reduce the spatial extent of the ion cloud. At last, the ions are ejected by an extraction potential at one end of the LIT into the direction of the next instrumental stage, e.g. the detector or another mass analyzer.[84]

LITs offer various possibilities for MS^n. Ions can be accumulated or mass-selected in linear ion traps first and, subsequently, transferred into another mass analyzer where the mass analysis or another mass-spectrometric experiment is performed. For instance, LITs can be connected to FT-ICR or Orbitrap mass analyzers.[84]

Another instrumental design of quadrupole ion traps is the three-dimensional quadrupole ion trap (QIT) which is also called Paul trap. The QIT consists of two hyperbolically shaped end caps as well as the ring electrode. It exploits the same physical principles as the LIT: Dynamic electric potentials are applied to the end caps and the ring electrode. By changing the ratio of the DC and AC component, ions of certain m/z are stabilized. The ion cloud is confined in all three dimensions in the center of the QIT. Just as in the LIT case, a buffer gas (He) is used to thermalize the ions. Ions are introduced into and ejected out of the QIT through small holes in the end caps (Figure 8).[84]
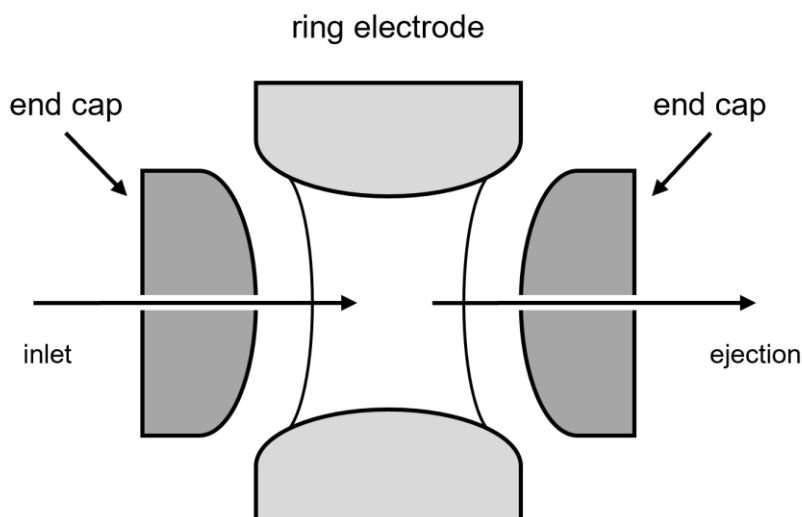
Figure 8:   Transverse section of a three-dimensional quadrupole ion trap (QIT). The QIT consists of two end caps and one ring electrode. The ions are confined in the center by dynamic electric fields. After the mass-spectrometric experiment, the ions are ejected to the detector. According to reference [84].

Three-dimensional quadrupole ion traps feature two operating modes: They can perform a mass scan or a mass selection. For both modes, modern QITs employ resonant excitation to eject the ions of a certain m/z ratio. In the scanning mode, the entire m/z range is scanned either from small to large m/z (forward scan) or the other way round (backward scan). One after the other, each m/z is excited and ejected. Each m/z then produces a signal at the detector and, thus, the mass spectrum is constructed. In the mass-selection mode, the ions of only one specific m/z ratio are stored in the QIT. This is achieved by a combination of forward and backward scanning, so that all ions with lower and higher m/z ratio than the selected one are thrown out.[84]

Quadrupole on traps provide great opportunities for gas-phase reactivity studies as they are able to accumulate, store and thermalize as well as mass-select ions. Modern mass-spectrometric and gas-phase experiments often employ two methods: collision-induced dissociation (CID) and ion-molecule reaction (IMR). As these two were frequently used throughout the project of this dissertation, they will be detailed below.

CID experiments can be carried out either in LITs or QITs. In such studies, the species of interest is first mass-selected. Afterwards, this precursor species is excited and its kinetic energy increases. The ions then collide with the buffer gas in the ion trap and, thus, the kinetic energy is converted into internal energy. As a consequence of the higher internal energy, the precursor species fragments. The resulting charged or neutral fragments bear information about the structure and unimolecular reactivity of the precursor species.[84,95]

Ion-molecule reactions are a way to probe the bimolecular reactivity of the species of interest. The first step is the mass selection of the ion under scrutiny. In the second step, the actual reaction, the methodologies diverge. For the sake of this work, two of them will be elaborated: the flowing-afterglow selected ion flow tube (FA-SIFT) technique as used by Bierbaum and DePuy[95] as well as the helium-substrate inlet method as carried out by Gronert and O'Hair.[43,96–99]

The FA-SIFT technique, which Bierbaum and DePuy made use of, is based on other flowing afterglow setups. Such designs combined a glow-discharge ion source with a downstream flow tube. After the analyte ions were formed in the afterglow, they flowed towards the next

instrumental stage. Within that time span, the ions were subjected to reactions with a neutral substrate gas which was introduced into the flow tube. Not yet converted reactants as well as the reaction products were then transferred into the mass analyzer. Depending on the length of the flow tube and the point of substrate insertion, the time for the ions to react with the substrate and, thus, the ratio of products to the reactants, varied. Thereby, kinetic measurements of ion-molecule reactions were performed. If a quadrupole mass filter is set between the glow discharge region and the flow tube, it is possible to select ions of specific mass-to-charge ratios, so that the intrinsic reactivity of the selected species can be studied. Bierbaum and DePuy connected the FA-SIFT stage with a triple quadrupole mass analyzer. These additional linear quadrupole mass filter not only served for ion transmission but also featured the capability to conduct CID experiments. [49,95,100]

Another method to probe the bimolecular reactivity of mass-selected ions was employed by Gronert and O'Hair. They modified quadrupole ion traps in such ways that they continuously fed a neutral substrate into the ion trap via its helium inlet. For that, a liquid volatile substrate was injected into the He tube with a syringe. Adjusting the helium and substrate flows, the concentration of the substrate within the ion trap was set. The mass-selected ions were stored in the ion traps for varying times where they underwent reactive collisions with substrate molecules. By varying the storage time, they obtained time-dependent species profiles. From those data, the bimolecular reaction rate constants were extracted with experimental uncertainties of ±25%. [43,96–99]

In 2019, Koszinowski introduced a new setup for introducing the substrate into the QIT via the He inlet. Instead of injecting the liquid substrate into the He tube, a defined mixture of the substrate and He is prepared within a gas-mixing chamber. First, a reservoir is evacuated to pressures of around 10^{-5} mbar. The liquid substrate is cleaned by pump-freeze-thaw cycles and subsequently evaporated into that container and mixed with He (6.00 bar). The gas mixture is then introduced into the QIT wherein the mass-selected ions react with an excess of the substrate under pseudo-first order conditions. Knowing the partial pressure of the substrate, the effective rate constants are converted into bimolecular rate constants. The error margin of the bimolecular rate constants is typically ±30%. The experimental design was successfully employed for gas-phase substitution reactions as well as oxidative addition and protonation reactions of organometallic ions. [101–103] This setup was also used for the experiments of this thesis. The details are described in section 5.1.3.2.

1.2.2 Computational chemistry

Computational chemistry refers to methods which enable researchers to investigate chemical questions by means of theoretical calculations and simulations *in silico*. As such methods were used in the protonation studies by, for instance, Bernasconi,[66–68] Gronert[60] or O'Hair[80,81] and also posed an essential part of this dissertation's project, they will be explicated below. Two kinds of computational methodologies were applied: quantum-chemical calculations as well as kinetic simulations. The details on the former are largely based on the textbook by Jensen.[104]

1.2.2.1 Quantum-chemical calculations

Chemical systems are fully described by their wave function which contains information about their nuclear and electronic degrees of freedom (DOF). The nuclei can be described as classical particles. In marked contrast, the electrons feature quantum character.

Therefore, it was proposed in the Born-Oppenheimer approximation (BOA) to separate the total wave function into a nuclear and an electronic part. In terms of the system's energy, this corresponds to splitting the total energy E_{tot} into the nuclear components (E_N) in the form of the translational energy E_{trans}, the rotational energy E_{rot} and the vibrational energy E_{vib} as well as the electronic contribution E_{el} (Equation 9).[105]

$$E_{tot} = E_N + E_{el} = E_{trans} + E_{rot} + E_{vib} + E_{el} \qquad \text{Equation 9}$$

Whereas the translational, rotational and vibrational energies are calculated with *classical* mechanics, the computation of the electronic energy requires *quantum* mechanics. Thus, quantum-chemical calculations (QCC) are conducted to determine the *electronic energy* E_{el}. If the electronic energy is calculated as a function of the nuclear coordinates as parameters, the so-called *potential energy surface* (PES) is obtained. The PES usually is multidimensional and, thus, representations of the PES, which are reduced in its dimensionality, are common. 2D representations are depicted as energy profiles, 3D representations are visualized either as three-dimensional or contour plots. If the abscissa of the energy profile is the reaction coordinate, the plot is referred to as the *reaction pathway*. In such depictions, the energy is often not given continuously along the reaction coordinate but only for discrete points. These stationary points are local minima for stable chemical structures, such as reactants, intermediates and products, as well as saddle points which correspond to transition states.[105]

There are two fundamental domains of quantum-chemical methods which employ different approaches to calculate the electronic energy: wave-function theory as well as density functional theory (DFT).[104] Both of them were used for this work and, thus, will be described below. An overview of the different classes of quantum-chemical methods is given in Figure 9.
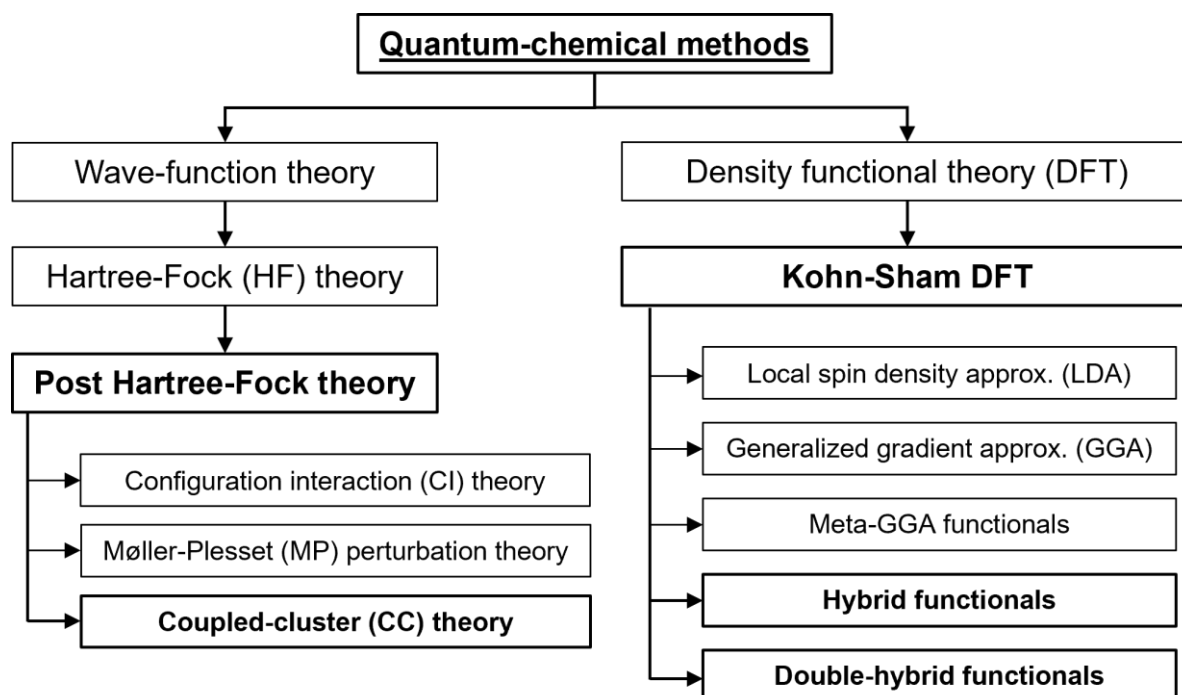

Figure 9: Overview of the different classes of quantum-chemical methods. Classes of methods which were used for this work are printed in bold.[104] For details, see text.

Wave-function methods are *ab initio* ("from the beginning"), i.e. they rely only on physical laws and constants and do not include any empirical information. They are based on the theory by Hartree and Fock. Hartree-Fock (HF) theory determines the approximate electronic energy within a molecule by solving the non-relativistic time-independent Schrödinger equation for many-electron systems. In this equation, the electronic energy E_{el} is calculated as the eigenvalue(s) of the electronic Hamilton operator $\boldsymbol{H}_{el}$ and the many-electron wave function Ψ_{el} (Equation 10):[104]

$$\boldsymbol{H}_{el}\Psi_{el} = E_{el}\Psi_{el} \qquad\qquad \text{Equation 10}$$

In Hartree-Fock theory, the problem of solving the many-electron problem is further tackled by breaking it down into the sum of many one-electron problems. To do so, electrons are assumed to be independent particles moving in the mean field of all the other electrons. The electronic wave function Ψ_{el} is constructed as the Slater determinant from the one-electron wave functions φ_i. Furthermore, the electronic Hamilton operator $\boldsymbol{H}_{el}$ is re-formulated in terms of the many one-electron operators $\boldsymbol{h}_i$, $\boldsymbol{J}_i$ and $\boldsymbol{K}_i$, where $\boldsymbol{h}_i$ describes the motion in the field of the nuclei, $\boldsymbol{J}_i$ the Coulomb potential and $\boldsymbol{K}_i$ the exchange interaction of the electron i. In the end, the Hartree-Fock equations are formulated which pose a set of pseudo-eigenvalue equations of the Fock operator $\boldsymbol{F}_i$ and the canonical molecular orbitals φ'_i (Equation 11):[104]

$$\boldsymbol{F}_i\varphi'_i = \varepsilon_i\varphi'_i \qquad\qquad \text{Equation 11}$$

Eventually, the energies are determined by applying the variational principle: For any approximate wave function, the calculated energy will be equal to or higher than the energy of the exact wave function. The variational principle thereby opens up the possibility to find an approximate wave function very close to the exact wave function and, in consequence, an approximate energy that is very close to the exact energy. The "best" approximate wave function is searched for computationally in an iterative fashion starting from some arbitrary initial guess of the molecular orbitals. The set of molecular orbitals, which solve the Fock equations, is referred to as the self-consistent field (SCF). The molecular orbitals, in turn, are constructed from the linear combination of atomic orbitals (LCAO). These atomic orbitals are mathematical functions representing the orbitals (and their angular momentum) of atoms and the set of such basis functions is called basis set. The size of basis sets is described via the *n*-Zeta (*n*Z) notation where higher *n* stand for larger basis sets. The larger the basis sets are, the better is the approximation of the "true" molecular orbitals. The computational cost for HF calculations scales with the fourth power of the system size N (N^4).[104]

The major limitation of the Hartree-Fock theory is that it does not account for the correlation of the electrons as a consequence of the mean field approach. However, the correlation energy is chemically significant, although it poses only about 1% of the total energy. So, in order to compute meaningful results, the correlation energy has to be included into the quantum-chemical calculations. There are several such post Hartree-Fock methods. The three most prominent candidates are configuration interaction, Møller-Plesset perturbation and coupled-cluster theory.[104,106]

The configuration interaction (CI) method addresses the correlation energy through the addition of excited Slater determinants to the Hartree-Fock wave function. The Hartree-Fock wave-function corresponds to the non-excited case to which singly, doubly, triply, etc.

excited determinants are added. The thus modified wave function is then used to solve the Schrödinger equation in an analogous manner to the HF approach. The higher the considered excitation is, the more accurate the calculated energy is. In the case of full configuration interaction (FCI) and an infinitely large basis set, the "exact" result is obtained.[104,106]

In Møller-Plesset (MP) perturbation theory, the total energy is calculated by means of a series expansion according to the many-body perturbation theory. Starting from the Hartree-Fock energy, the correlation energy is obtained from considering all excitation terms (single, double, triple, etc.) up to a certain order n where n is the number of electrons interacting with each other. Depending on the order of the highest perturbative contribution, multiple kinds of Møller-Plesset theory, such as MP2 (N^5) or MP4 (N^7), exist.[104,107]

In coupled-cluster (CC) methods, the total energy is calculated by including all excitation terms of a certain order (single, double, triple etc.). If the excitation was to be expanded to infinity, the "true" energy would be determined. However, as the calculations are run computationally, the hardware limitations restrict the order of the expansion. Therefore, CC methods are truncated and often include the excitation terms up to the second order (CCSD). To enhance the accuracy, the energetic contribution from the triple excitation (T) is then added employing a perturbational ansatz. This approach is denoted CCSD(T), scales with N^7 and is commonly referred to as the "gold standard" in quantum chemistry. CCSD(T) typically achieves accuracies better than the desideratum of "chemical accuracy" which means that the energy difference between the experimentally determined and theoretically computed value is within 4 kJ mol^{-1}.[104,108] In the last two decades, CC methods were advanced with the intention to decrease the computational cost but keeping the high accuracy. In this regard, so-called *local* CC methods in contrast to the canonical ones were developed. They consider only the interactions of those electrons which are in proximity to each other. The domain-based local pair natural orbital (DLPNO) CCSD(T) method by Neese is known to deliver accurate results even for large organometallic systems.[109–111]

The second class of quantum-chemical methods is based on density functional theory (DFT). In general, DFT calculations feature much lower computational costs which renders them powerful tools even for the investigation of (very) large chemical systems. DFT grounds on the theorems by Hohenberg and Kohn:[112]

1. The electronic ground state energy E of a chemical system is determined by its electron density ρ via the functional $E[\rho]$.
2. The variation of the electron density ρ within one system can only result in higher energies than for the ground state.

The second theorem thus makes the utilization of the variational principle applicable to DFT. The exact functional $E[\rho]$ is, however, not known and must be computed in some way. Kohn and Sham (KS) described the electronic energy in the framework of an independent particle and separated the functional $E[\rho]$ into several components (Equation 12):[104]

$$E_{KS}[\rho] = T[\rho] + V_{N-el}[\rho] + J[\rho] + E_{XC}[\rho]$$

Equation 12

$T[\rho]$ corresponds to the kinetic energy of non-interacting electrons, $V_{N-el}[\rho]$ to the potential between nuclei and electrons and $J[\rho]$ to the Coulomb potential between the electrons. The so-called exchange-correlation functional $E_{XC}[\rho]$ is defined such that it comprises all

contributions that make the difference between the Kohn-Sham functional $E_{KS}[\rho]$ and the exact functional $E[\rho]$. In KS-DFT, the electron densities are described by the introduction of atomic orbitals. The electron densities are represented by the linear combination of atomic orbitals (LCAO). In an analogous manner to HF theory, the solutions to the KS equations are searched for computationally within the self-consistent field procedure. The computational costs of KS-DFT in its simplest form scale with N^3.[104]

However, the exchange-correlation functional $E_{XC}[\rho]$ is not known and must therefore be expressed in some way. The formulations for $E_{XC}[\rho]$ in KS-DFT build the grounds for the variety of DFT methods. Following the taxonomy by Perdew, the exchange-correlation functionals can be classified into the rungs of the "Jacob's ladder of density functional approximations"[113] ranging from the Hartree-Fock world to the heaven of chemical accuracy.[113] In the context of chemistry, the following DFT functionals are of relevance (ordered from low to high accuracy):

3. local spin density approximation (LDA),
4. generalized gradient approximation (GGA),
5. meta-generalized gradient approximation (meta-GGA),
6. hybrid, and
7. double-hybrid.

In the LDA, only the electron density itself is considered for $E_{XC}[\rho]$. GGA functionals express the $E_{XC}[\rho]$ via the electron density and its derivative. Hybrid functionals further include exchange energy from Hartree-Fock calculations and double-hybrid functionals incorporate HF exchange energy as well as correlation energy from a MP2 calculation.[114] One significant shortcoming of KS-DFT is that intermolecular interactions are not well represented resulting in the poor description of chemical properties. Therefore, dispersion corrections are added. The most popular dispersion correction is Grimme's D3 correction with Becke-Johnson damping.[115]

During the last decades, quantum-chemical calculations were significantly facilitated by the development of new methods and the provision of (open-source) quantum chemistry packages such as ORCA by Neese.[116,117] With these software suites, it became feasible even for non-theoretical chemists to conduct QCC. Typically, structures of chemical species are computed employing DFT methods. Electronic single-point energies are usually calculated either with hybrid or double-hybrid DFT methods or sophisticated wave-function methods such as DLPNO-CCSD(T). Calculations are often carried out for the gas phase, but may also be performed for the solution phase with the help of solvation models.[118]

With the advent of more and more computational methods, the checking of their performances becomes increasingly important. Such benchmarking is conducted by comparing the theoretical result calculated by the method under scrutiny to either some theoretical or experimental reference data. For theory-theory benchmarking, data from the canonical CCSD(T) method is often used as the reference. Experiment-theory benchmarking is rather rare, but crucial to evaluate the suitability of QCC methods with respect to real-life chemical problems.[119]

1.2.2.2   Calculation of theoretical rate constants

In this work, experiment-theory benchmarking is carried out with regards to the barriers of the gas-phase protonation reactions of organometallics where bimolecular reaction rate

constants are the observables. Experimental rate constants are compared to theoretical ones. For this to be possible, the computed reaction barriers need to be converted into theoretical rate constants before-hand. Such theoretical bimolecular rate constants k incorporate two components: the collision rate k_{coll} of ions and neutrals, which poses the upper limit of the rate constant, as well as the reaction efficiency φ (Equation 13). The two components will be explained below.

$$k = k_{coll} \times \varphi$$

<div align="right">Equation 13</div>

The collision of ions with neutrals is determined by the long-range forces of the impact partners. The ion is often considered to be a point charge. The neutral can either be apolar or polar and feature an induced or permanent dipole.[95]

In the Langevin model, the neutral features the polarizability α and the reduced mass μ and interacts with the point charge Zq. The Langevin collision rate k_L is defined in Equation 14 where ε_0 is the vacuum permittivity:

$$k_L = \frac{2\pi Zq}{(4\pi\varepsilon_0)} \times \left(\frac{\alpha}{\mu}\right)^{1/2}$$

<div align="right">Equation 14</div>

The Langevin collision rate thus increases with the polarizability of the neutral.[95]

For proton-transfer reactions, the collision of ions with permanent dipoles have to be considered. The orientation of the dipole towards the ion plays a role and, thus, has to be accounted for. One approach is to lock the orientation of the dipole ("locked dipole") and calculate the collision rate within this approximation.[120] The capture rate constant k_{LD} then is (Equation 15):

$$\frac{k_{LD}}{k_L} = 1 + \mu_D \left(\frac{2}{\pi\alpha k_B T}\right)^{1/2}$$

<div align="right">Equation 15</div>

with μ_D being the dipole moment, k_B the Boltzmann constant and T the temperature. In the locked dipole perspective, however, the capture rates are overestimated. Therefore, another model is more suitable: the average dipole orientation (ADO) model. Herein, an "effective" dipole moment of the neutral is calculated by averaging over the rotational states. The approach is parametrized and the capture rate obtained from trajectory calculations.[95,121] The capture theory by Su and Chesnavich is commonly applied and typical values for ion-neutral collision rates are in the order of 10^{-9} cm^3 s^{-1}.[122–124,125] Nevertheless, the calculated collision rates do not reflect on the full physical picture because they still assume the ions to be point charges. Due to neglecting the spatial extent of the ions, the capture rates are underestimated.[126]

For bimolecular reactions, the reaction efficiency φ is an expression for the fraction of the pre-reactive complex reacting to the product complex via the central barrier. In mass spectrometry and gas-phase chemistry it is calculated from unimolecular rate constants for which, in turn, statistical rate theories are employed. Given that the reactions proceed in the vacuum, the chemical ensemble is microcanonical and so, unimolecular rate constants $k(E)$ are calculated as a function of the energy E for each particle. The energy cannot be exchanged between two particles, as no heat bath is present. The approach is in distinct contrast to the solution phase where the ensemble is canonical and the well-known canonical transition state theory (TST)[127] can be applied for the calculation of rate

constants.[95] As a consequence of the microcanonical nature of gas-phase reactions, the potential energy surface of gas-phase reactions is better described via the enthalpy (at 0 K), $\Delta H_{(0)}$, than in terms of the Gibbs energy (at 298 K), $\Delta G_{(298)}$.[128]

Statistical rate theories consider the kinetics of chemical reactions in an averaged fashion. The assumption is that the energy within the molecule or ion is randomized amongst all its degrees of freedom and energetic (de-)excitation proceeds instantaneously. Within the Rice-Ramsperger-Kassel-Marcus (RRKM) and quasi-equilibrium theory (QET), the unimolecular reaction is described using microcanonical transition state theory: If the reaction reaches the transition state as the "point of no return", the reaction takes place. The microcanonical rate constant $k(E)$ is expressed via the sum of states $N^{\ddagger}(E-E_0)$ of the transition state above the threshold energy or activation barrier E_0 and the density of states $\rho(E)$ of the reactant (Equation 16). By the introduction of the transmission coefficient $\kappa(E)$ quantum-chemical effects, such as proton tunneling, can be accounted for.[95]

$$k(E) = \kappa(E) \times \frac{N^{\ddagger}(E - E_0)}{h\rho(E)}$$
Equation 16

The unimolecular rate constant is statistically determined. It eventually results from the ratio of the number of states at the TS and the reactant. In other words: The reaction is more likely if the threshold energy E_0 of the TS is low because then the number of states at the TS is high and thus, there are more possibilities for the reaction to proceed from the reactant to the TS than vice versa.

If one wants to compare theoretical to experimental results, phenomenological (and not microcanonical) rate constants $k(T,p)$ are required though, which depend on the reaction temperature T and pressure p. One elegant approach is to simulate the reaction kinetics. Master-equation calculations lend themselves useful for this purpose as they model the time evolution of chemical systems of unimolecular and bimolecular reactions even within multi-well pathways.[129,130]

The Master equation (ME) in its simplest form is given in Equation 17 where t is the time, $n_i(t)$ the probability of the molecule to be in state i at the time t and p_{ij} the transition probability from state i to j per unit time. So, the rate of the system's probability to be in state i at the time t is the sum over all populating and depopulating processes at that time.[129,130]

$$\frac{\mathrm{d}n_i(t)}{\mathrm{d}t} = \sum_j \left(p_{ij} n_j(t) - p_{ji} n_i(t) \right)$$
Equation 17

As chemical systems such as molecules or ions are usually large and therefore feature many states, the ME is described in terms of the population of states $p(E)$ of a chemical species within the energy interval E and $E + \mathrm{d}E$ as well as the microcanonical rate constants $k(E)$ and the collisional energy transfer probabilities $P(E|E')$. The latter two correspond to the reactive processes from one species to another and the rovibrational (de-)excitation of one species, respectively. The ME is reformulated as the energy-grained master equation (EGME). The EGME poses a set of coupled differential equations which can be expressed as (Equation 18):[129,130]

$$\frac{d}{dt}\mathbf{p} = \mathbf{Mp}$$ <div style="text-align:right">Equation 18</div>

Therein, the vector **p** contains the population densities $p(E)$ of all species involved in the reaction. The transition matrix **M** includes the microcanonical rate constants $k(E)$ and collisional energy transfer probabilities $P(E|E')$. The EGME is parametrized and solved numerically.[129,130] Eventually, the time-dependent species profiles are obtained from which the phenomenological rate constants $k(T,p)$ can be extracted.
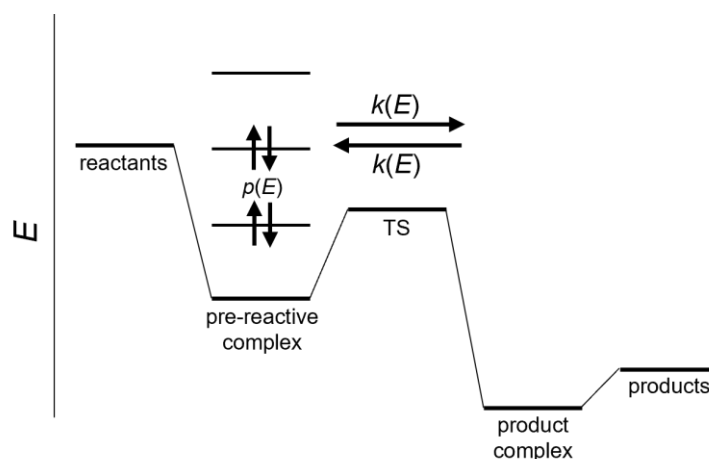
Figure 10: Multi-well reaction pathway for a typical ion-molecular reaction. Master-equation approaches calculate the time evolution of the reactive system by evolving the energy-dependent population $p(E)$ of the involved species over the course of time. $p(E)$ is affected by collisional (de-)activation and chemical reactions featuring the microcanonical rate constants $k(E)$. Adapted from reference [131].

The populations $p(E)$ of the involved species are evolved over the time t by considering the collisional (de-)activation (rovibrational (de-)excitation) within one species and additionally, the reaction from one species to another with the associated microcanonical rate constants $k(E)$. The formation of the pre-reactive complex can be modelled via the capture rate using the inverse Laplace transform (ILT) method. The actual proton-transfer step is calculated using RRKM theory (Figure 10).[131]

2   Approach and objectives

Protonation reactions are of outmost importance in nature and chemistry. Accordingly, they have been studied in the solution and gas phase for a long time. Even though there is a lot of understanding about the physical chemistry of proton transfer involving organic molecules, such as C–H acids and C bases, much less is known about the microscopic processes and intrinsic properties of organometallics that feature stabilized carbanions as substituents. As the reactivity is mostly defined by the activation energies associated with chemical reactions, the barriers of protonation reactions of organometallics should be of special concern.

This dissertation is set out to close the gap between the quantitative physicochemical understanding of proton transfer in organic molecules and the more qualitative perspective on the reactivity of organometallic compounds. So, it systematically analyzes protonation reactions of organometallic species in the gas phase and rigorously assesses the effects that changes in the proton donor and acceptor exert on the intrinsic reactivity.

The work connects the various perspectives and methodologies explained in the previous sections. On the one hand, the concepts of physical (organic) chemistry shall be combined with those of organometallic research. On the other hand, experimental and theoretical studies are brought together. These partnerships offer encouraging possibilities to investigate the intrinsic reactivity of organometallics towards protonation and to rationalize their properties by means of structure-reactivity relationships. Moreover, they allow for detailed mechanistic investigations of proton-transfer reactions of organometallic species in the gas phase.

In detail, this dissertation aims to
- unravel the typical mechanisms for the gas-phase protonation reactions of organometallic ions,
- elucidate the intrinsic reactivity of organometallic species towards protonation,
- understand the heights of the activation barriers for different protonation sites,
- and find the dependence of the kinetic activation barriers on the thermodynamic driving force.

The research design was as follows. By means of electrospray-ionization (ESI) mass spectrometry, organometallic species were transferred into the gas phase. The ions of interest were selected based on their mass-to-charge (m/z) ratio and, thereafter, subjected to ion-molecule reactions with a neutral proton donor. Kinetic measurements allowed for the observation of their intrinsic reactivity as well as the determination of experimental rate constants associated with each reaction pathway.

Furthermore, methods of computational chemistry were employed to gain deeper insight into the protonation reactions. The structures of the reactants, intermediates, transition states and products along the reaction pathway were computed using density functional theory (DFT). Next, the energies of each stationary point were determined with high accuracy by conducting electronic single-point energies calculations with sophisticated wave-function methods. On the basis of the structures and energies, theoretical rate constants were then calculated applying statistical rate theory.

The research project largely benefitted from the interplay of experiment and theory. By comparing the theoretical rate constants against the experimental ones, which are completely independent from each other, proposed reaction pathways as well as the

performance of computational protocols could be checked (Figure 11). In this regard, the experimental results served as reference data for the benchmarking of numerical quantum chemistry. This served the purpose of the research training group "Benchmark Experiments for Numerical Quantum Chemistry" (BENCh; RTG 2455) within which this project was carried out.[132]
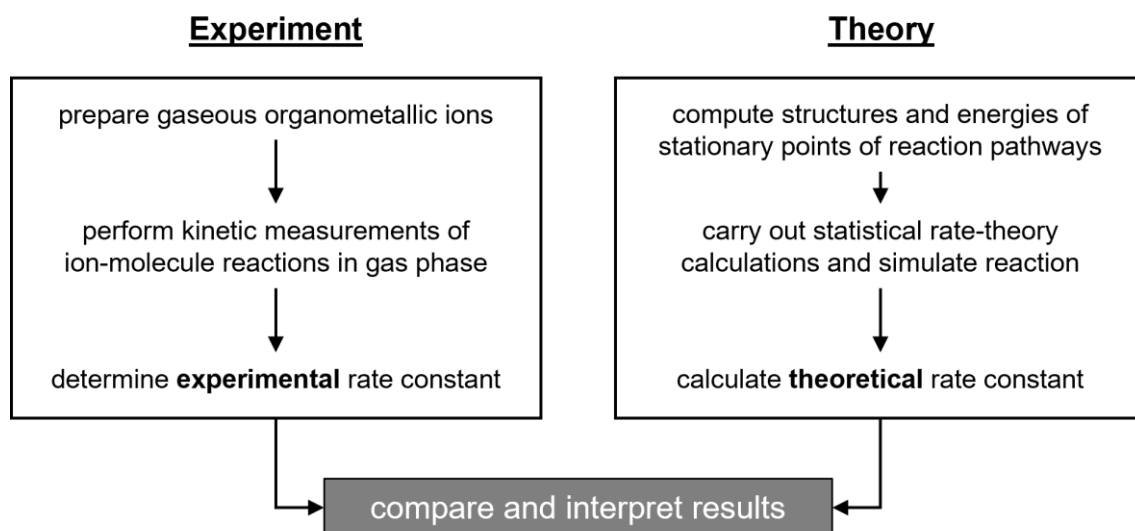
Experiment　　　　　　　　　　　　**Theory**

prepare gaseous organometallic ions	compute structures and energies of stationary points of reaction pathways
↓	↓
perform kinetic measurements of ion-molecule reactions in gas phase	carry out statistical rate-theory calculations and simulate reaction
↓	↓
determine **experimental** rate constant	calculate **theoretical** rate constant

compare and interpret results

Figure 11:　　Design of the research project about the barriers of protonation reactions of organometallics which is described in this dissertation.

The organometallic systems under investigations were organometalates, i.e. anionic metal complexes featuring carbon moieties. First, the intrinsic reactivity of organozincate anions towards protonation was probed. The effects, which occur upon changing the substituents within the metal complex and the proton donor, were studied. Second, organoferrate anions were tested in order to analyze how the metal center and its electronic configuration influence the reactivity. Third, more generic derivations about the typical mechanism of protonation reactions of organometallics as well as the dependence of the reaction barrier on the reaction energy were made. Thereby, the new results were re-connected to earlier research about proton transfer. The work concludes with stating the central findings and drawing the road map for further research.

3 Results and discussion

3.1 Protonation of organozincate anions

Organozincate anions are anionic representatives of zinc organyls which are commonly applied in synthetic chemistry.[133] The species consist of the Zn(+II) metal center and three anionic substituents from which at least one must be an organic residue. Their overall charge of −1 makes them amenable to mass-spectrometric investigations. Organozincate species are readily prepared via the transmetalation of the organic residue from Grignard reagents RMgX or lithium organyls RLi onto zinc halides ZnX_2 (R = organyl; X = Cl, Br, I) as Koszinowski and coworkers demonstrated.[134,135] With their closed-shell electronic configuration ($3d^{10}$) they pose ideal model systems for the systematic assessment of protonation reactions of organometallics because their intrinsic reactivity cannot be affected by spin-electronic effects. Thus, their microscopic reactivity is largely controlled by the substituents.

3.1.1 Variation of proton acceptor

3.1.1.1 Influence of carbon bases

To assess the effects that different kinds of carbon bases with regards to their hybridization (sp^n) exert onto the intrinsic reactivity of organozincate anions, species bearing aryl (sp^2) and alkyl (sp^3) moieties were probed. Trisarylzincate anions Ar_3Zn^- (Ar = Ph, p-C$_6$H$_4$X), mixed aryl-alkyl organozincate anions Ph_2ZnMe^- and $PhZnMe_2^-$ as well as homoleptic trisalkylzincate anions R_3Zn^- (R = Me, Et) were used for this purpose.

The proton-transfer reactions of the trisarylzincate anions Ph_3Zn^- and $Ar^XZnPh_2^-$ (Ar^X = p-C$_6$H$_4$X) featuring electron-donating groups (EDG; X = NMe$_2$, OMe, Me) or electron-withdrawing groups (EWG; X = F, Cl) were studied. The trisarylzincate species $Ar^XZnPh_2^-$ can react in two different ways upon the reaction with the proton donor 2,2,2-trifluoroethanol ($R^{F3}OH$): Either the substituted aryl moiety or one of the two phenyl groups is protonated (Scheme 7).[4]
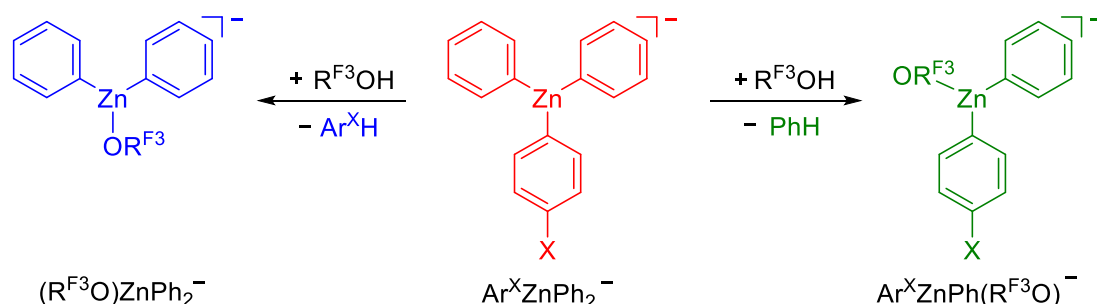
Scheme 7: Protonation reactions of the *para*-substituted trisarylzincate anions $Ar^XZnPh_2^-$ (X = NMe$_2$, OMe, Me, H, F, Cl) (red) with 2,2,2-trifluoroethanol ($R^{F3}OH$) in the gas phase. The competitive reactions of the protonation at the aryl (blue) vs. phenyl site (green) lend themselves useful for the design of a Hammett study wherein the electronic effects of the *para*-substituents X on the intrinsic reactivity of the organozincate anions towards proton transfer can be analyzed. Adapted with permission from reference [102]. Copyright 2023 American Chemical Society.

---

[4] The section is based on the article about the gas-phase protolysis of trisarylzincate anions which the author of this work had published. See reference [102].

The zincates were prepared in solution under inert-gas conditions by treating a solution of $ZnCl_2$ in THF with phenyllithium (PhLi) and/or the *para*-substituted arylmagnesium bromides (Ar^{X}MgBr). They were then injected into the ESI source of a commercial 3D quadrupole ion trap (QIT) mass spectrometer. First, mass spectra (MS^1) of the solutions were recorded. Afterwards, kinetic measurements (MS^n) for the ion-molecule reaction of the mass-selected trisarylzincate anion with an excess of 2,2,2-trifluoroethanol (R^{F3}OH) were performed.[5]

In the mass spectrum of the solution of $ZnCl_2$ and PhLi (4 equiv.), only Ph$_3$Zn$^-$ was found (Figure 12, left). In the reaction of mass-selected Ph$_3$Zn$^-$ with R^{F3}OH the expected reaction was observed. Ph$_3$Zn$^-$ is protolyzed by R^{F3}OH to give the organozincate anion (R^{F3}O)ZnPh$_2^-$ and by means of mass balance benzene (PhH) which could, of course, be not measured mass-spectrometrically due to the lack of charge. Within a reaction time of $t = 2000$ ms, the reactant was consumed almost entirely. Consecutive protonation reactions giving (R^{F3}O)$_2$ZnPh$^-$ or (R^{F3}O)$_3$Zn$^-$ were not observed. Another minor reaction channel was found: The triphenylzincate anion Ph$_3$Zn$^-$ reacted with residual formic acid (HCOOH) in a protolysis reaction to give (HCOO)ZnPh$_2^-$ and benzene. Unfortunately, the formic acid posed a contamination from former measurements and could not be removed entirely.
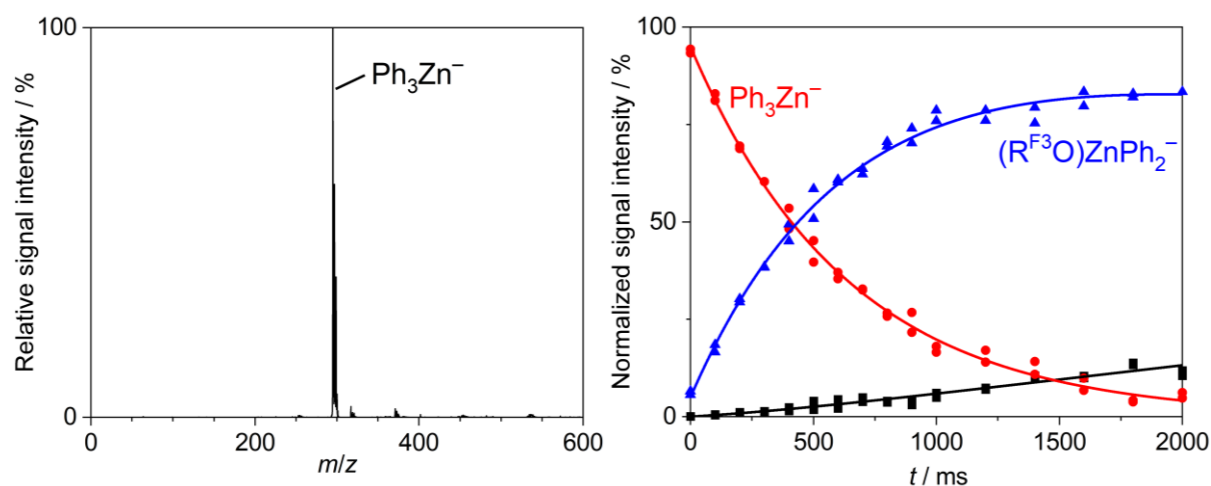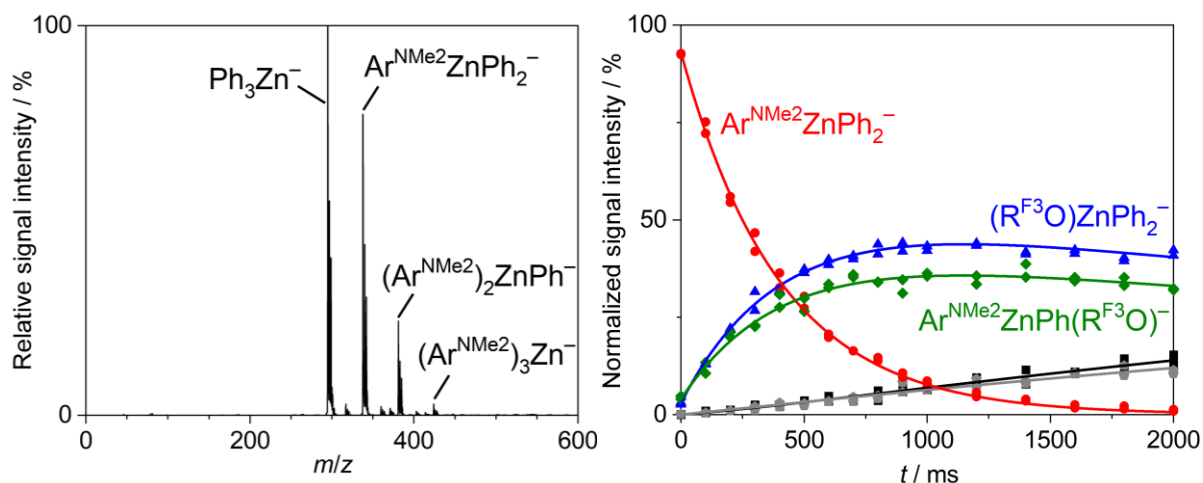

Figure 12:   Left: Negative ion-mode electrospray ionization (ESI) mass spectrum (MS^1) of a solution of the products formed in the reaction of $ZnCl_2$ with PhLi (4 equiv.) in THF (20 mM) at 273 K. Right: Kinetic measurement (MS^2) of the gas-phase reaction of mass-selected Ph$_3$Zn$^-$ with 2,2,2-trifluoroethanol (R^{F3}OH; $N_{substrate}/V = 8.5 \times 10^{10}$ cm^{-3}). Due to contaminant formic acid (HCOOH) in the QIT, (HCOO)ZnPh$_2^-$ (black) forms as a side product which was accounted for in the kinetic modelling. Adapted with permission from reference [102]. Copyright 2023 American Chemical Society.

In addition to the qualitative investigations, reactions were also probed in a quantitative manner. The kinetic data were fitted to a conceived reaction network to give the effective reaction rate constant (pseudo-first order). Knowing the partial pressure of the substrate R^{F3}OH, the effective rate constant for the protonation by R^{F3}OH was converted into a bimolecular rate constant k_{exp} for the reaction temperature $T = (310 \pm 20)$ K.[97,101,136] [5] For the protolysis of Ph$_3$Zn$^-$ the bimolecular rate constants were determined to be $k_{exp} = 1.6 \times 10^{-11}$ cm^3 s^{-1} (Figure 12, right). The rate constant was transformed into a reaction efficiency of $\varphi_{exp} = 1.3\%$ by dividing it through the collision rate according to the

---

[5] For details about the experimental methods, consult section 5.1.

capture theory by Su and Chesnavich.[123,124] [6] The low reaction efficiency indicates a significant central barrier associated with the protonation reaction.

In an analogous fashion, mass-spectrometric experiments were carried out for the *para*-substituted trisarylzincate anions, $Ar^XZnPh_2^-$ (X = NMe_2, OMe, Me, F, Cl). The two extreme cases featuring the most electron-donating and withdrawing groups of X = NMe_2 and Cl, respectively, are described in detail.

In the mass spectrum of the solution of $ZnCl_2$ with PhLi (2 equiv.) and $Ar^{NMe2}MgBr$ (2 equiv.), the two homoleptic species Ph_3Zn^- and $(Ar^{NMe2})_3Zn^-$ as well as the two heteroleptic anions $Ar^{NMe2}ZnPh_2^-$, $(Ar^{NMe2})_2ZnPh^-$ were found. The intensity distribution does not obey statistics, but instead the dominating species were those featuring more phenyl and less aryl moieties (Figure 13, left). Under the assumption of very similar ESI activities, the observation expresses different efficiencies of the transmetalation from PhLi and $Ar^{NMe2}MgBr$, respectively, to Zn^{2+} in solution.

In the ion-molecule reaction (IMR) of the mass-selected dimethylamino-substituted species $Ar^{NMe2}ZnPh_2^-$ with the proton donor $R^{F3}OH$, the two competing reaction pathways of aryl and phenyl protonation were found which yielded either $(R^{F3}O)ZnPh_2^-$ (and $Ar^{NMe2}H$) or $Ar^{NMe2}ZnPh(R^{F3}O)^-$ (and PhH). The protonation at the Ar site was found to be the major reaction pathway. The dominance of that pathway is even more remarkable if the statistical bias is considered because the trisarylzincate anion $Ar^{NMe2}ZnPh_2^-$ features only one Ar^{NMe2} but two Ph groups. Apparently, the NMe_2 groups facilitate the proton transfer to the aryl group. Moreover, the corresponding formate-containing species $(HCOO)ZnPh_2^-$ and $Ar^{NMe2}ZnPh(HCOO)^-$ were observed due to the side reaction with contaminant HCOOH (Figure 13, right).
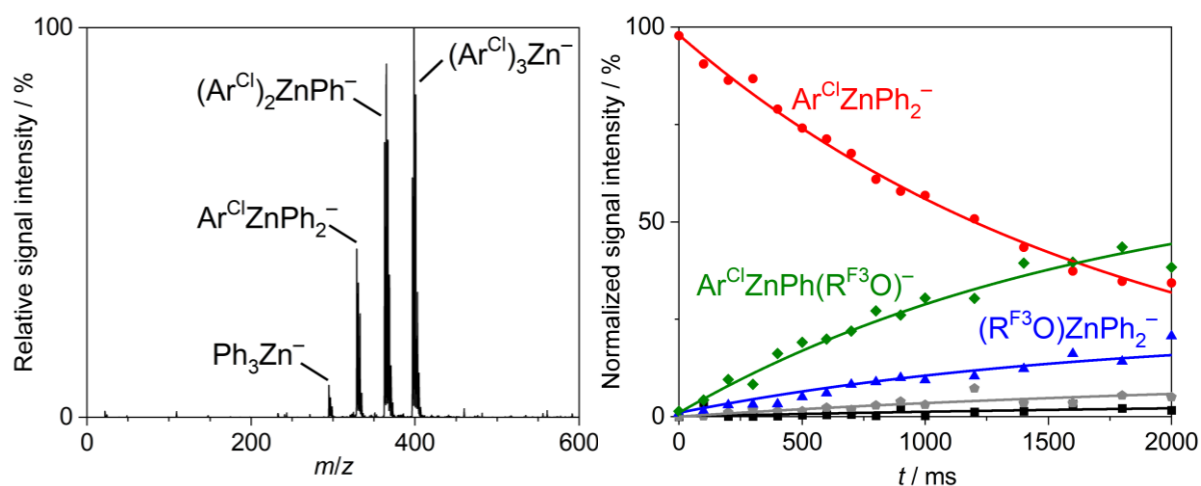

Figure 13:   Left: Negative ion-mode electrospray ionization (ESI) mass spectrum (MS[1]) of a solution of the products formed in the reaction of $ZnCl_2$ with PhLi (2 equiv.) and $Ar^{NMe2}MgBr$ (2 equiv.) in THF (20 mM) at 273 K. Right: Kinetic measurement (MS[2]) of the gas-phase reaction of mass-selected $Ar^{NMe2}ZnPh_2^-$ with 2,2,2-trifluoroethanol ($R^{F3}OH$; $N_{substrate}/V$ = 8.5 × 10^10 cm^−3). Due to contaminant formic acid (HCOOH) in the QIT, side products (black, gray) form which were accounted for in the kinetic modelling. Adapted with permission from reference [102]. Copyright 2023 American Chemical Society.

Over the course of the reaction time (t = 2000 ms), total conversion of the reactant was found. The experimental rate constants k_{exp} (and reaction efficiencies φ) for the Ar^{NMe2} and Ph protonations were determined as 1.5 × 10^−11 cm^3 s^−1 (1.3%) and 1.2 × 10^−11 cm^3 s^−1

---

[6] The calculation of the theoretical collision rates is detailed in section 5.2.2.1.

(1.0%), respectively. The organozincate anions $Ar^{NMe2}ZnPh_2^-$ is approx. 80% more reactive than the triphenylzincate Ph_3Zn^-. The NMe_2 group seems to activate the organometallic species for its protonation.

In the mass spectrum of the solution of $ZnCl_2$, PhLi (3 equiv.) and $Ar^{Cl}MgBr$ (1 equiv.), the species with more Ar^{Cl} and less Ph moieties are in higher abundance. In fact, the ratio of the transmetalation reagents had to be changed (from 2:2 to 3:1) because otherwise the species of interest $Ar^{Cl}ZnPh_2^-$ was not obtained in sufficient yield. It appears that the formation of the trisarylzincate anions featuring more Ar^{Cl} groups is favored (Figure 14, left).

The kinetic measurement for the protolysis reaction of $Ar^{Cl}ZnPh_2^-$ by $R^{F3}OH$ showed, again, the protonation of both the aryl and phenyl moieties. This time, the proton transfer to the phenyl groups was dominant. For the Ar^{Cl} protonation the experimental rate constant (reaction efficiency) was 1.4×10^{-12} cm^3 s^{-1} (0.1%) and for the phenyl protonation 4.6×10^{-12} cm^3 s^{-1} (0.4%). The findings as well as the overall lower reaction conversion (only 60% within 2000 ms) suggest that the *para*-substituent Cl as an EWG deactivates the aryl group and the entire trisarylzincate anion for protonation (Figure 14, right).

Figure 14: Left: Negative ion-mode electrospray ionization (ESI) mass spectrum (MS^1) of a solution of the products formed in the reaction of $ZnCl_2$ with PhLi (3 equiv.) and $Ar^{Cl}MgBr$ (1 equiv.) in THF (20 mM) at 273 K. Right: Kinetic measurement (MS^2) of the gas-phase reaction of mass-selected $Ar^{Cl}ZnPh_2^-$ with 2,2,2-trifluoroethanol ($R^{F3}OH$; $N_{substrate}/V = 8.5 \times 10^{10}$ cm^{-3}). Due to contaminant formic acid (HCOOH) in the QIT, side products (black, gray) form which were accounted for in the kinetic modelling. Adapted with permission from reference [102]. Copyright 2023 American Chemical Society.

Such kinetic measurements were carried out for all other para-substituents and their experimental bimolecular rate constants k_{exp} determined. The experimental uncertainties given correspond to the 95% confidence interval (2σ) from two independent kinetic measurements (statistical error). The systematic error is estimated at ±30%.[101]

The rate constants for both the aryl and phenyl protonation, k_{exp}^{Ar} and k_{exp}^{Ph}, were normalized with regards to the number of Ar^X and Ph moieties of the trisarylzincate, n_{Ar} and n_{Ph}, respectively. The logarithms of the normalized rate constants were correlated with the Hammett parameter σ_p.[18–20,22] Figure 15 shows the Hammett plots for the proton-transfer to the aryl and phenyl sites, respectively. In both cases, the rate constants decrease with increasing Hammett parameters. Disregarding the data points for NMe_2, the data were fairly well fitted with linear regressions featuring negative slopes m and intercepts b. In the case of the aryl protonation the slope is more negative ($m = -1.74$) than for the phenyl

protonation ($m = -0.76$). The negative slopes in the Hammett plots mean that EWG (EDG) decelerate (accelerate) the protonation reaction and hamper (facilitate) the proton transfer.
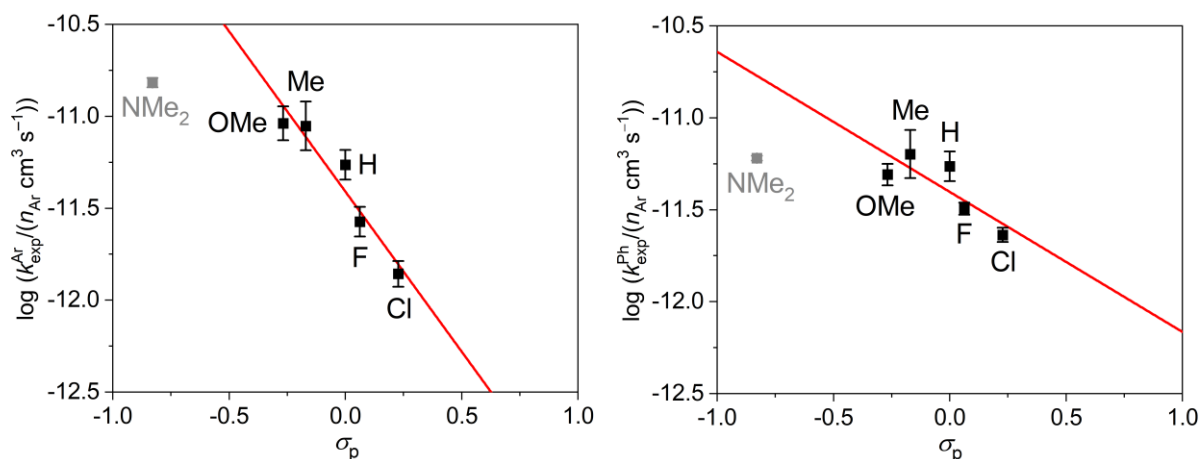

Figure 15:   Correlation of the logarithm of the experimental rate constants k_{exp} for the protonation at the Ar^X (left) or Ph (right) site of the denoted $Ar^X ZnPh_2^-$ with the Hammett parameter σ_p. The experimental rate constants were normalized with regards to the number of Ar^X and Ph moieties of the organozincate anion n_{Ar} and n_{Ph}, respectively. The experimental uncertainties correspond to the 95% confidence interval from two independent measurements. Disregarding the data point for NMe_2 (gray), the data points (black) can be fitted with a linear regressions (left: slope $m = -1.74$, intercept $b = -11.4$, $R^2 = 0.89$; right: $m = -0.76$, $b = -11.4$, $R^2 = 0.56$). Adapted with permission from reference [102]. Copyright 2023 American Chemical Society.

For deeper insight into the intrinsic reactivity of the trisarylzincate anions, the reaction pathways for their aryl and phenyl protonations were computed with quantum-chemical methods using the software package ORCA 4.2.1.[116,117] Structures were optimized with the long-range corrected hybrid density functional ωB97X-D3[137–139] and Ahlrichs' def2-TZVP basis sets[140] as intermolecular interactions are decisive for ion-molecule reactions involving polar and hydrogen-bond forming molecules. Subsequently, electronic single-point calculations were carried out the coupled-cluster method DLPNO-CCSD(T)[110,111] and Dunning's correlation-consistent cc-pVnZ basis sets extrapolated to the complete basis set limit (n = 3, 4).[141–144] [7]

From the quantum-chemical calculation of the pathway for the reaction of Ph_3Zn^- with 2,2,2-trifluoroethanol ($R^{F3}OH$) a double-well potential in terms of the enthalpy at 0 K, ΔH_0, was obtained. This is typical for many ion-molecule reactions in the gas phase (cf. section 1.1.2.2). Given the microcanonical nature of the reaction ensemble under low-pressure conditions, the enthalpy ΔH_0 (and not the Gibbs energy at 310 K, ΔG_{310}) is the most representative energy for the description of the reaction (cf. section 1.2.2.2).

In the first step, the reactants Ph_3Zn^- and $R^{F3}OH$ (1) form the pre-reactive complex (2) which is stabilized by intermolecular interactions of the hydroxyl group of $R^{F3}OH$ with the metal center ($\Delta H_0 = -49$ kJ mol^{-1}). Subsequently, the proton transfer occurs and the pre-reactive complex reacts to the product complex (3) via the transition structure (TS). The TS is four-membered ($Zn-O(R^{F3})-H-C(Ph)$) and features one imaginary frequency (approx. -1000 cm^{-1}) which corresponds to the motion of the proton between the donor oxygen and the acceptor carbon atom. The TS can be deemed as "early" because the O–H bond length in the hydroxyl group of the alcohol is close to that in free $R^{F3}OH$ (1.16 Å vs. 0.96 Å). Although the proton transfer is associated with a net energy gain of $\Delta\Delta H_0 =$

---

[7] For further information about the quantum-chemical methods, see section 5.2.

−92 kJ mol^{-1}, it still features a pronounced central barrier of $\Delta H_0^\ddagger = -20$ kJ mol^{-1}. In the last step, the product complex dissociates into the products (R^{F3}O)ZnPh$_2^-$ and benzene (PhH) for which an energy of $\Delta\Delta H_0 = +32$ kJ mol^{-1} is required to overcome the stabilization by intermolecular interactions. The protolysis reaction is overall exothermic with a reaction enthalpy of $\Delta_r H_0 = -109$ kJ mol^{-1} (Figure 16).
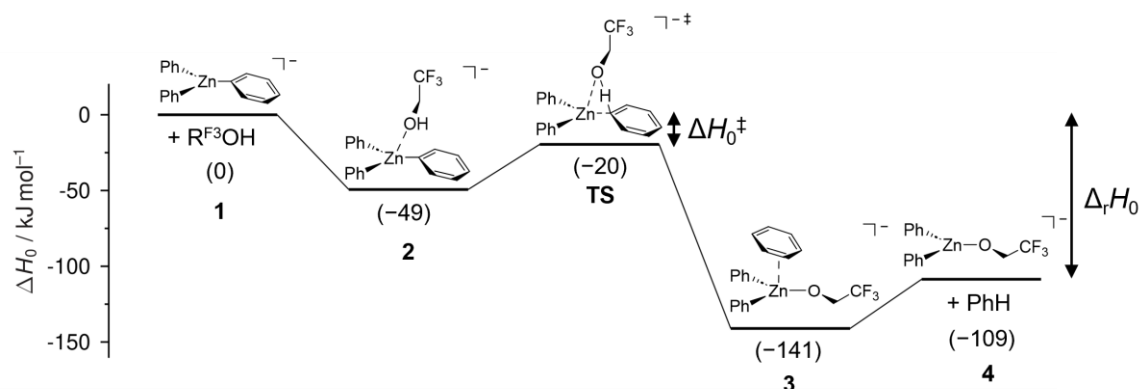

Figure 16: Reaction pathway for the protonation reaction of Ph$_3$Zn$^-$ with 2,2,2-trifluoroethanol (R^{F3}OH) as obtained from quantum-chemical calculations (DLPNO-CCSD(T)/cc-pV[T;Q]Z//ωB97X-D3/def2-TZVP). The energy profile poses a double-well potential which is typical for gas-phase ion-molecule reactions. Energies are given as enthalpies at 0 K relative to the reactants, ΔH_0. The reaction is exothermic ($\Delta_r H_0 = -109$ kJ mol^{-1}) and features the central barrier $\Delta H_0^\ddagger$ of −20 kJ mol^{-1}. Adapted with permission from reference [102]. Copyright 2023 American Chemical Society.

To assess the reliability of the computed energies, elasticity tests were performed by carrying out electronic single-point energy calculations with other methods as well. First, the energies of the stationary points were computed with the double-hybrid density functional DSD-PBEP86[145] and def2-TZVP basis sets. For the product complex and products, the energies of the DLPNO-CCSD(T) and DSD-PBEP86 agreed well ($\Delta\Delta H_0 \leq$ 2 kJ mol^{-1}). However, for the pre-reactive complex and the TS the DSD-PBEP86 energies were lower by 6 and 11 kJ mol^{-1}, respectively. Further test calculations addressed the influence of relativistic effects of the metal center by the application of the zeroth-order relativistic approximation (ZORA) to the ωB97X-D3/def2-TZVP calculations. Furthermore, augmented correlation-consistent basis sets aug-cc-pVnZ[146] (n = 3; 4) were applied to the DLPNO-CCSD(T) calculations as the organozincate species are anions which in some cases are better described by augmented basis sets. It was found that neither relativistic effects nor augmented basis sets change the central barrier significantly ($\Delta\Delta H_0 =$ 2 kJ mol^{-1}). Given that the DLPNO-CCSD(T) method is known to provide accurate and reliable results[147–149] and that the use of augmented basis sets results in much higher computational costs, the energies of the DLPNO-CCSD(T)/cc-pV[T;Q]Z calculations were used for further analysis.

Following the protocol of structure optimization with the functional ωB97X-D3 and def2-TZVP basis sets and subsequent electronic single-point energy calculations with the method DLPNO-CCSD(T)/cc-pV[T;Q]Z, the reaction pathways for the Ar^X and Ph protonation of the organozincate anions Ar^{X}ZnPh$_2^-$ (X = OMe, Me, H, F, Cl) were calculated.

In the case of the Ar^X protonation, double-well potentials were obtained in line with expectations. The mechanisms of the protonation reactions were the same for all trisarylzincate anions considered although the energies of the stationary points were

affected (Figure 17). The *para*-substituents changed the energies of the pre-reactive complex and TS only to a minor extent ($\Delta\Delta H_0 \leq 3$ kJ mol^{-1}) but those of the product complex and products considerably ($\Delta\Delta H_0 \leq 13$ kJ mol^{-1}). The fact that the species which occur late in the reaction are affected more by the *para*-substituent than the early ones shall be noted. The correlation of the central barrier $\Delta H_0^{\ddagger,Ar}$ with the reaction energy $\Delta_r H_0^{Ar}$, which is related to a Brønsted plot, where log k and log K are considered, shows that the central barrier depends on the reaction energy. EWG (F, Cl) decrease the exothermicity and thereby raise the reaction barrier. In contrast, EDG increase the exothermicity and lower the central barrier (Figure 18, left). The data can be fitted with a linear regression featuring a slope of m = +0.19±0.04 meaning that the change in the reaction energy affects the reaction barrier by only one fifth. Here, a clear connection between the thermochemistry and kinetics within the same set of reactions is found. This is a gas-phase example of the Bell-Evans-Polanyi principle and the Hammond-Leffler postulate (cf. section 1.1.2.1). Moreover, the intercept is interesting which is b = 0±5. As it describes the central barrier $\Delta H_0^{\ddagger,Ar}$ for the (hypothetical) thermoneutral reaction ($\Delta_r H_0^{Ar}$ = 0) of Ar^{X}ZnPh$_2^-$ by R^{F3}OH, it can be interpreted as the intrinsic barrier in terms of the Marcus' theory.
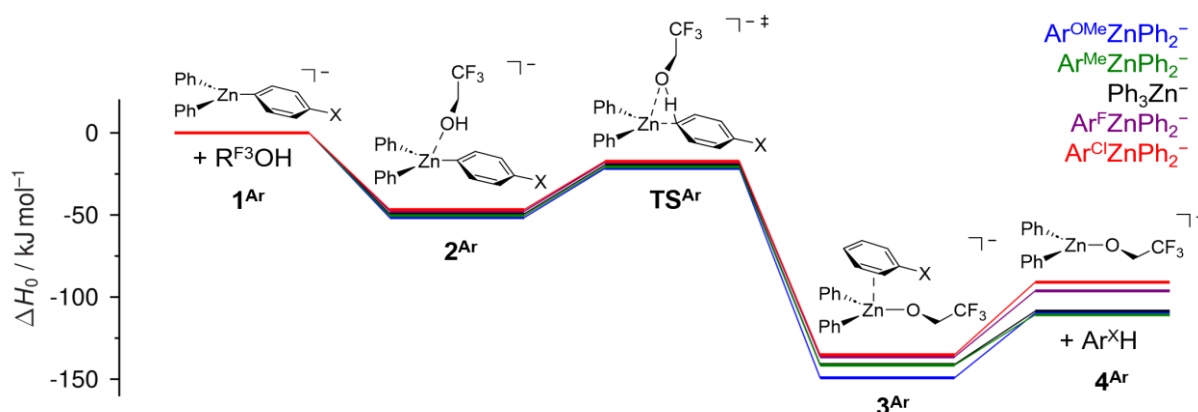
Figure 17: Reaction pathways for the protonation of the aryl moiety of the *para*-substituted trisarylzincate anions Ar^{X}ZnPh$_2^-$ (X = OMe, Me, H, F, Cl) by 2,2,2-trifluoroethanol (R^{F3}OH) as obtained from quantum-chemical calculations (DLPNO-CCSD(T)/cc-pV[T;Q]Z//ωB97X-D3/def2-TZVP). Adapted with permission from reference [102]. Copyright 2023 American Chemical Society.

Based on the calculated structures and energies along the reaction pathways, theoretical rate constants for the protonation of Ar^{X}ZnPh$_2^-$ (X = OMe, Me, H, F, Cl) at the Ar^X site, k_{theo}^{Ar}, were calculated using the Master equation solver MESMER by Glowacki and co-workers[131] under low-pressure conditions and assuming classical statistical mechanics, i.e. without quantum effects such as proton tunneling. The applied reaction scheme for the kinetic simulation was simplified by removing the product complex from the double-well potential, so that the TS leads directly to the products. The approximation appears well justified given that the proton transfer is the rate-determining step in the protonation reaction.[8] The obtained theoretical rate constants k_{theo}^{Ar} proved to be very sensitive towards the central barrier $\Delta H_0^{\ddagger}$, but negligibly sensitive towards the energy of the pre-reactive complex and not at all affected by the exothermicity. The theoretical rate constants k_{theo}^{Ar} were normalized with regards to the number of aryl moieties n_{Ar}. The temperature uncertainty (T = (310 ± 20) K) was accounted for in the kinetic modelling. The logarithmic normalized rate constants were correlated against the Hammett parameter σ_p. The linear

---

[8] The kinetic simulations are explained in detail in section 5.2.2.

fit of the data features a slope of $m = -1.48$ which indicates that EDG (EWG) increase (decrease) the rate constant (Figure 18, right). Apparently, the electron-donating (withdrawing) nature of the *para*-substituents X lower (raise) the central barrier and thus, speed up (slow down) the proton-transfer reaction. To this point, the theoretical and experimental results for the protonation of the aryl group agree qualitatively.
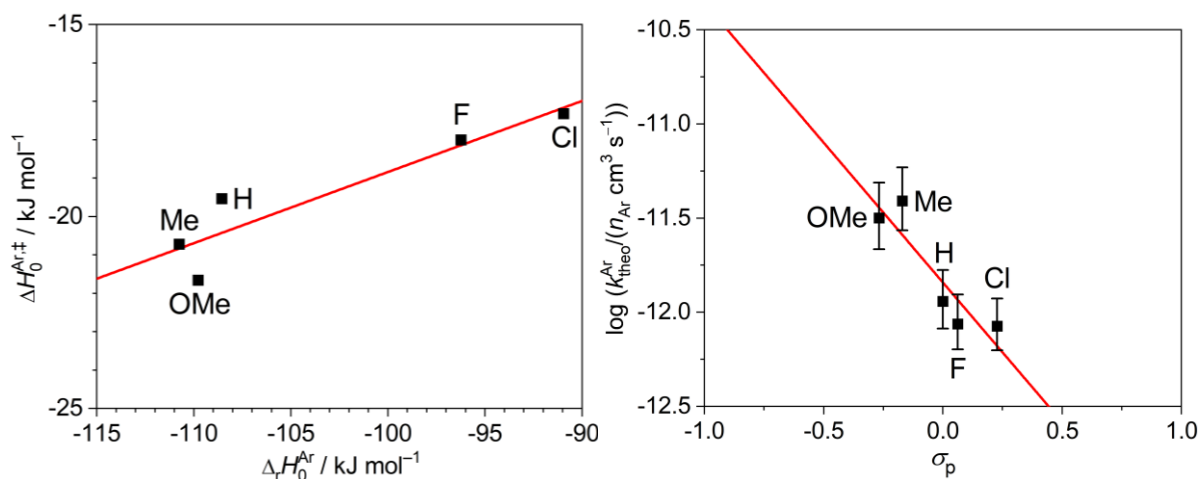

Figure 18:   Left: Correlation of the computed central barrier $\Delta H_0^{Ar,\ddagger}$ with the reaction energy $\Delta_r H_0^{Ar}$ for the protonation of the *para*-substituted trisarylzincate anions $Ar^X ZnPh_2^-$ (X = OMe, Me, H, F, Cl) by 2,2,2-trifluoroethanol ($R^{F3}OH$) at the aryl site. The data points can be fitted by a linear regression ($m = +0.19$, $b = 0$, $R^2 = 0.81$). Right: Correlation of the logarithm of the normalized theoretical rate constants k_{theo}^{Ar} for the protonation at the aryl site of the denoted $Ar^X ZnPh_2^-$ species with the Hammett parameter σ_p. The data points are fitted with a linear regressions ($m = -1.48$, $b = -11.8$, $R^2 = 0.76$). Adapted with permission from reference [102]. Copyright 2023 American Chemical Society.

Analogous studies were conducted for the protonation of $Ar^X ZnPh_2^-$ (X = OMe, Me, H, F, Cl) at the phenyl site. The findings were similar to those for the Ar^X protonation, although they were less pronounced (Figure 19, Figure 20).

Apparently, the substituent X in the *para*-position of one aryl moiety of the trisarylzincate anions $Ar^X ZnPh_2^-$ exerts a stronger direct and a weaker indirect effect onto the reactivity of the species. One rationalization for the observed structure-reactivity relationship of the trisarylzincate anions towards protonation relies on the partial charges in the species. The direct effect might be explained as follows: The more electron donating the *para*-substituent is, the higher is the electron density at the carbon atom of the aryl residue which is coordinated to the zinc center and is accepting the proton of the donor $R^{F3}OH$. The higher electron density at the accepting carbon atom promotes the proton transfer. The hypothesis is supported by the atomic charges that were calculated for the accepting carbon atom of the aryl group employing the natural population analysis (NPA) scheme by Weinhold.[150] Their negative partial charges decrease from X = OMe (−0.632) to X = Cl (−0.580).

The afore-mentioned indirect effect is easily explained taking into account that electron-donating (-withdrawing) groups increase (decrease) the electron density at the proton-accepting site of the Ar^X substituent which also leads, mediated by the metal center, to higher electron densities at the basic sites of the Ph moieties.
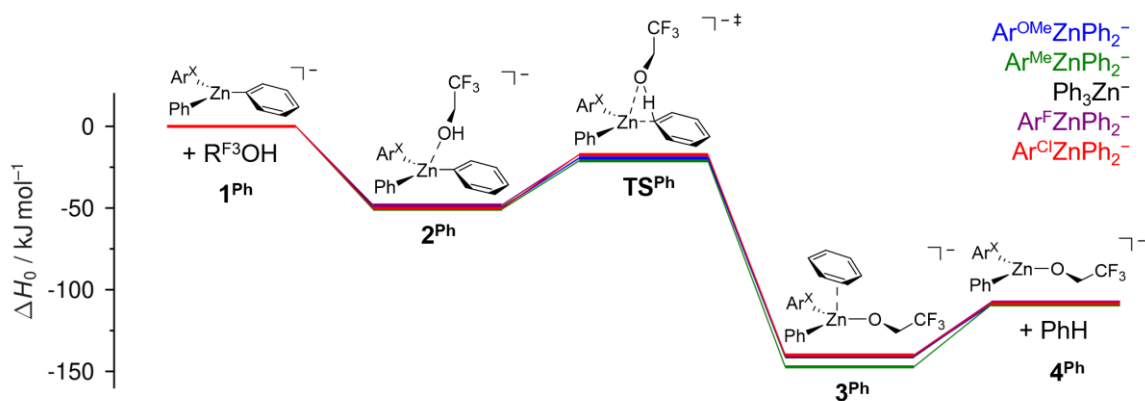
Figure 19: Reaction pathways for the protonation of the phenyl moiety of the *para*-substituted trisarylzincate anions $Ar^XZnPh_2^-$ (X = OMe, Me, H, F, Cl) by 2,2,2-trifluoroethanol ($R^{F3}OH$) as obtained from quantum-chemical calculations (DLPNO-CCSD(T)/cc-pV[T;Q]Z//ωB97X-D3/def2-TZVP). Adapted with permission from reference [102]. Copyright 2023 American Chemical Society.
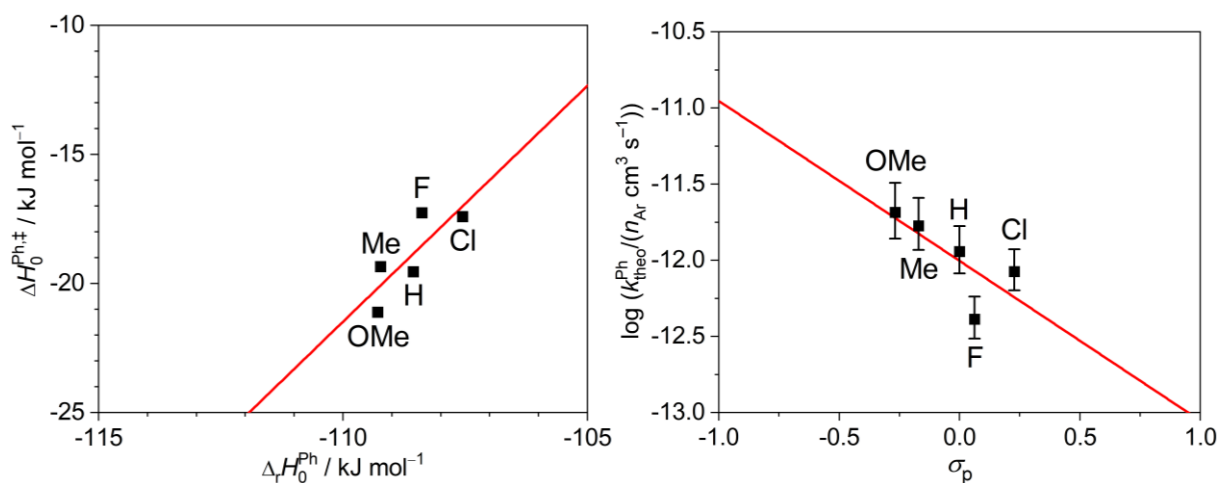

Figure 20: Left: Correlation of the computed central barrier $\Delta H_0^{Ph,\ddagger}$ with the reaction energy $\Delta_r H_0^{Ph}$ for the protonation of the *para*-substituted trisarylzincate anions $Ar^XZnPh_2^-$ (X = OMe, Me, H, F, Cl) by 2,2,2-trifluoroethanol ($R^{F3}OH$) at the phenyl site. The data points can be fitted by a linear regression (*m* = +1.83, *b* = 180, R^2 = 0.53). Right: Correlation of the logarithm of the normalized theoretical rate constants k_{theo}^{Ph} for the protonation at the phenyl site of the denoted $Ar^XZnPh_2^-$ species with the Hammett parameter σ_p. The data points are fitted with a linear regressions (*m* = −1.05, *b* = −12.0, R^2 = 0.40). Adapted with permission from reference [102]. Copyright 2023 American Chemical Society.

After establishing the qualitative agreement of experiment and theory, the experimental and theoretical rate constants k_{exp} and k_{theo} were compared quantitatively. Thereby, the performance of the applied quantum-chemical methods and the suitability of the kinetic simulations were assessed. The theoretical and experimental rate constants deviated by factors of only 2–3 and 2–8 for the protonation of the Ar^X and Ph moieties, respectively, which is within one order of magnitude. Interestingly, the theoretical rate constants were always found to be lower than their experimental congeners. As the consideration of the temperature uncertainty (*T* = (310 ± 20) K) in the theoretical modelling translates only into relative uncertainties in k_{theo} of less than ±30%, they can be disregarded for the comparison of the experimental and theoretical rate constants because their deviations are significantly larger (Figure 21).
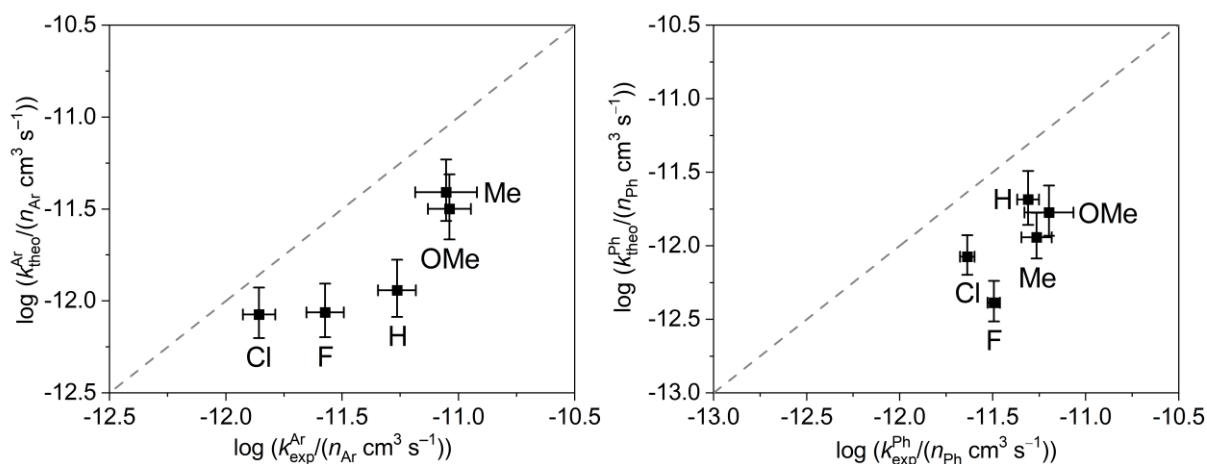
Figure 21: Comparison of the experimental and theoretical rate constants for the protonation of the *para*-substituted trisarylzincate anions $Ar^XZnPh_2^-$ (X = OMe, Me, H, F, Cl) at the Ar^X (left) and Ph site (right). The rate constants were normalized with regards to the number of Ar^X and Ph moieties of the organozincate anions n_{Ar} and n_{Ph}, respectively. The gray dashed line represents ideal agreement between experiment and theory. Adapted with permission from reference [102]. Copyright 2023 American Chemical Society.

To evaluate how the deviations of the rate constants translate into deviations of the barrier heights, the dependence of the central barrier $\Delta H_0^\ddagger$ on the theoretical rate constant k_{theo} was studied for the reaction of Ph_3Zn^- with $R^{F3}OH$. The central barrier was systematically decreased to the energy of the pre-reactive complex ($\Delta H_0^\ddagger = -49$ kJ mol^{-1}) on the one hand and increased up to the energy level of the reactants ($\Delta H_0^\ddagger = 0$ kJ mol^{-1}) at the other. The obtained correlation of k_{theo} and $\Delta H_0^\ddagger$ approaches two limits: For very low central barriers the theoretical rate constant converges towards the collision rate limit. In contrast, barriers higher than -5 kJ mol^{-1} result in reactions too slow to be observed within the experimental time frame (Figure 22). The correlation reveals to regimes of the kinetic simulation:

- For low barriers the reaction rate is dominated by the collision rate and thus, the reaction is kinetically governed by the formation of the pre-reactive complex (Figure 22, red).
- For higher central barriers ($\Delta H_0^\ddagger > -25$ kJ mol^{-1}) the rate constant scales linearly with the barrier height indicating that the proton transfer is the kinetically governing process of the reaction (Figure 22, blue).

The findings are fully in line with the concept to describe the reaction rate constant as the result of the collision rate as modelled by the capture theory and the proton-transfer rate as modelled by the RRKM theory (cf. section 1.2.2.2).

The scaling was then used to convert the deviating factors from the comparison of the theoretical and experimental rate constants into differences in the computed barrier heights. It was found that deviations by factors of up to 5 correspond to energy differences of less than 4 kJ mol^{-1}. In this regard, for all systems but the phenyl protonation in $Ar^FZnPh_2^-$ agreement within the limit of chemical accuracy ($\Delta E_{exp\text{-}theo} < 4$ kJ mol^{-1}) was achieved. The scaling of the activation barrier on the rate constant of the microcanonical ensemble could be described fairly well by the Boltzmann factor $\exp(-\Delta H_0^\ddagger/RT)$ with R being the universal gas constant and $T = 310$ K for canonical ensembles in the linear regime. The coincidental agreement probably holds true only within the linear regime and in close proximity to the reference point $\Delta H_0^\ddagger = -20$ kJ mol^{-1}.
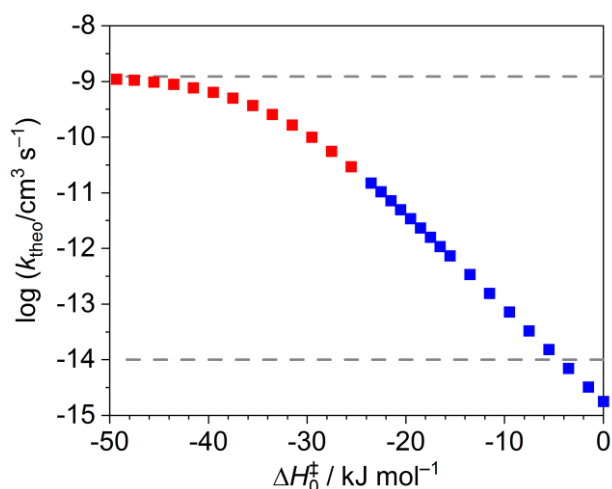
Figure 22:   Scaling study for the dependence of the logarithm of the theoretical rate constant k_{theo} on the calculated central barrier $\Delta H_0^{\ddagger}$. For vanishingly small central barriers ($\Delta H_0^{\ddagger} \rightarrow -49$ kJ mol^{-1}), the rate constant is dominated by the capture rate (red) featuring the collision rate limit (upper gray dashed line). For $\Delta H_0^{\ddagger} > -25$ kJ mol^{-1} the logarithmic rate constant depends linearly on the central barrier (blue). Central barriers higher than -5 kJ mol^{-1} will give rate constants too slow to be observed in the experiment (lower gray dashed line).

Unfortunately, the reaction pathways for the dimethylamino-substituted system Ar^{NMe2}ZnPh$_2^-$ were not calculated as the transition states could not be located. One reason is the higher computational cost for the quantum-chemical calculations due to the NMe$_2$ *para*-substituent. Another reason presumably is that the central barrier for the TS is very low as a consequence of the strong electron-donating effect of X = NMe$_2$ and thus, the potential energy surface is likely to be very flat around the transition state which renders the search of the TS difficult. However, the central barriers $\Delta H_0^{\ddagger}$ for the protonation of Ar^{NMe2}ZnPh$_2^-$ by R^{F3}OH at the aryl and phenyl site could be determined indirectly using the linear energy relationship between the Hammett parameter σ_p(NMe$_2$) = -0.83 and the normalized rate constant k_{exp}/n_{Ar} (Figure 15) as well as the scaling study (Figure 22). The central barriers $\Delta H_0^{\ddagger}$ for the Ar^X and Ph protonation were determined to be approx. -27 and -22 kJ mol^{-1}, respectively. Due to the low central barrier the rate constant is no longer governed by the barrier height but rather by the collision rate. The finding also explains why the data points for X = NMe$_2$ in the experimental Hammett plots (Figure 15) do not match the linear trend of the other substituents.

Table 1: Results of the quantum-chemical calculations of the reaction pathways for the protonation of the trisarylzincate anions $Ar^XZnPh_2^-$ by 2,2,2-trifluoroethanol ($R^{F3}OH$). Structures were computed with the DFT functional ωB97X-D3 and def2-TZVP basis sets, electronic single point energies were calculated with the method DLPNO-CCSD(T) and cc-pV[T;Q]Z basis sets if not noted otherwise. Energies are given as enthalpies at 0 K relative to the reactants, ΔH_0, in kJ mol^{-1}.

| X | site | ΔH_0[a] / kJ mol^{-1} | | | |
		Pre-reactive complex	TS	Product complex	Products
NMe$_2$	Ar^X	--	-27[b]	--	--
	Ph	--	-22[b]	--	--
OMe	Ar^X	-52	-22	-149	-110
	Ph	-50	-19	-141	-109
Me	Ar^X	-50	-20	-141	-111
	Ph	-51	-21	-147	-109
H	Ph	-49	-20	-141	-109
H[c]	Ph	-55	-25	-148	-114
H[d]	Ph	-55	-31	-148	-107
F	Ar^X	-48	-18	-136	-96
	Ph	-48	-17	-140	-108
Cl	Ar^X	-47	-17	-135	-91
	Ph	-50	-17	-140	-108

[a] DLPNO-CCSD(T)/cc-pV[T;Q]Z//ωB97X-D3(def2-TZVP). [b] Central barriers were determined indirectly from the use of linear energy relationships and scaling study. [c] ωB97X-D3/def2-TZVP. [d] DSD-PBEP86/def2-TZVP//ωB97X-D3/def2-TZVP.

Table 2: Experimental and theoretical rate constants k_{exp} and k_{theo} for the protonation at the aryl and phenyl site of the trisarylzincate anions $Ar^XZnPh_2^-$ by 2,2,2-trifluoroethanol ($R^{F3}OH$). The theoretical rate constants were obtained from Master equation calculations based on DLPNO-CCSD(T)/cc-pV[T;Q]Z/ωB97X-D3/def2-TZVP reaction pathways and for the assumed reaction temperatures of 310, 330 and 290 K, respectively. Adapted with permission from ref. [102]. Copyright 2023 American Chemical Society.

X	Site	k_{exp}[a,b] / 10^{-12} cm^3 s^{-1}	φ_{exp}[c]/ %	k_{theo}[d] / 10^{-12} cm^3 s^{-1}[d]	k^{min}_{theo}[d] / 10^{-12} cm^3 s^{-1}	k^{max}_{theo}[d] / 10^{-12} cm^3 s^{-1}
NMe$_2$	Ar^X	15 ± 1	1.3	--	--	--
	Ph	12 ± 0	1.0	--	--	--
OMe	Ar^X	9.2 ± 2.2	0.8	3.2	2.2	4.9
	Ph	9.8 ± 1.4	0.8	4.1	2.8	6.4
Me	Ar^X	8.9 ± 3.2	0.7	3.9	2.7	5.9
	Ph	13 ± 4	1.0	3.4	2.3	5.1
H	Ph	16 ± 3	1.3	3.4	2.5	5.0
F	Ar^X	2.7 ± 0.6	0.2	0.87	0.64	1.2
	Ph	6.4 ± 0.5	0.5	0.82	0.61	1.2
Cl	Ar^X	1.4 ± 0.2	0.1	0.90	0.67	1.3
	Ph	4.6 ± 0.4	0.4	1.7	1.3	2.4

[a] The experimental uncertainty corresponds to the statistical error from two independent measurements (95% confidence interval). [b] The experimental rate constants stem from the fit of the experimental data without consideration of the statistical factors. [c] The reaction efficiency φ_{exp} was calculated by dividing the experimental rate constant by the collision rate according to the capture theory by Su and Chesnavich. [d] In the theoretical modelling of the reaction kinetics, the symmetry number was taken into account.

After elucidating the intrinsic reactivity of zincates with C(sp^2) bases, the reactivity of the homoleptic trisalkylzincate anions R$_3$Zn$^-$ (R = Me, Et) with C(sp^3) bases was investigated. Their reaction with 2,2,2-trifluoroethanol (R^{F3}OH) gave the corresponding alkanes RH and the zincate species (R^{F3}O)ZnR$_2^-$ (Scheme 8).
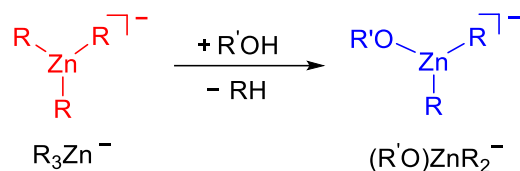
Scheme 8:   Protolysis reactions of the homoleptic trisalkylzincate anions R$_3$Zn$^-$ (R = Me, Et) by 2,2,2-trifluoroethanol (R^{F3}OH). The protonation of one of the alkyl substituents yields the corresponding alkane RH and the alkoxide-containing zincate (R^{F3}O)ZnR$_2^-$.

At first, the intrinsic reactivity of the trismethylzincate anion Me$_3$Zn$^-$ was studied. It was prepared from electrospraying a solution of ZnMe$_2$ and MeLi (2 equiv.). Aside from the desired Me$_3$Zn$^-$, large amounts of the hydrolysis products Me$_2$Zn(OH)$^-$ and Me$_2$Zn(OH)$_2$Li$^-$ were found in the ESI mass spectrum. Continuously cooling the solution to 195 K and injecting the cooled sample solution directly into the ESI source of the mass spectrometer by pressurized-sample infusion (PSI)[151] helped to reduce the hydrolysis in solution but could not prevent it from happening (Figure 23, left).
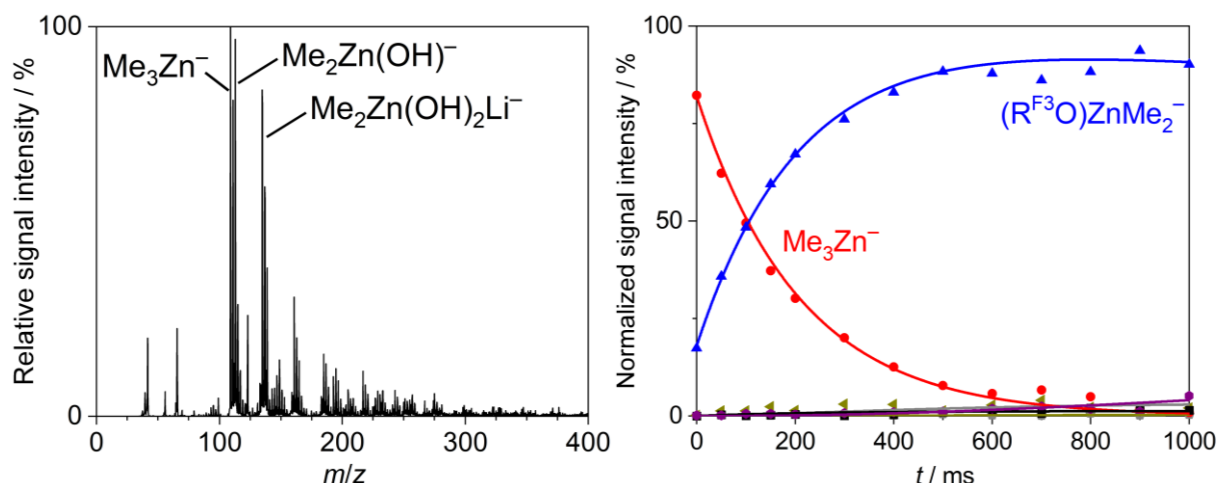
Figure 23:   Left: Negative ion-mode electrospray ionization (ESI) mass spectrum (MS^1) of a solution of the products formed in the reaction of ZnMe$_2$ with MeLi (2 equiv.) in THF (20 m$_M$) at 195 K. The peaks for Me$_3$Zn$^-$ and Me$_2$Zn(OH)$^-$ partly overlap. Right: Kinetic measurement (MS^2) of the gas-phase reaction of mass-selected (very narrow isolation width) Me$_3$Zn$^-$ with 2,2,2-trifluoroethanol (R^{F3}OH; $N_{substrate}/V$ = 5.1 × 10^9 cm^{-3}). Side reactions were observed (gray, black, purple, ocher) and accounted for in the kinetic modelling.

The reactivity of Me$_3$Zn$^-$ was probed in an ion-molecule reaction with 2,2,2-trifluoroethanol (R^{F3}OH). However, as the isotopic patterns of the species Me$_3$Zn$^-$ and Me$_2$Zn(OH)$^-$ partly overlap, a very narrow isolation width of only Δm/z = ±0.5 had to be applied to the Me$_3$Zn$^-$ isotopologue with m/z = 109 to ensure the mass selection of the correct ion. Thus mass-selected Me$_3$Zn$^-$ reacted with R^{F3}OH to give the protolysis products (R^{F3}O)ZnMe$_2^-$ and MeH which is in line with expectations. The side reaction with contaminant formic acid was observed only to a small extent. Further, a species of the type Me$_2$Zn(OMe)$^-$, which might be the product of the insertion of oxygen into the Zn–C bond was found.[135,152] The total conversion of the reactant ion Me$_3$Zn$^-$ took place within a reaction time of t = 1000 ms. This corresponds to a bimolecular rate constant of k_{exp} = (1.0±0.1) × 10^{-10} cm^3 s^{-1} and a reaction

efficiency of φ_{exp} = 69% which indicate a rather low central barrier. The second or third protonation reactions of $(R^{F3}O)ZnMe_2^-$ and $(R^{F3}O)_2ZnMe^-$, respectively, were not observed within the experimental time window (Figure 23, right; Table 3).

The energy profile for the reaction of Me_3Zn^- with $R^{F3}OH$ was obtained from quantum-chemical calculations (DLPNO-CCSD(T)/cc-pV[T;Q]Z//ωB97X-D3/def2-TZVP). When compared to the protonation of Ph_3Zn^-, the reaction is more exothermic ($\Delta\Delta_rH_0$ = 69 kJ mol^{-1}) and features a much lower central barrier of $\Delta H_0^{\ddagger}$ = −52 vs. −20 kJ mol^{-1} (Figure 24). The latter is in good agreement with the much higher reaction efficiency (φ_{exp} = 69% vs. 1.6%). Evidently, the large increase in the exothermicity comes along with the significant decrease in the activation barrier.
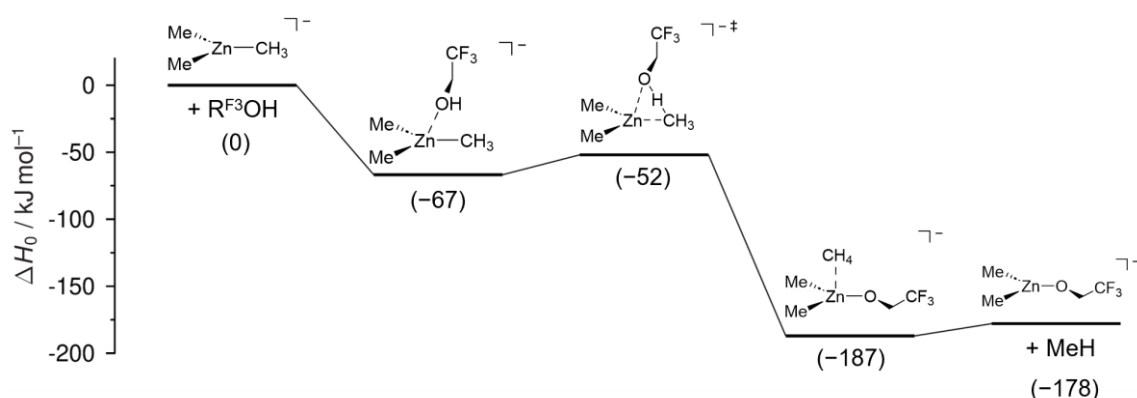
Figure 24:   Reaction pathway for the protonation of Me_3Zn^- by 2,2,2-trifluoroethanol ($R^{F3}OH$) as obtained from quantum-chemical calculations (DLPNO-CCSD(T)/cc-pV[T;Q]Z//ωB97X-D3/def2-TZVP).

The reaction pathway served as the basis for the computation of theoretical rate constants k_{theo} by Master-equation calculations. This time two different models for the kinetic simulation of the reactions were applied wherein the torsion of the methyl groups attached to the Zn center are described differently. Such methyl torsions can either be described as low-frequency *vibrations* or as free *rotations*. The choice of the model affects the sum of states in the pre-reactive complex and transition structure and the density of states in the reactant and thus, will change the microcanonical rate constant $k(E)$ according to RRKM theory. In many cases where the methyl group is not the reactive site the choice of the model is not relevant as the contributions of the methyl torsion in the reactant, pre-reactive complex and transition structure largely cancel out independent of the description as vibrations or rotations. However, in the case of methyl protonation in Me_3Zn^- by $R^{F3}OH$ the model should have a sizeable effect on the obtained phenomenological rate constant k_{theo}.

Theoretical rate constants of k_{theo} = 8.2 × 10^{-11} cm^3 s^{-1} and 3.4 × 10^{-10} cm^3 s^{-1} were obtained applying the models of low-frequency vibrations and free rotations, respectively (Table 3). The description of the methyl torsion as free rotors gives theoretical rate constants approx. 4 times faster. This model also achieves better agreement between the theoretical and experimental rate constant (k_{exp} = (1.0±0.1) × 10^{-9} cm^3 s^{-1}) within a factor of 3. Interestingly, the theoretical rate constant is again smaller than the experimental one which is similar for the trisarylzincate anions $Ar^XZnPh_2^-$ (see above). The deviating factor of 3 translates into a mismatch of the computed and "true" experimental central barrier of less than 3 kJ mol^{-1} if the empirical Boltzmann relationship is applied, which is within the limit of chemical accuracy ($\Delta E_{exp\text{-}theo}$ < ±4 kJ mol^{-1}). The results support the suitability of the quantum-chemical methods and the kinetic modelling.

Next, the trisalkylzincate anion Et_3Zn^- was studied. In an analogous fashion to Me_3Zn^-, Et_3Zn^- was prepared from a solution of Et_2Zn and $EtLi$ (2 equiv.). Similarly to Me_3Zn^-, the desired species Et_3Zn^- as well as the hydrolysis products $Et_2Zn(OH)^-$ and $Et_2Zn(OH)_2Li^-$ were observed in the ESI source mass spectrum (Figure 25, left).[9]

The trisethylzincate species was mass-selected and subjected to an ion-molecule reaction with $R^{F3}OH$. The ethyl protonation yielded the products $(R^{F3}O)ZnEt_2^-$ and EtH which is in agreement with the protolysis of Me_3Zn^-. The bimolecular rate constant k_{exp} and reaction efficiency φ_{exp} were determined to be $(8.9\pm0.2) \times 10^{-10}$ cm^3 s^{-1} and 66% which is only slightly less than for Me_3Zn^- and suggests an equally low barrier for the protonation. The side reactions with $HCOOH$ or O_2 were not observed (Figure 25, right; Table 3).
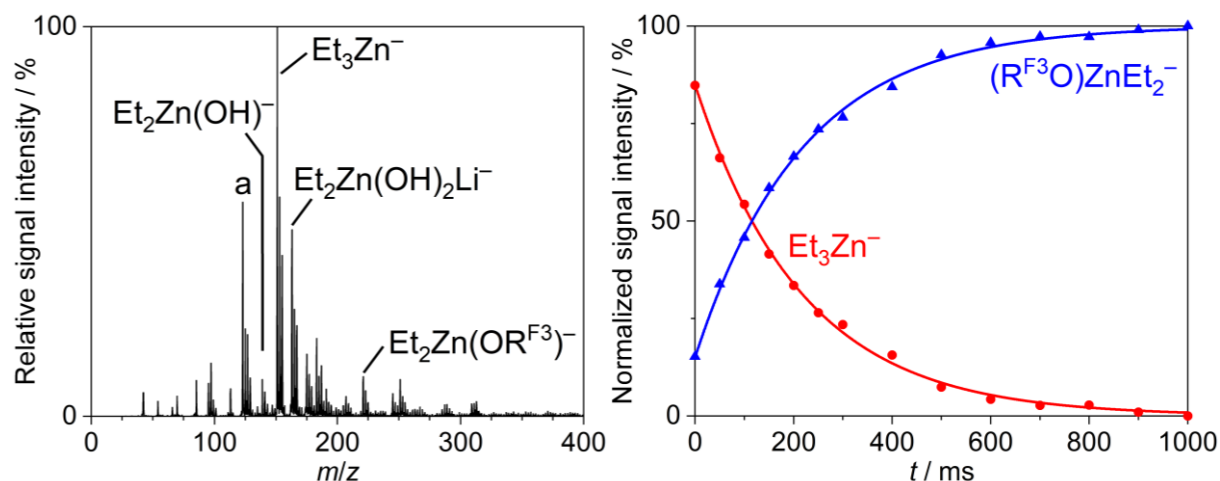
Figure 25: Left: Negative ion-mode electrospray ionization (ESI) mass spectrum (MS^1) of a solution of the products formed in the reaction of $ZnEt_2$ with $EtLi$ (2 equiv.) in THF (20 mM) at 195 K. a: unknown species. Right: Kinetic measurement (MS^2) of the gas-phase reaction of mass-selected Et_3Zn^- with 2,2,2-trifluoroethanol ($R^{F3}OH$; $N_{substrate}/V = 5.1 \times 10^9$ cm^{-3}) giving $(R^{F3}O)ZnEt_2^-$. Adapted from reference [153].

Quantum-chemical calculations (DLPNO-CCSD(T)/cc-pV[T;Q]Z//ωB97X-D3/def2-TZVP) for the protolysis of Et_3Zn^- by $R^{F3}OH$ found an energy profile which is very similar to that of Me_3Zn^-. The reaction energies $\Delta_r H_0$ differ only by 2 kJ mol^{-1}. The value for the central barrier $\Delta H_0^{\ddagger}$ amounts to -52 kJ mol^{-1} in both systems (Figure 26). That agrees well with the almost equal experimental reaction efficiencies for the methyl and ethyl protonation.

---

[9] Parts of the results presented in the following paragraphs were published in ref. [153].
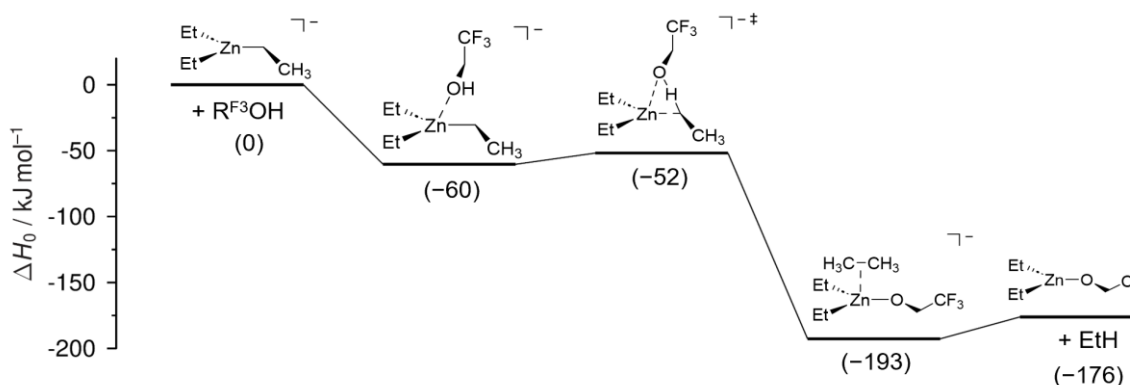
Figure 26: Reaction pathway for the protonation of Et_3Zn^- by 2,2,2-trifluoroethanol ($R^{F3}OH$) as obtained from quantum-chemical calculations (DLPNO-CCSD(T)/cc-pV[T;Q]Z//ωB97X-D3/def2-TZVP). According to reference [153].

Again, the kinetics of the reaction were simulated by carrying out Master-equation calculations based on the computed structures and energies. A theoretical rate constant $k_{theo} = 3.7 \times 10^{-10}$ cm^3 s^{-1} was obtained for $T = 310$ K. The value is less than three times lower than the experimental value $k_{exp} = 8.9 \times 10^{-10}$ cm^3 s^{-1} which is an excellent agreement between experiment and theory. Adjusting the temperature in the kinetic simulation by ±20 K (in accordance with the temperature uncertainty in the experiment) changed the rate constant by approx. ±40% which corresponds to the temperature sensitivity of the collision rate (Table 3). Furthermore, raising (lowering) the central barrier by 4 kJ mol^{-1} resulted in an decrease (increase) of the reaction rate constant by a factor of less than 2. Both results point to the fact that the reaction dynamics are governed by the formation of the pre-reactive complex and not the proton-transfer step.

Table 3: Experimental and theoretical rate constants k_{exp} and k_{theo} for the protonation the trisalkylzincate anions R_3Zn^- (R = Me, Et) by 2,2,2-trifluoroethanol ($R^{F3}OH$). The theoretical rate constants were obtained from Master equation calculations based on DLPNO-CCSD(T)/cc-pV[T;Q]Z/ωB97X-D3/def2-TZVP reaction pathways and correspond the assumed reaction temperatures of 310, 330 and 290 K, respectively.

Species	Site	k_{exp}[a] / 10^{-10} cm^3 s^{-1}	φ_{exp}[b] / %	k_{theo}[c] / 10^{-10} cm^3 s^{-1}	k^{min}_{theo}[c] / 10^{-10} cm^3 s^{-1}	k^{max}_{theo}[c] / 10^{-10} cm^3 s^{-1}
Me$_3$Zn$^-$	Me	10.0 ± 1.0	69	0.8	0.5	1.3
				3.4[d]	2.5[d]	4.6[d]
Et$_3$Zn$^-$	Et	8.9 ± 0.2	66	3.7	2.7	5.1

[a] The experimental uncertainty corresponds to the statistical error from two independent measurements (95% confidence interval). [b] The reaction efficiency φ was calculated by dividing the experimental rate constant by the collision rate according to the capture theory by Su and Chesnavich. [c] In the theoretical modelling of the reaction kinetics, the symmetry number was taken into account. [d] The methyl torsions were treated as free rotors.

To learn more about the intrinsic reactivity of organozincate anions featuring stabilized carbanions as residues that can be described as Eigen abnormal bases, the findings for the three homoleptic organozincate anions R_3Zn^- (R = Me, Et, Ph) were combined and tested for linear free (energy) relationships. The reaction enthalpies Δ_rH_0 and the central barriers $\Delta H_0^{\ddagger}$ as obtained from quantum-chemical calculations (DLPNO-CCSD(T)/cc-pV[T;Q]Z//ωB97X-D3/def2-TZVP) were correlated (Brønsted-type relationship). A dependence between the thermochemistry and kinetics was found as the increasing (decreasing) exothermicity lowers (raises) the central barrier of the proton-transfer reaction. If one fitted the data with a linear regression, a Brønsted parameter of $\alpha \approx 0.5$ would be obtained (Figure 27).

Due to the scarcity of data points it is difficult to make more extensive statements. However, it is likely that the investigations of more organic residues, such as further alkyl (sp^3), alkenyl (sp^2) or alkynyl (sp) moieties, will support the presumably linear dependence between the gas-phase basicity of R$^-$ and the protonation rate in the organozincates R$_3$Zn$^-$. At this point, it is unclear whether the hybridization (sp^2 vs. sp^3) affects the central barrier only via the change in the reaction energy or whether the hybridization modifies the intrinsic barrier in other ways, too. It could turn out that the character of the C bases become more Eigen normal from C(sp^3) over C(sp^2) to C(sp) which might result from the availability of π electrons at the C site.
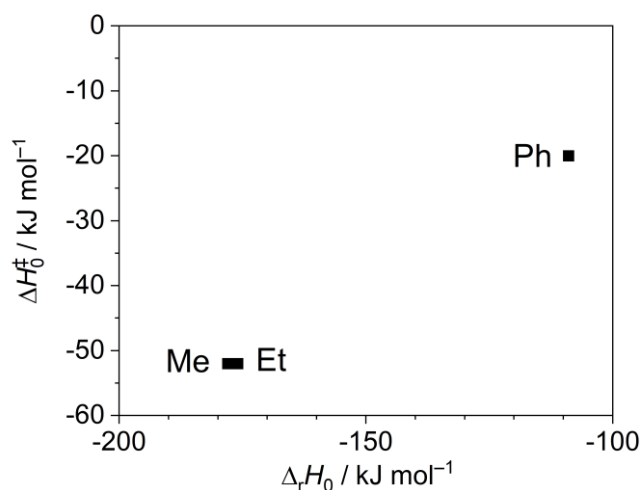
Figure 27: Brønsted-type correlation of the calculated central barrier $\Delta H_0^{\ddagger}$ with the calculated reaction enthalpy $\Delta_r H_0$ for the protonation reactions of the homoleptic organozincate anions R$_3$Zn$^-$ (R = Me, Et, Ph) with 2,2,2-trifluoroethanol (R^{F3}OH).

In the endeavor to shed light onto that question, the mixed organozincates with both aryl and alkyl moieties were studied. The approach allowed for the direct comparison of the aryl vs. alkyl protonation by means of competitive reaction pathways. Accordingly, the proton-transfer reactions of Ph$_2$ZnMe$^-$ and PhZnMe$_2^-$ with 2,2,2-trifluoroethanol (R^{F3}OH) were investigated (Scheme 9).
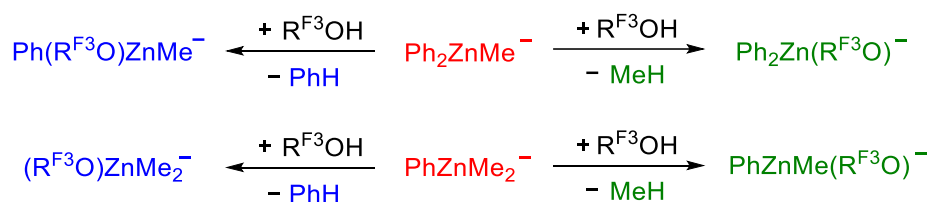
Scheme 9: Proton-transfer reactions of the heteroleptic aryl-alkyl organozincate anions Ph$_2$ZnMe$^-$ (top; red) and PhZnMe$_2^-$ (bottom; red) with 2,2,2-trifluoroethanol (R^{F3}OH). The protonation can occur either at the phenyl site (blue) or the methyl site (green).

In the negative-ion mode electrospray-ionization mass spectrum of a solution of ZnCl$_2$, PhLi (2 equiv.) and MeLi (2 equiv.), the two major species were Ph$_2$ZnMe$^-$ and Ph$_3$Zn$^-$. Only small amounts of PhZnMe$_2^-$ were observed (Figure 28, left). The results can most probably be ascribed to the higher ESI activity of such organozincate anions bearing phenyl groups over those with methyl groups because the phenyl groups enhance the surface activity of the ions in the microdroplets during the ESI process which renders their ion evaporation more efficient (cf. section 1.2.1.1). The species Ph$_2$ZnMe$^-$ was mass-selected and subjected to IMR experiments with R^{F3}OH. Aside from the reactions with residual

HCOOH in the ion trap, both the protonation of the phenyl and methyl sites were observed giving either Ph(R^{F3}O)ZnMe$^-$ and PhH or Ph$_2$Zn(R^{F3}O)$^-$ and MeH. The consecutive proton-transfer reactions were not observed. The proton transfer to the phenyl site was much more pronounced and approx. 5 times faster (k_{Ph} = (9.6±0.7)× 10^{-11} vs. k_{Me} = (2.4±0.3) × 10^{-11} cm^3 s^{-1}; φ_{Ph} = 8% vs. φ_{Me} = 2%). Even if the statistical factor of 2:1 (Ph:Me) is corrected for, the protonation of the phenyl groups is favored (Figure 28, right).
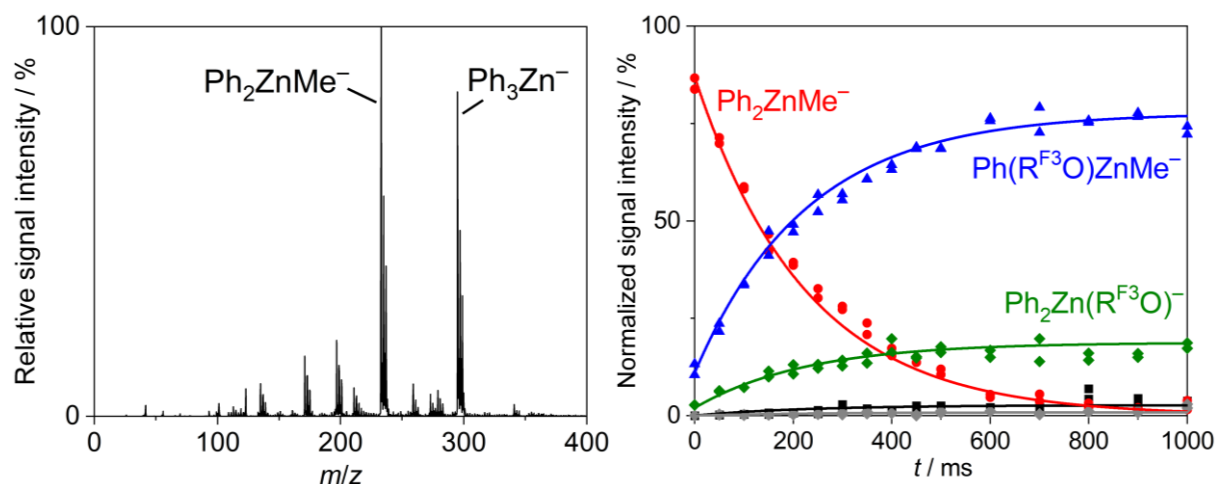
Figure 28: Left: Negative ion-mode electrospray ionization (ESI) mass spectrum (MS^1) of a solution of the products formed in the reaction of ZnCl$_2$ with PhLi (2 equiv.) and MeLi (2 equiv.) in THF (20 mм) at 273 K. Right: Kinetic measurement (MS^2) of the gas-phase reaction of mass-selected Ph$_2$ZnMe$^-$ with 2,2,2-trifluoroethanol R^{F3}OH; $N_{substrate}/V$ = 3.4 × 10^{10} cm^{-3}). Side reactions with HCOOH were observed (gray, black) and accounted for in the kinetic modelling.

The complementary organozincate species featuring two methyl groups and one phenyl group, PhZnMe$_2$$^-$, was prepared by electrospraying a solution of ZnMe$_2$ and PhLi (1 equiv.). The electrospray-ionization mass spectrum of that solution had an overall lower absolute signal intensity and showed various species. The two dominant ions were PhZnMe$_2$$^-$ and Ph$_2$ZnMe$^-$. Even though only 1 equiv. of PhLi was present in the solution, the zincate Ph$_2$ZnMe$^-$ was observed in higher intensity than PhZnMe$_2$$^-$. The finding poses an example of the scrambling of the zinc-bound aryl and alkyl residues in solution (Figure 29, left). The ion-molecule reaction of isolated PhZnMe$_2$$^-$ with the proton donor R^{F3}OH yielded the products of the phenyl protonation, (R^{F3}O)ZnMe$_2$$^-$ and PhH, and the methyl protonation, PhZnMe(R^{F3}O)$^-$ and MeH. In the kinetic measurement, both product ions were obtained in roughly the same amount. Bimolecular rate constants of k_{Ph} = 1.9 × 10^{-10} cm^3 s^{-1} and k_{Me} = 1.7 × 10^{-10} cm^3 s^{-1} as well as reaction efficiencies of φ_{Ph} = 14% and φ_{Me} = 13% were determined for the proton transfer to the phenyl and methyl sites, respectively. Apparently, the protonation of the Ph is favored over that of Me here, too (Figure 29, right).
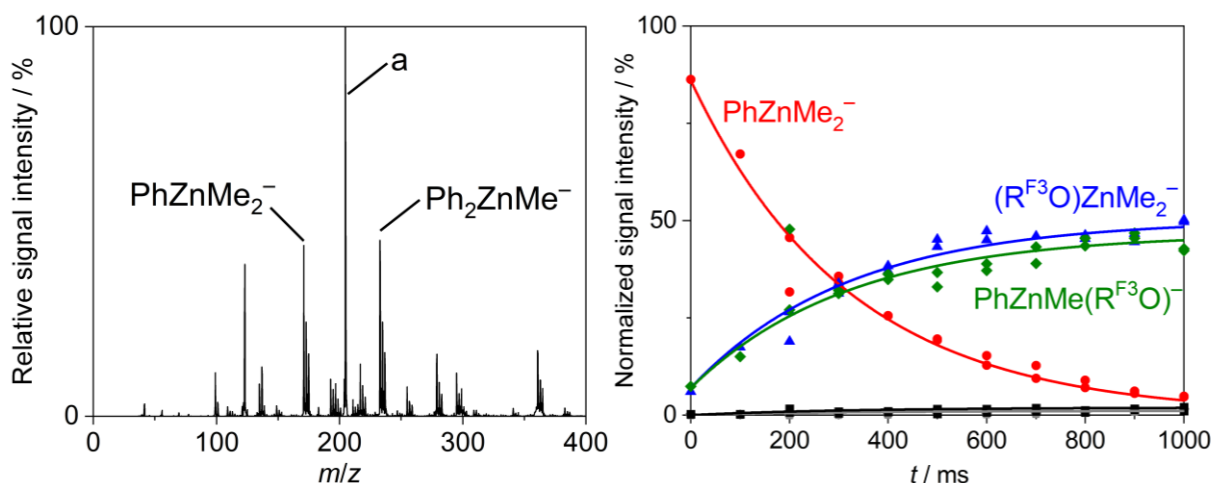
Figure 29: Left: Negative ion-mode electrospray ionization (ESI) mass spectrum (MS[1]) of a solution of the products formed in the reaction of $ZnMe_2$ with PhLi (1 equiv.) in THF (20 mM) at 273 K. a: unknown species. Right: Kinetic measurement (MS[2]) of the gas-phase reaction of mass-selected $PhZnMe_2^-$ with 2,2,2-trifluoroethanol ($R^{F3}OH$; $N_{substrate}/V = 8.5 \times 10^9$ cm^{-3}). Side reactions with HCOOH were observed (gray, black) and accounted for in the kinetic modelling.

For more detailed insight into the reactions of Ph_2ZnMe^- and $PhZnMe_2^-$ with 2,2,2-trifluoroethanol ($R^{F3}OH$), quantum-chemical calculations were conducted. The structures of the involved reactants, intermediates, products and transition structures were optimized using the DFT functional ωB97X-D3 and def2-TZVP basis sets. Additionally, electronic single-point energy calculations with the local coupled-cluster method DLPNO-CCSD(T) and cc-pVnZ basis sets extrapolated to the complete basis set (CBS) limit (n = T;Q) were carried out. Double-well potentials in terms of the enthalpy at 0 K, ΔH_0, were obtained for the reaction profiles in all cases. As for the trisarylzincate anions, an encounter complex forms first. Subsequently, the pre-reactive complex reacts to the product complex via the transition structure. Eventually, the product complex dissociates into the products. All reactions are exothermic ($\Delta_r H_0 < 0$) and feature central barriers of around −35 kJ mol^{-1} (Figure 30, Figure 31).
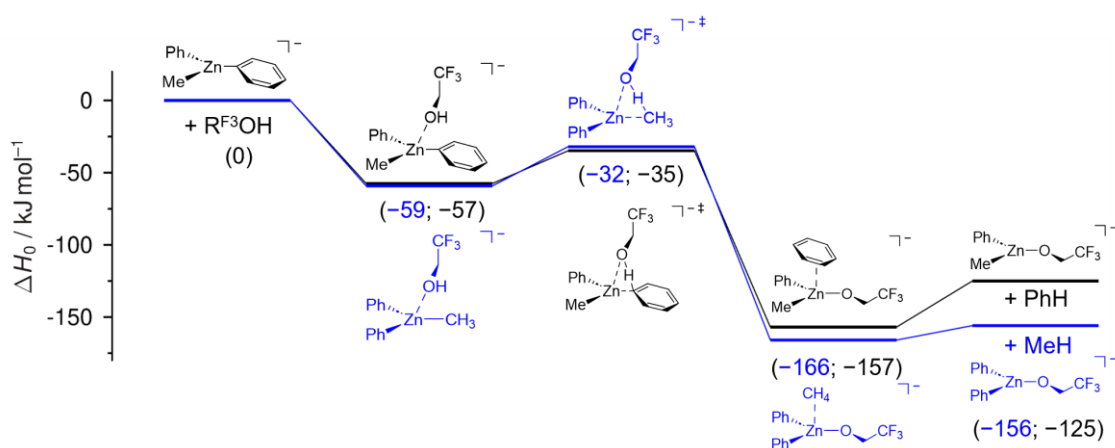

Figure 30: Reaction pathways for the protonation of the phenyl (black) and methyl (blue) moiety of Ph_2ZnMe^- by 2,2,2-trifluoroethanol ($R^{F3}OH$) as obtained from quantum-chemical calculations (DLPNO-CCSD(T)/cc-pV[T;Q]Z//ωB97X-D3/def2-TZVP).

48

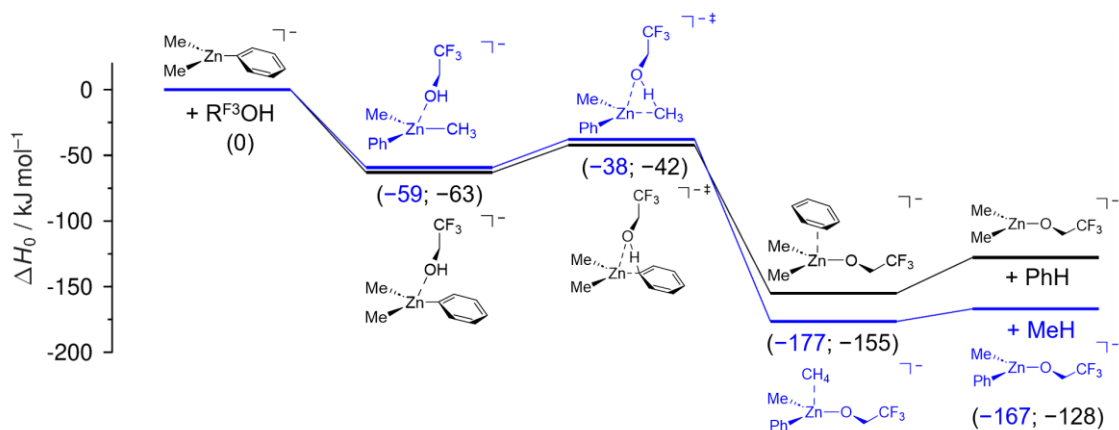Figure 31: Reaction pathways for the protonation of the phenyl (black) and methyl (blue) moiety of PhZnMe$_2^-$ by 2,2,2-trifluoroethanol (R^{F3}OH) as obtained from quantum-chemical calculations (DLPNO-CCSD(T)/cc-pV[T;Q]Z//ωB97X-D3/def2-TZVP).

In both systems the central barrier for the phenyl protonation is lower than for the methyl protonation which is in agreement with the experimental results. Another result is noteworthy: Although the protonation of the methyl moiety is more exothermic, the phenyl protonation features the lower central barrier. In accordance with the computed reaction pathways, the theoretical rate constants for the phenyl protonation in Ph$_2$ZnMe$^-$ and PhZnMe$_2^-$ were determined to be higher (5.0 × 10^{-11} and 1.4 × 10^{-11} cm^3 s^{-1}) than for the respective methyl protonations (1.6 × 10^{-11} and 6.0 × 10^{-12} cm^3 s^{-1}).

Apparently, the reaction energy and activation barrier are not connected in a straightforward fashion in the mixed aryl-alkyl zincate anions as opposed to the homoleptic zincate anions where an increase (decrease) in the exothermicity caused a proportionally lower (higher) central barrier. The results illustrate the role of the hybridization of the C bases (sp^2 vs. sp^3) for the intrinsic barriers associated with the proton-transfer reactions involving organozincate anions. However, the question of *how* the hybridization affects the intrinsic barriers cannot be answered conclusively at this point and further research is needed.

Table 4: Experimental and theoretical rate constants k_{exp} and k_{theo} for the protonation of the mixed aryl-alkyl zincate anions Ph$_2$ZnMe$^-$ and PhZnMe$_2^-$ by 2,2,2-trifluoroethanol (R^{F3}OH). The theoretical rate constants were obtained from Master equation calculations based on DLPNO-CCSD(T)/cc-pV[T;Q]Z/ωB97X-D3/def2-TZVP reaction pathways and correspond the assumed reaction temperatures of 310, 330 and 290 K, respectively.

Species	Site	k_{exp}[a,b] / 10^{-11} cm^3 s^{-1}	φ_{exp}[c] / %[b]	k_{theo}[d] / 10^{-11} cm^3 s^{-1}	k^{min}_{theo}[d] / 10^{-11} cm^3 s^{-1}	k^{max}_{theo}[d] / 10^{-11} cm^3 s^{-1}
Ph$_2$ZnMe$^-$	Ph	9.6±0.7	8	5.0	3.1	8.1
	Me	2.4±0.3	2	1.6	1.0	2.8
PhZnMe$_2^-$	Ph	19[e]	14	1.4	0.8	2.5
	Me	17[e]	13	0.6	0.3	1.1

[a] The experimental uncertainty corresponds to the statistical error from two independent measurements (95% confidence interval). [b] The experimental rate constants stem from the fit of the experimental data without consideration of the statistical factors. [c] The reaction efficiency φ_{exp} was calculated by dividing the experimental rate constant by the collision rate according to the capture theory by Su and Chesnavich. [d] In the theoretical modelling of the reaction kinetics, the symmetry number was taken into account. [e] No experimental uncertainty is given, as only one experiment was performed.

3.1.1.2   Influence of other bases

After the investigation of C bases in the form of organic residues in organozincate species, the influence of other bases X^- (X = H, O, F, Cl) on the intrinsic reactivity was studied. For the example of the organozincate anions Et_2ZnX^- the substituent effects were probed. In such organozincate anions, either one of the ethyl moieties or the X group is protonated (Scheme 10).
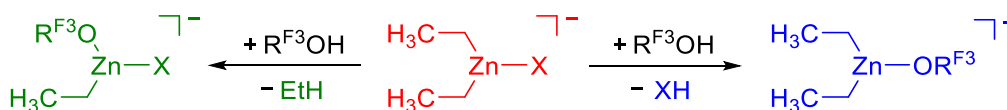
Scheme 10:   Protolysis reactions of Et_2ZnX^- (X = H, O, F, Cl) by 2,2,2-trifluoroethanol ($R^{F3}OH$). The protonation can occur either at the X site (blue) or the Et site (green).

First, the substituent effects for X = H were studied. A solution of $ZnEt_2$ and ^nBuLi in THF at 195 K was prepared which showed the homoleptic species Et_3Zn^- and Bu_3Zn^-, the heteroleptic species Et_2ZnBu^- and $EtZnBu_2^-$ as well as some hydrolysis products in the ESI mass spectrum (Figure 32, left). The ion Et_2ZnBu^- was mass-selected and subjected to collision-induced dissociation (CID). Therein, Et_2ZnH^- formed via β-hydride elimination. The anion reacted with 2,2,2-trifluoroethanol ($R^{F3}OH$). In the kinetic measurement, the protonation was observed at the hydride as well as the ethyl site. The proton transfer to the hydride residue proceeded with a rate constants of $k_{exp} = (9.6\pm0.2) \times 10^{-10}$ cm^3 s^{-1} and a reaction efficiency of $\varphi_{exp} = 68\%$. In contrast, the ethyl protonation was much slower with $k_{exp} = (1.7\pm0.5)\ 10^{-10}$ cm^3 s^{-1} and $\varphi_{exp} = 12\%$ which indicates that the ethyl protonation is associated with the higher reaction barrier (Figure 32, right).
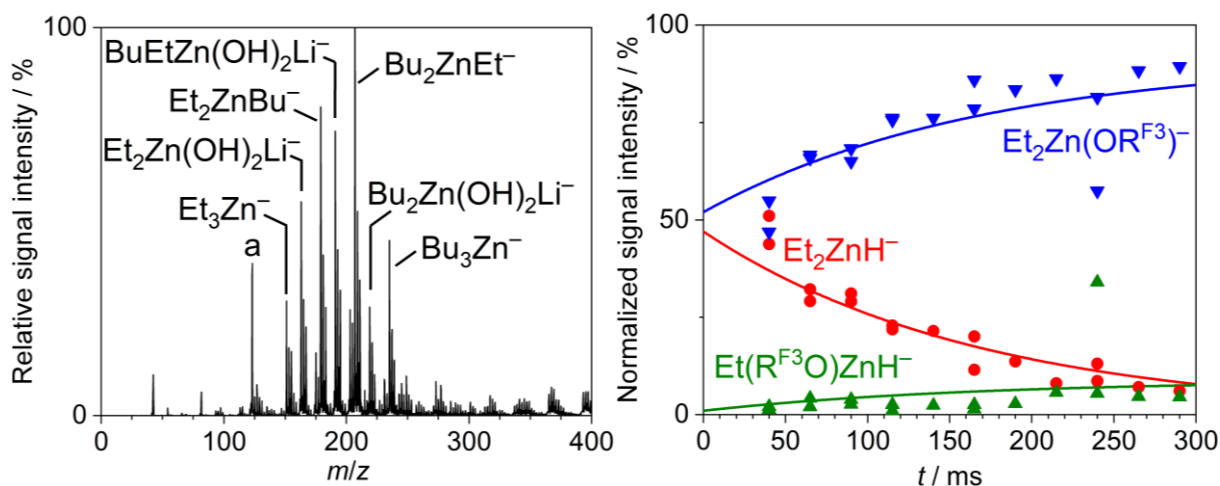

Figure 32:   Left: Negative ion-mode electrospray ionization (ESI) mass spectrum (MS^1) of a solution of the products formed in the reaction of $ZnEt_2$ with ^nBuLi (1 equiv.) in THF (20 mM) at 273 K. a: unknown species. Right: Kinetic measurement (MS^2) of the gas-phase reaction of mass-selected Et_2ZnH^- with 2,2,2-trifluoroethanol ($R^{F3}OH$; $N_{substrate}/V = 5.1 \times 10^9$ cm^{-3}).

To analyze the intrinsic reactivity of Et_2ZnH^- in more detail, quantum-chemical calculations were performed. For the H and Et protonation, the reaction pathways were found to be double-well potentials in terms of the enthalpy at 0 K, ΔH_0. Although the protonation of the ethyl groups is more exothermic, the proton transfer to the hydride features the lower central barrier (Figure 33). Based on the calculated structures and energies, Master-equation calculations were conducted to simulate the experiment *in silico*. Theoretical rate constants k_{theo} of 9.6×10^{-10} and 5.7×10^{-10} cm^3 s^{-1} were obtained for the H and Et

protonation, respectively. Accordingly, the kinetic modelling reproduces the experimental findings qualitatively, even though the branching ratio between both reaction channels does not agree quantitatively.
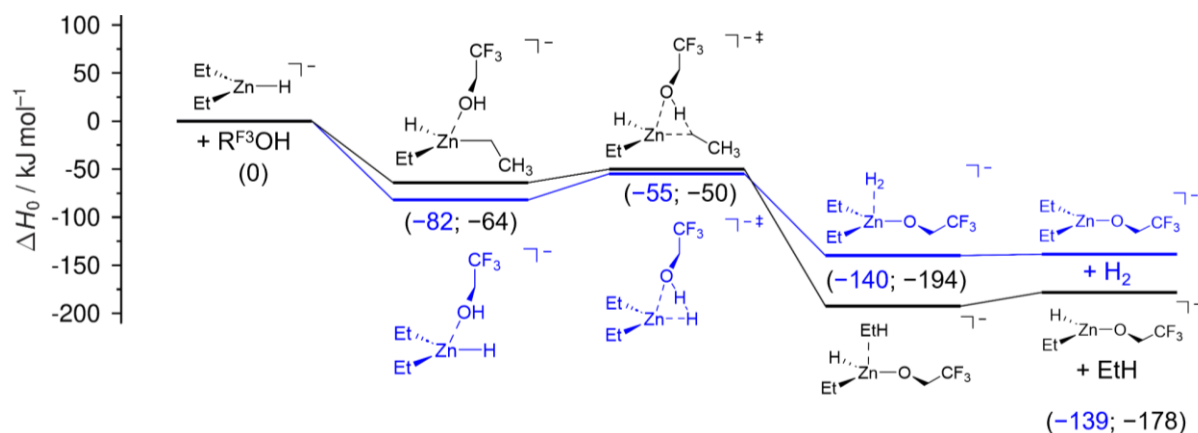

Figure 33: Reaction pathways for the protonation of the ethyl (black) and hydride (blue) group of Et_2ZnH^- by 2,2,2-trifluoroethanol ($R^{F3}OH$) as obtained from quantum-chemical calculations (DLPNO-CCSD(T)/cc-pV[T;Q]Z//ωB97X-D3/def2-TZVP).

Second, the intrinsic reactivity of organozincates with hydroxy groups (X = OH) was investigated.[10] Upon stirring for 15 min and warming from 195 to 298 K, a solution of $ZnEt_2$ and EtLi (1 equiv.) gave the hydrolysis products $Et_2Zn(OH)^-$ and $Et_2Zn(OH)_2Li^-$ (Figure 34, left). When isolated $Et_2Zn(OH)^-$ reacted with $R^{F3}OH$ in an ion-molecule reaction, only the protonation of the OH group was observed. This result is surprising given that the Et^- anion is much more basic than OH^- with gas-phase acidities ΔH_{acid} for EtH and H_2O of 1758 and 1633 kJ mol^{-1}, respectively.[47,154] The kinetic experiments gave a bimolecular rate constant of $k_{exp} = (1.8\pm0.2) \times 10^{-9}$ cm^3 s^{-1} (Figure 34, right).
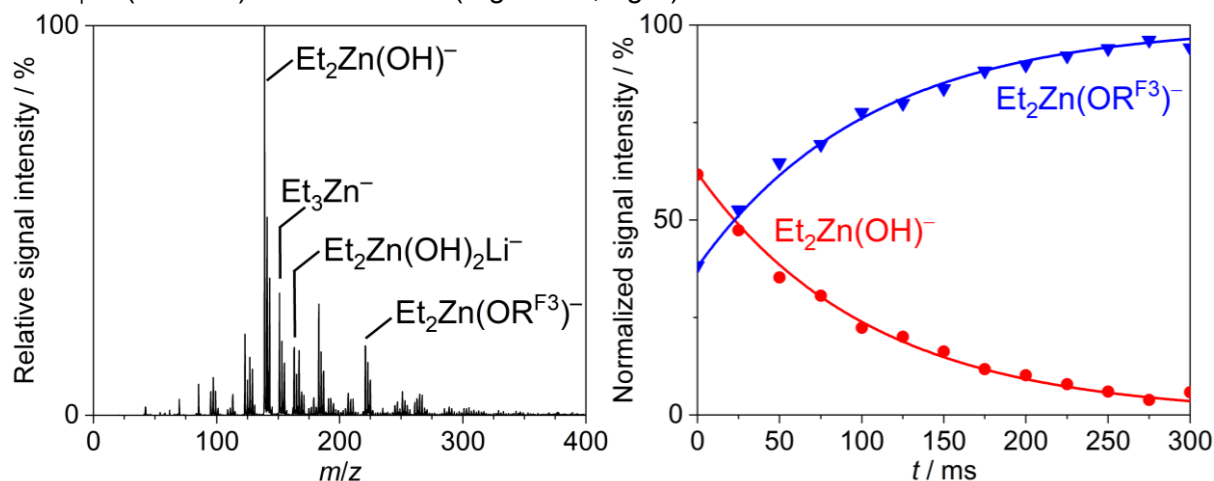

Figure 34: Left: Negative ion-mode electrospray ionization (ESI) mass spectrum (MS^1) of a solution of the products formed in the reaction of $ZnEt_2$ with EtLi (1 equiv.) in THF (20 mM) after stirring for 15 min at warming up from 195 to 298 K. Right: Kinetic measurement (MS^2) of the gas-phase reaction of mass-selected $Et_2Zn(OH)^-$ with 2,2,2-trifluoroethanol ($R^{F3}OH$; $N_{substrate}/V = 5.1 \times 10^9$ cm^{-3}). According to reference [153].

The reaction proceeded with unity efficiency. In fact, the reaction efficiency was >100% (φ_{exp} = 128%) which reflects on the shortcoming of the capture theory by Su and

---

[10] The results of the following paragraphs have already been published in reference [153].

Chesnavich.[122–124] Because the ions are treated as point charges, the spatial extent of $Et_2Zn(OH)^-$ is not accounted for and thus, the collision rates are underestimated.[126]

The energy profiles for the two conceivable protolysis reactions of $Et_2Zn(OH)^-$ by 2,2,2-trifluoroethanol ($R^{F3}OH$) were calculated quantum-chemically. The reaction pathways do predict a higher exothermicity and the higher central barrier for the ethyl protonation which is in line with the experimental observations. In fact, the energy difference between the central barriers is so high ($\Delta\Delta H_0^‡ = -59$ kJ mol^{-1}), that the proton transfer to the ethyl moieties should not occur with any significant reaction rate. Apparently, the reaction enters the OH protonation channel at an early stage as its pre-reactive complex is much more stable than for the Et protonation ($\Delta\Delta H_0 = -56$ kJ mol^{-1}) due to the hydrogen-bonding interactions between free electron pairs of the hydroxy residue of $Et_2Zn(OH)^-$ and the proton of the donor $R^{F3}OH$. This extra stabilization is mostly conserved in the transition structure (Figure 35).
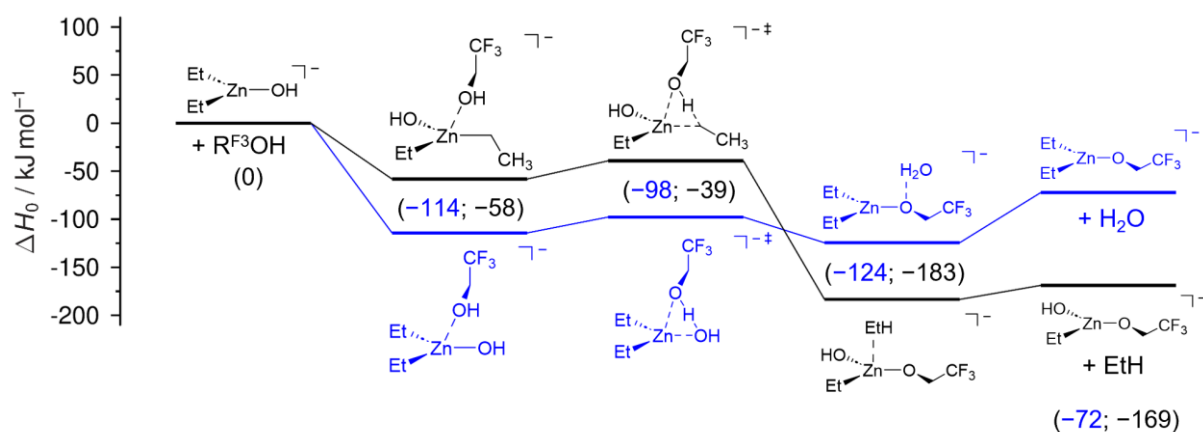

Figure 35: Reaction pathways for the protonation of the ethyl (black) and hydroxy (blue) group of $Et_2Zn(OH)^-$ by 2,2,2-trifluoroethanol ($R^{F3}OH$) as obtained from quantum-chemical calculations (DLPNO-CCSD(T)/cc-pV[T;Q]Z//ωB97X-D3/def2-TZVP). According to reference [153].

The kinetics of the reactions were simulated by carrying out Master-equation calculations. For the hydroxy and ethyl protonation, theoretical rate constants of $k_{theo} = 1.3 \times 10^{-9}$ and 1.7×10^{-10} cm^3 s^{-1} were obtained, respectively. As such, the Et protonation is predicted to be 8 times slower than the OH protonation. However, in the experiment no significant protonation at the ethyl site was observed and thus, the ethyl protonation is probably even slower.

Moreover, the intrinsic reactivity of the Li^+-containing species $Et_2Zn(OH)_2Li^-$ was probed. Lithium cations are known to enhance the reactivity of organometallic compounds in so-called "turbo" reagents.[155] In the ion-molecule reaction with $R^{F3}OH$, $Et_2Zn(OH)_2Li^-$ was protonated at both OH sites first. Only after that, one of the two ethyl residues was attacked by the proton donor. The observed reactivity is in qualitative agreement with the experimental findings for $Et_2Zn(OH)^-$ where OH was the favored protonation site, too. The kinetic analysis yielded experimental rate constants of $k_{exp} = (1.7\pm0.1) \times 10^{-9}$, $(1.1\pm0.1) \times 10^{-9}$ and $(1.3\pm0.4) \times 10^{-10}$ cm^3 s^{-1} as well as reaction efficiencies of $\varphi_{exp} = 124\%$, 79% and 10% for the two hydroxy and the ethyl protonation, respectively (Figure 36).

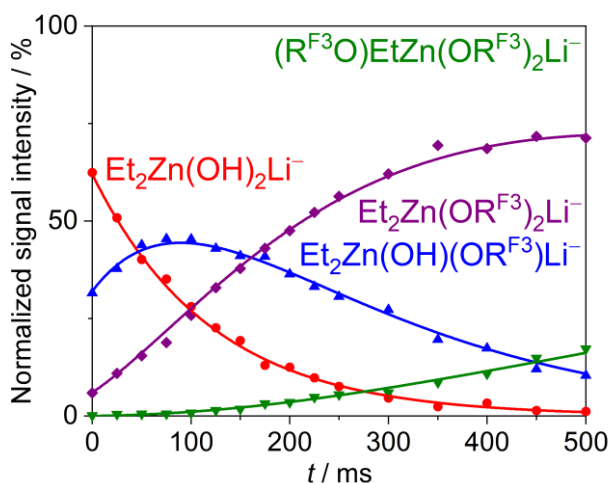Figure 36: Kinetic measurement (MS^2) of the gas-phase reaction of mass-selected Et$_2$Zn(OH)$_2$Li$^-$ with 2,2,2-trifluoroethanol (R^{F3}OH; $N_{substrate}/V$ = 5.1 × 10^9 cm^{-3}). According to reference [153].

The structure of Et$_2$Zn(OH)$_2$Li$^-$ was computed employing the DFT method ωB97X-D3/def2-TZVP. It was found to be an adduct of Et$_2$Zn(OH)$^-$ and LiOH in a planar and linear configuration. The tetragonal conformer of Et$_2$Zn(OH)$_2$Li$^-$ where two ethyl and two hydroxy groups are arranged tetrahedrally at the zinc center was computed to be 21 kJ mol^{-1} higher in energy (Scheme 11).
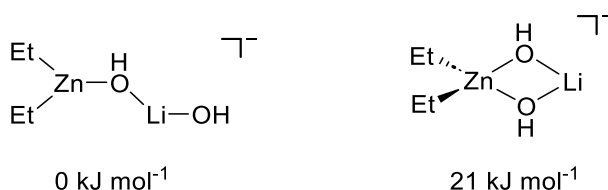
Scheme 11: Two possible structures of Et$_2$Zn(OH)$_2$Li$^-$. The tetragonal conformer (right) was computed to be higher in energy.

For the lower-energy conformer the protolysis reactions at the four conceivable sites (two Et, two OH) were calculated. The two ethyl protonation channels are similar to the Et protonation in Et$_2$Zn(OH)$^-$. However, the central barriers are increased by 9 and 18 kJ mol^{-1}, respectively, due to the higher Lewis acidity of the Zn center. Both ethyl protonations are highly exothermic. The protolysis reactions at the OH sites are much less exothermic, but feature the lower barriers for the proton transfer. The pathway for the protonation of the terminal hydroxy group is similar to that in Et$_2$Zn(OH)$^-$ with a reaction enthalpy of $\Delta_r H_0$ = −74 kJ mol^{-1} and a central barrier of $\Delta H_0^{\ddagger}$ = −105 kJ mol^{-1}. In marked contrast, the reaction pathway for the protonation of the bridging OH group distinctly differs. In the first stage of the reaction, the proton is transferred from R^{F3}OH to the internal OH moiety. However, the species undergoes a subsequent conformational change wherein the newly formed H$_2$O and the R^{F3}O$^-$ alkoxide switch positions. Only after that, water is released from the product complex and the organozincate anion Et$_2$Zn(OR^{F3})(OH)Li$^-$ forms (Figure 37).

Master-equation calculations predict theoretical rate constants of k_{theo} = 2.5 × 10^{-15} and 1.2 × 10^{-13} cm^3 s^{-1} for the proton-transfer reactions to the ethyl residues and k_{theo} = 2.4 × 10^{-10} and 9.8 × 10^{-10} cm^3 s^{-1} for the protonation of the bridging and terminal OH, respectively. The rate constants for the first protonation of Et$_2$Zn(OH)$_2$Li$^-$ at the four conceivable sites were used to determine which moiety was initially protonated in the

53

experiment. Given that the theoretical rate constant for the protonation at the terminal OH is the fastest, this site was most probably attacked at first in the experiment.
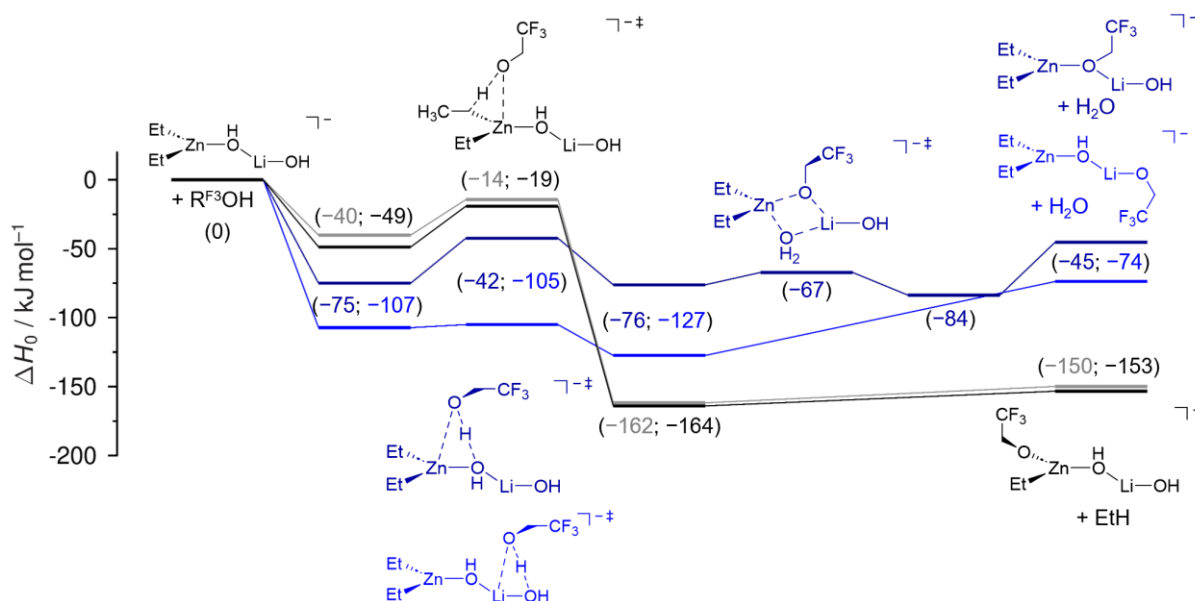

Figure 37: Reaction pathways for the protonation of the ethyl (gray, black) and hydroxy (dark blue, blue) groups of $Et_2Zn(OH)_2Li^-$ by 2,2,2-trifluoroethanol ($R^{F3}OH$) as obtained from quantum-chemical calculations (DLPNO-CCSD(T)/cc-pV[T;Q]Z//ωB97X-D3/def2-TZVP). Only the reactants, transition structures and products are given for the sake of clarity.

Third, the effect of X = F for the intrinsic reactivity of Et_2ZnX^- towards protonation was studied. The respective zincate species Et_2ZnF^- was prepared by treating a solution of $ZnEt_2$ with NBu_4F (1 equiv.) at 195 K (Figure 38, left). The ion of interest was mass-selected and allowed to react with 2,2,2-trifluoroethanol in the gas phase. Three resulting ions were observed: the product of the Et protonation, $Et(R^{F3}O)ZnF^-$, the product of the F protonation, $Et_2Zn(OR^{F3})^-$, as well as a species with the sum formula corresponding to either $Et_2ZnF(HOR^{F3})^-$ or $Et_2Zn(OR^{F3})HF^-$ whose constitution was not clear. For those three reaction channels experimental rate constants of $k_{exp} = (7.4\pm2.0) \times 10^{-11}$, $(1.9\pm0.8) \times 10^{-10}$ and $(6.3\pm2.8) \times 10^{-11}$ cm^3 s^{-1} were determined which correspond to reaction efficiencies of $\varphi_{exp} = 5\%$, 14% and 5%, respectively (Figure 38, right).
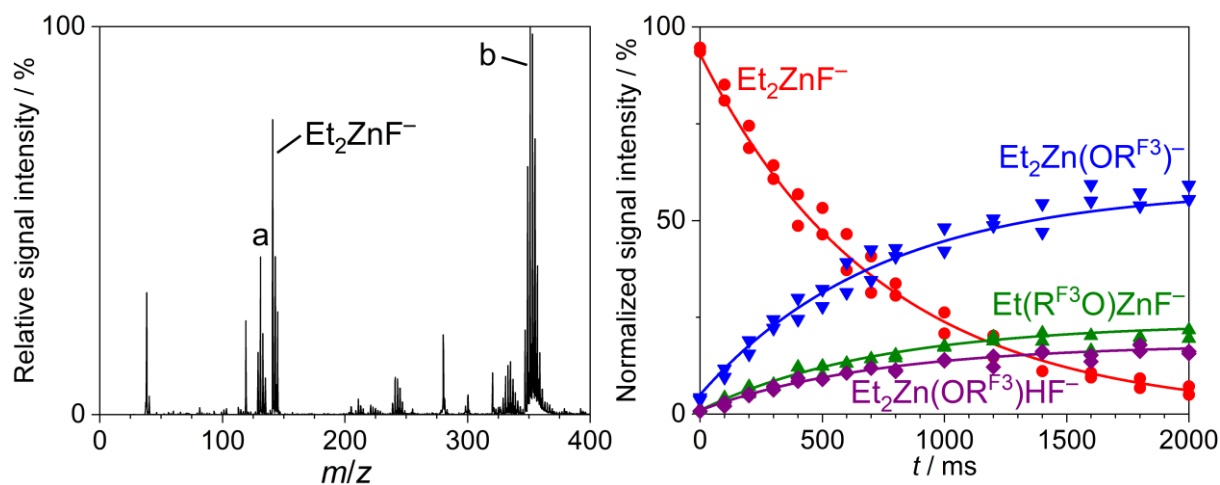

Figure 38: Left: Negative ion-mode electrospray ionization (ESI) mass spectrum (MS^1) of a solution of the products formed in the reaction of $ZnEt_2$ with NBu_4F (1 equiv.) in THF (20 mM) at 195 K. a, b: unknown species. Right: Kinetic measurement (MS^2) of the gas-phase reaction of mass-selected Et_2ZnF^- with 2,2,2-trifluoroethanol ($R^{F3}OH$; $N_{substrate}/V = 5.1 \times 10^9$ cm^{-3}).

Again, quantum-chemical calculations were conducted to characterize the reaction pathways for the protonation of Et_2ZnF^- at the Et and F site. As expected, the protonation of the ethyl moiety is exothermic ($\Delta_rH_0 = -160$ kJ mol^{-1}) and its activation barrier is rather high with $\Delta H_0^{\ddagger} = -30$ kJ mol^{-1}. Just the opposite holds true for the F protonation. Although the proton transfer is approx. thermoneutral ($\Delta_rH_0 = -11$ kJ mol^{-1}), it is associated with the lower barrier ($\Delta H_0^{\ddagger} = -77$ kJ mol^{-1}). As for $Et_2Zn(OH)^-$, the pre-reactive complex and possibly also the transition structure is energetically stabilized by hydrogen-bonding interactions between the proton of the donor $R^{F3}OH$ and the fluoride residue of the organozincate anion (Figure 39).

On the basis of the computed energy profiles, the ambiguous species with the sum formula for either $Et_2ZnF(HOR^{F3})^-$ or $Et_2Zn(OR^{F3})HF^-$, which was observed in the experiment, can be characterized. Given that the reaction barrier for the proton transfer to the F site is very low and the energy requirement for the dissociation step to the products is high, it is likely that the observed species corresponds to the product complex $Et_2Zn(OR^{F3})HF^-$ in which the newly formed HF binds to the alkoxide residue via a hydrogen bond. In other words: The reaction is trapped at the product-complex stage. From the ratio of the $Et_2Zn(OR^{F3})^-$ and $Et_2Zn(OR^{F3})HF^-$ in the kinetic measurement, it can be deduced that around 30% of the product complex fail to overcome the dissociation barrier (Figure 39).[11]

Master-equation calculations were performed only for the Et protonation in Et_2ZnF^- because for the F protonation the previously employed approximation that the dissociation step can be neglected for the kinetic simulation obviously no longer holds as is directly evident from the experimental findings. The theoretical rate constant for the proton transfer to the ethyl site was determined to be $k_{theo} = 2.5 \times 10^{-12}$ cm^3 s^{-1} which is significantly lower than the experimental value. Apparently, either the chosen kinetic model or the calculated central barrier is not accurate. If it is the latter, $\Delta H_0^{\ddagger}$ should be much (>4 kJ mol^{-1}) lower.
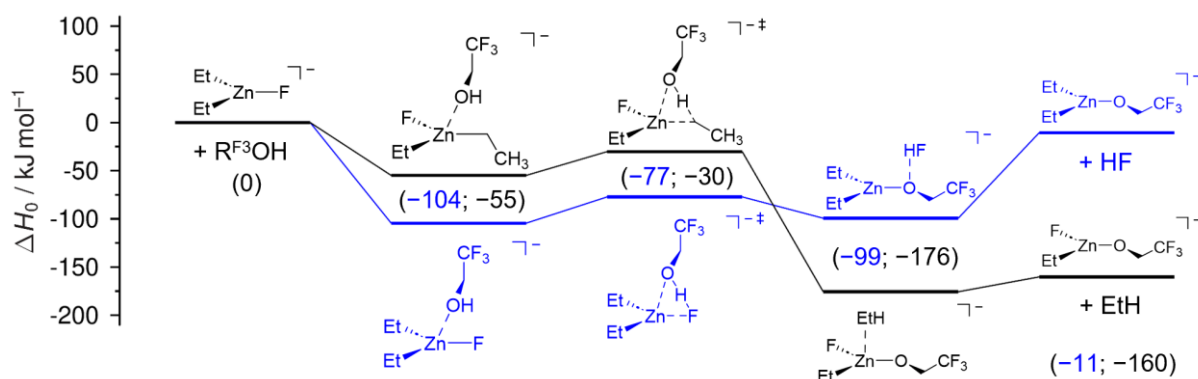

Figure 39: Reaction pathways for the protonation of the ethyl (green) and fluoride (blue) moieties of Et_2ZnF^- by 2,2,2-trifluoroethanol ($R^{F3}OH$) as obtained from quantum-chemical calculations (DLPNO-CCSD(T)/cc-pV[T;Q]Z//ωB97X-D3/def2-TZVP).

At last, the intrinsic reactivity of the organozincate anion Et_2ZnX^- (X = Cl) was investigated. In analogy to its F congener, Et_2ZnCl^- was prepared from a solution of $ZnEt_2$ and NBu_4Cl (1 equiv.) in THF at 195 K. In addition, the species $EtZnCl_2^-$ was present in small amounts (Figure 40, left). The isolated ion Et_2ZnCl^- was subjected to the reaction with $R^{F3}OH$. In contrast to Et_2ZnF^-, no halogen protonation and only the protonation of the Et residues was

<hr>

[11] The results could be combined to model the internal energy of the reacting ion over the course of the reaction. More explicitly, the collision dynamics of the mass-selected ion with the buffer gas (He) in such ion-molecule reactions could be analyzed.

observed.[12] The reaction proceeded so slowly that both a very long reaction time t of up to 6000 ms and a high substrate concentration of $N_{substrate}/V = 8.5 \times 10^{10}$ cm^{-3} were applied to monitor the reaction in the experiment. The kinetic measurement gave an experimental rate constant of only $(4.1\pm0.7) \times 10^{-12}$ cm^3 s^{-1} corresponding to a reaction efficiency φ_{exp} as low as 0.3% (Figure 40, right). It appears that the chloride moiety deactivates Et$_2$ZnCl$^-$ for the ethyl protonation in comparison to Et$_2$ZnF$^-$ by at least an order of magnitude.
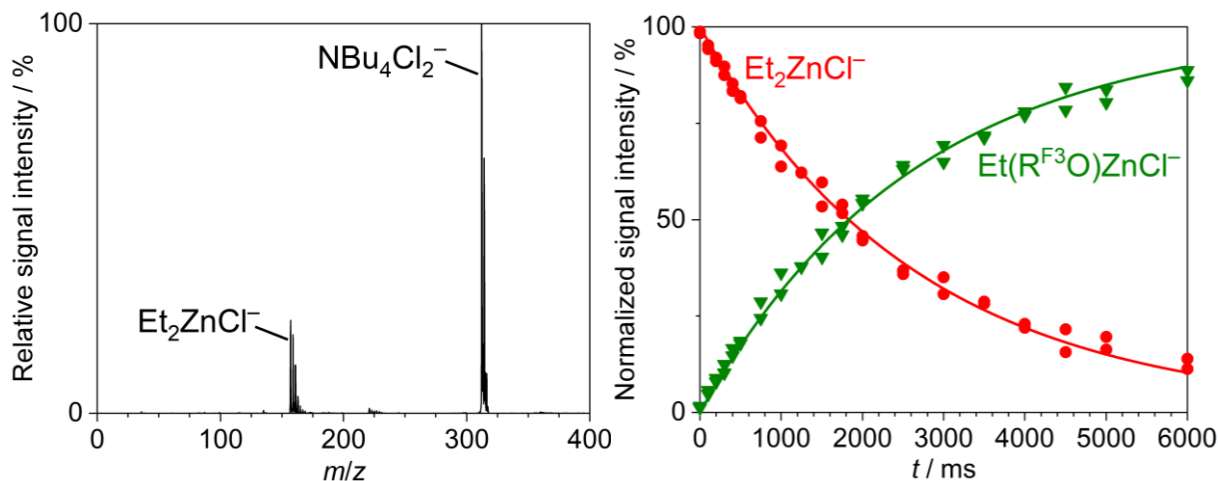

Figure 40: Left: Negative ion-mode electrospray ionization (ESI) mass spectrum (MS^1) of a solution of the products formed in the reaction of ZnEt$_2$ with NBu$_4$Cl (1 equiv.) in THF (20 mM) at 195 K. Next to the signal for Et$_2$ZnCl$^-$, some signal intensity for EtZnCl$_2^-$ was found. Right: Kinetic measurement (MS^n) of the gas-phase reaction of mass-selected Et$_2$ZnCl$^-$ with 2,2,2-trifluoroethanol (R^{F3}OH; $N_{substrate}/V = 8.5 \times 10^{10}$ cm^{-3}).
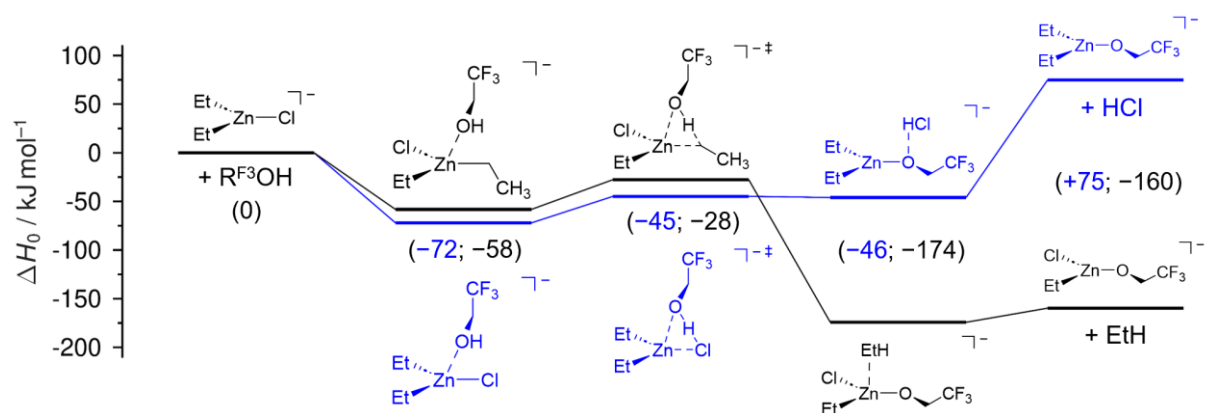

Figure 41: Reaction pathways for the protonation of the ethyl (black) and chloride (blue) moieties of Et$_2$ZnCl$^-$ by 2,2,2-trifluoroethanol (R^{F3}OH) as obtained from quantum-chemical calculations (DLPNO-CCSD(T)/cc-pV[T;Q]Z//ωB97X-D3/def2-TZVP).

Quantum-chemical calculations for the reaction pathways of the Et and Cl protonation in Et$_2$ZnCl$^-$ are in line with the experimental findings. Though the proton transfer to Cl features the lower central barrier ($\Delta H_0^\ddagger = -45$ kJ mol^{-1}), it does not take place as the reaction is endothermic ($\Delta_r H_0 = +75$ kJ mol^{-1}). The proton transfer to Et, however, is exothermic ($\Delta_r H_0 = -160$ kJ mol^{-1}) and thus, can occur despite its higher reaction barrier ($\Delta H_0^\ddagger = -28$ kJ mol^{-1}; Figure 41).[13]

---

[12] Interestingly, in the reactions of Ph$_2$ZnCl$^-$ and PhZnCl$_2^-$ with formic acid (HCOOH) the protonation of Cl was observed. In fact, it was even favored over that of the Ph residues.
[13] For Ph$_2$ZnCl$^-$ and PhZnCl$_2^-$, the Cl protonation can probably only be observed because HCOOH is much more acidic than CF$_3$CH$_2$OH and thus rendering both the Et and Cl protonation thermochemically feasible. As a consequence, the activation barriers govern the reactivity of Ph$_2$ZnCl$^-$ and PhZnCl$_2^-$ – and not the reaction energies.

In order to analyze the effects of the bases X^- as substituents in the organozincate species Et_2ZnX^- (X = H, Et, OH, F, Cl), linear energy relationships were tested to check for structure-reactivity relationships. In the Brønsted-type correlation of the calculated reaction barrier $\Delta H_0^\ddagger$ with the calculated reaction enthalpy $\Delta_r H_0$, it appears that the reaction barrier scales linearly with the reaction energy for X = OH, F and Cl, but X = H and Et deviate from that trend. The finding might be an artifact of the rather low number of data points or could hint to the different nature of Et and H as bases. Following the terminology of Eigen, one could refer to the OH, F and Cl bases as "normal" and to the ethyl and hydride anions as "non-normal" bases. The latter feature especially high intrinsic barriers. Their unusual nature leads to the breakdown of the linear relationship between thermochemical driving force and kinetic activation barrier for their protonation in Et_2ZnX^- (Figure 42). The Brønsted-type correlation clarifies that there is no easy dependence between the thermochemistry and kinetics for the X protonation in Et_2ZnX^- since the protonation sites differ too much.
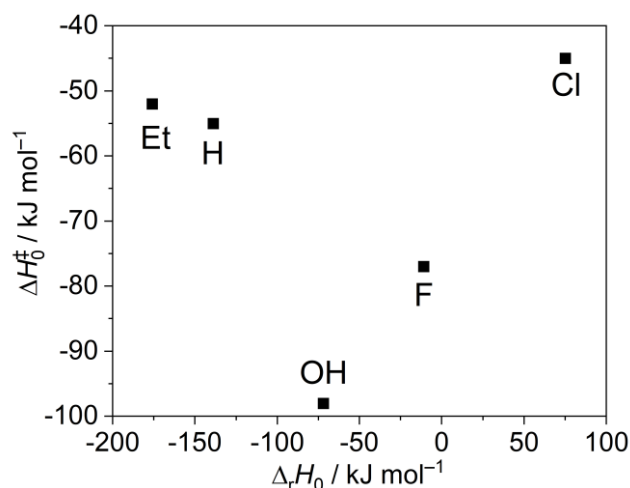

Figure 42: Brønsted-type correlation of the calculated central barrier $\Delta H_0^\ddagger$ with the calculated reaction enthalpy $\Delta_r H_0$ for the protonation reactions of the organozincate anions Et_2ZnX^- (X = H, Et OH, F, Cl) with 2,2,2-trifluoroethanol ($R^{F3}OH$) at the X site.

What causes the low intrinsic barriers for OH, F and Cl protonation on the one hand and the high intrinsic barriers for the proton transfer to H and C bases? For one, OH, F and Cl feature free electron pairs with which the proton donor $R^{F3}OH$ can form hydrogen bonds. This pre-organization stabilizes the pre-reactive complex and the transition structure thereby lowering the barrier associated with the proton transfer. This hypothesis complies with the Brønsted-type plot (Figure 42, right). It is further supported by works on identity proton-transfer reactions from Gronert in which he found linear correlations between the proton affinity of the free anions X^- (X = H, CH_3, NH_2, OH, F) and the energy of the transition structure.[62–64] In contrast, H and Et do not possess free electron pairs because the 1s orbital of the hydride and $2sp^3$ hybrid orbital of the ethyl carbon are occupied with the coordination to the Zn center. Thus, there is no extra stabilization of the TS and the central barriers for their protonation will be increased.

Another reason might stem from the electronic reorganization in X^- to form the X–H bond. For OH, F and Cl, the negative charge, which is required for the proton to bind, is already localized in (a free electron pair of) the X^- anion due to its high electronegativity. In contrast, carbanions (and possibly hydride anions) tend to delocalize the negative charge more

strongly over the entire X^- anion as a consequence of the lower electronegativity. Thus, the accepting of the proton is associated with high electronic reorganization at the carbon site. This electronic reorganization causes the exceptionally high intrinsic barriers for C protonation. The idea is backed by findings of Brauman and Savéant who found high barriers for thermoneutral proton-transfer reaction to (delocalized) C bases.[40,57]

To test these hypotheses, the transition structures for the X protonation in Et_2ZnX^- were analyzed. More specifically, the Zn–X as well as the X–H(OR^{F3}) bond lengths in the computed TS were considered for X = H, Et, OH, F and Cl. The species can be imagined in terms of the partial charges for the four-membered transition structure where Zn and the protic H of R^{F3}OH feature positive partial charges and X and the hydroxy O of R^{F3}OH negative partial charges (Scheme 12).
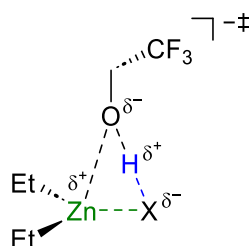
Scheme 12:   Transition structure for the protonation of Et_2ZnX^- by 2,2,2-trifluoroethanol (R^{F3}OH) at the X site. The Zn—X (green) and the X–H(OR^{F3}) (blue) bond lengths were considered.
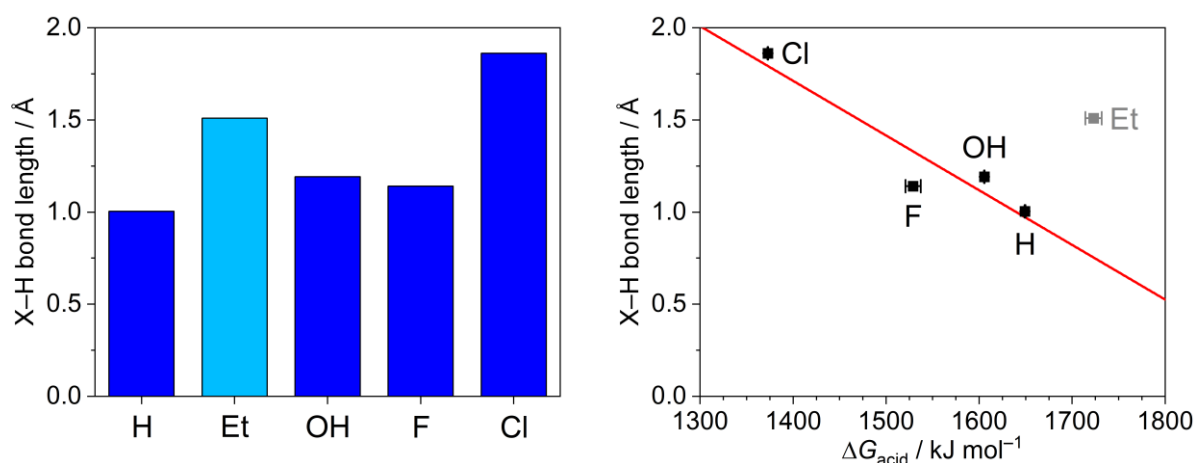

Figure 43:   Left: X–H(OR^{F3}) bond length in the transition structure for the X protonation of Et_2ZnX^- (X = H, Et, OH, F, Cl). Right: Correlation of X–H bond length with the gas-phase acidity ΔG_{acid} of XH. Disregarding X = Et (gray), the data was fitted with a linear regression ($m = -0.003$; $R^2 = 0.83$).

It was found that the X–H(OR^{F3}) bond length increases from X = H to Cl as would be expected from the gas-phase acidities of XH which is a measure of the capability of X^- to form hydrogen bonds. However, Et does not match the trend (Figure 43). This indeed supports the idea of the significance of hydrogen-bonding for the intrinsic barrier for the proton transfer as postulated by Gronert.

Moreover, the Zn−X bond distances were studied. Apparently, this bond length increases from X = H to Cl, too. The correlation with the gas-phase acidity of XH, which may be taken as a proxy for the affinity of X^- to bind Zn^{2+}, is evident. The more acidic XH is, the more stable is the free anion X^- and the less tightly X^- binds to the metal center. Again, Et deviates from the described trend with an rather high Zn–C bond length (Figure 44). This hints to the second hypothesis about C bases delocalizing the negative charge more than

Eigen-normal bases such as OH and F as Brauman and Savéant propose. However, the comparison is not entirely fair because Et is larger than OH, F, and Cl and thus, inherently tends to delocalize the negative charge more. So, the system with X = CH_3 must be investigated to conclusively assess the validity of the second hypothesis. If X = CH_3 shows similar properties as for X = Et, then the electronic reorganization hypothesis is underlined.
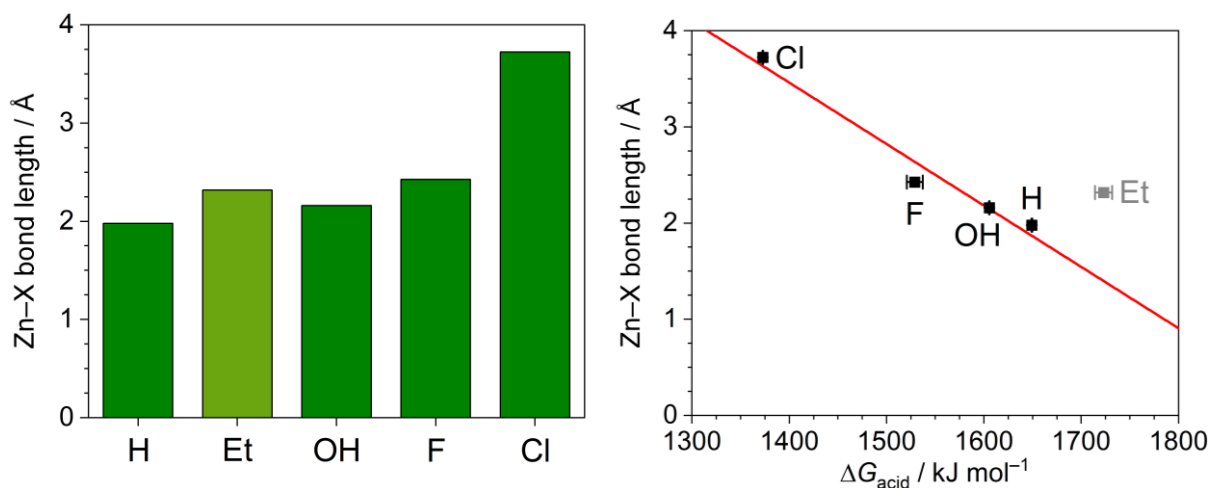

Figure 44: Left: Zn–X bond length in the transition structure for the X protonation of Et_2ZnX^- (X = H, Et, OH, F, Cl). Right: Correlation of Zn–X bond length with the gas-phase acidity ΔG_{acid} of XH. Disregarding X = Et (gray), the data was fitted with a linear regression (m = −0.006; R^2 = 0.95).

The indirect substituent effect of X onto the Et protonation in Et_2ZnX^- (X = H, Et, OH, F, Cl) was investigated. The Eigen-type correlation evidently shows a linear dependence of the logarithmic rate constant from the gas-phase acidity of XH. Furthermore, the Brønsted-type plot reveals the linear correlation of the central barrier and the reaction enthalpy (Figure 45). Both trends can be explained with the same structure-reactivity relationship: The more (less) basic the substituent X^- is, the more (less) electron density is pushed into the organozincate which, mediated via the metal center, also increases (decreases) the basicity of the Et groups facilitating (hampering) their protonation.
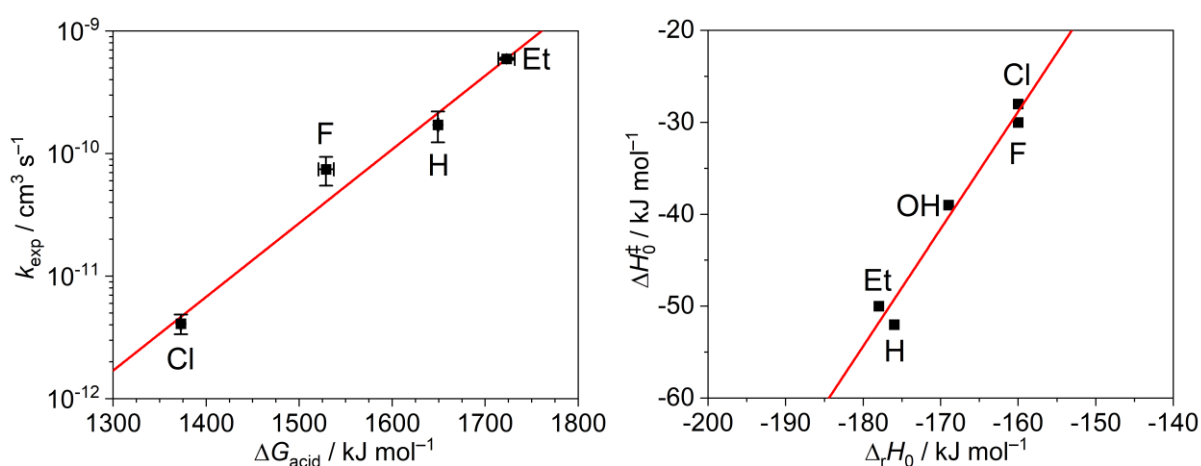
Figure 45: Left: Eigen-type correlation of the experimental rate constant k_{exp} with the experimental gas-phase acidity ΔG_{acid} of the XH (X = H, Et, F, Cl) for the protonation at the Et site of Et_2ZnX^- with $R^{F3}OH$ and linear regression (red line; m = 0.006, R^2 = 0.99). The values for the gas-phase acidities were taken from ref. [47]. Right: Brønsted-type correlation of the calculated central barrier $\Delta H_0^{\ddagger}$ with the calculated reaction enthalpy $\Delta_r H_0$ for the protonation reactions of the organozincate anions Et_2ZnX^- (X = H, Et, OH, F, Cl) with 2,2,2-trifluoroethanol ($R^{F3}OH$) at the Et site and linear regression (red line; m = 1.3, R^2 = 0.96).

The findings about the direct and indirect effect of the substituent X (X = H, OH, F, Cl) in the protonation of the organozincate species Et_2ZnX^- help to understand how organometallic transformations are possible within protic media. Usually, organometallic reagents need to be handled under strict inert-gas conditions excluding any air or water which would oxidize or hydrolyze the reactive species. However, recent results show that chemical reactions with typical transmetalation reagents, such as organolithium, Grignard or zinc organyl compounds, can also be carried out in protic media which is unexpected because the protic hydrogen atoms should lead to the quenching of the organometallic reagents.[3–6,156] Often, the observed reactivity is considered to be the consequence of the transmetalation kinetically outcompeting the hydrolysis. However, the detailed reasons are not fully understood yet and no general explanation has been found so far.[3–6,156]

So-called deep eutectic solvents (DES) are one of these protic media. DES are typically prepared from quaternary ammonium salts (e.g. choline chloride) and a metal chloride or hydrogen-bond donor. It was found that organometallic reagents, such as RMgCl, are often more reactive in DES under air than in aprotic solvents under inert-gas conditions. The literature rationalized the reactivity enhancement by a "double role"[3] of the quaternary ammonium halide as a component of the DES as well as the origin of putative anionic species, such as $RMgCl_2^-$, which would facilitate the reaction as a result of the increased intermolecular interactions between the negatively charged metalate complex and the substrate (cf. Figure 2 in section 1.1.2.1).[3–6]

The findings presented in this section support the hypothesis of the formation of metalate complexes as the organozincate anions Et_2ZnX^- readily form upon the addition of NBu_4X (X = F, Cl), which is very similar to choline chloride, to a solution of $ZnEt_2$ in THF (Figure 38, Figure 40). Moreover, they suggest a *third* role of the quaternary ammonium salt. By the formation of the metalate complex, the intrinsic properties of the organometallic compound are altered twofold. First, the activation barrier for the alkyl (aryl) protonation is increased (indirect effect). Furthermore, the X substituent operates as proton scavenger which proton donors will form hydrogen bonds with (and transfer their proton to). So, single proton donor molecules will not be able to attack the more basic C site as they are caught by the X group (direct effect).

Table 5: Experimental and theoretical rate constants k_{exp} and k_{theo} for the protonation of the zincate anions Et$_2$ZnX$^-$ (X = H, OH, F, Cl) by 2,2,2-trifluoroethanol (R^{F3}OH). The theoretical rate constants were obtained from Master equation calculations based on DLPNO-CCSD(T)/cc-pV[T;Q]Z/ωB97X-D3/def2-TZVP reaction pathways and correspond the assumed reaction temperatures of 310, 330 and 290 K, respectively.

Species	Site	k_{exp}[a,b] / 10^{-10} cm^3 s^{-1}	φ_{exp}[c] / %	k_{theo}[d] / 10^{-10} cm^3 s^{-1}	k^{min}_{theo}[d] / 10^{-10} cm^3 s^{-1}	k^{max}_{theo}[d] / 10^{-10} cm^3 s^{-1}
Et$_2$ZnH$^-$	H	9.6±0.2	68	9.6	8.2	11
	Et	1.7±0.5	12	5.7	4.5	7.1
Et$_2$Zn(OH)$^-$	OH	18 ±2	128	13	12	14
	Et	--[e]	--[e]	1.7	1.2	0.3
Et$_2$ZnF$^-$	F	2.6±0.9[f]	19[f]	--[g]	--[g]	--[g]
	Et	0.7±0.2	5	0.025	0.016	0.042
Et$_2$ZnCl$^-$	Cl	--[e]	--[e]	--[g]	--[g]	--[g]
	Et	0.041±0.01	0.31	0.025	0.016	0.041

[a] The experimental uncertainty corresponds to the statistical error from two independent measurements (95% confidence interval). [b] The experimental rate constants stem from the fit of the experimental data without consideration of the statistical factors. [c] The reaction efficiency φ_{exp} was calculated by dividing the experimental rate constant by the collision rate according to the capture theory by Su and Chesnavich. [d] In the theoretical modelling of the reaction kinetics, the symmetry number was taken into account. [e] No reaction was observed. [f] The reaction channel for Et$_2$Zn(OR)$^-$ and Et$_2$Zn(OR^{F3})HF$^-$ formation were summed up. [g] No theoretical rate constants were calculated as the approximation that the dissociation of the product complex is negligible no longer holds.

3.1.2 Variation of proton donor

After multiple changes in the proton acceptor, i.e. the organozincate anion, had been explored, it was probed how the variation of the proton donor affects the reactivity of the proton-transfer reactions of the organometallic species. For the homoleptic systems R_3Zn^- (R = Ph, Me), the alcohols 2,2,2-trifluoroethanol ($R^{F3}OH$), 2,2-difluoroethanol ($R^{F2}OH$), 2-fluoroethanol ($R^{F1}OH$), ethanol ($R^{F0}OH$), and water (H_2O) as well as formic acid (HCOOH) were used as proton donors in experimental and/or theoretical studies. In all cases, the protolysis reaction is expected to give RH and the organozincate $(R'O)ZnR_2^-$ (Scheme 13).
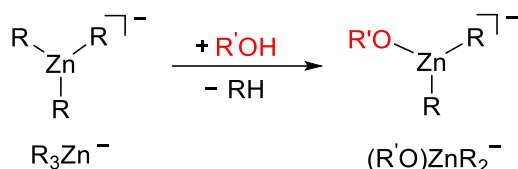
Scheme 13: Protolysis reactions of the homoleptic zincate anions R_3Zn^- (R = Ph, Me) by the proton donors R'OH (R' = CF_3CH_2, CF_2HCH_2, CFH_2CH_2, CH_3CH_2, H; HCO).

3.1.2.1 Reactions with alcohols and water

Ph_3Zn^- was prepared from a solution of $ZnCl_2$ and PhLi (4 equiv.), mass-selected and subjected to an ion-molecule reaction with the fluorinated ethanol derivative $R^{F2}OH$ (Figure 46, left). For the proton donor $R^{F1}OH$, the protonation reaction was slow and barely took place within the experimental time window. Therefore, the derived rate constant k_{exp} should only be considered as an upper limit (Figure 46, right). For the even less acidic proton donors $R^{F0}OH$ and H_2O, the reaction could not be observed at all.

In the kinetic measurements, some difficulties were encountered for the less acidic proton donors due to traces of the more acidic R'OH which resulted in significant side reactions. However, rinsing the gas-mixing chamber with liquid methanol and excessive flushing of the QIT with He could suppress the side reactions to an acceptable amount. Still, side reactions were observed but accounted for in the kinetic analysis of the experiments.

Figure 46: Left: Kinetic measurement (MS^n) of the gas-phase reaction of mass-selected Ph_3Zn^- with 2,2-difluoroethanol ($R^{F2}OH$; $N_{substrate}/V$ = 1.8 × 10^{11} cm^{-3}). The side reactions with residual $R^{F3}OH$ and HCOOH were accounted for in the kinetic modelling. R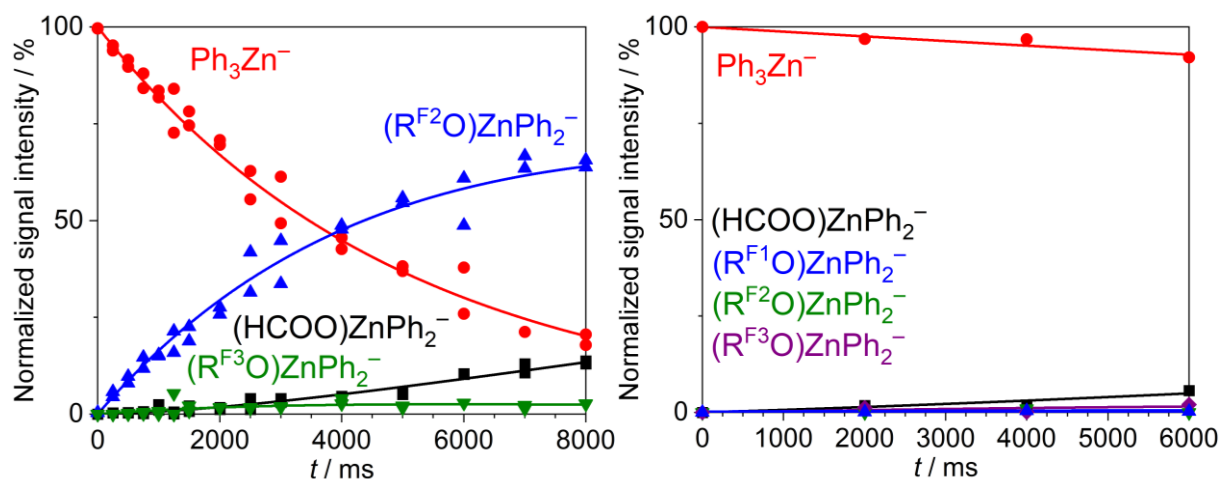ight: Kinetic measurement (MS^n) of the gas-phase reaction of mass-selected Ph_3Zn^- with 2-fluoroethanol ($R^{F1}OH$; $N_{substrate}/V$ = 1.7 × 10^{11} cm^{-3}). The side reactions with residual $R^{F2}OH$, $R^{F3}OH$ and HCOOH were accounted for in the kinetic modelling. However, the rate constant for the reaction of $Ph_3Zn^-/R^{F1}OH$ should only be considered an upper limit.

In an Eigen-type plot, an excellent linear correlation between the logarithmic rate constant k_{exp} and the gas-phase acidity ΔG_{acid} of the alcohol was found (Figure 47). Apparently, the increasing exothermicity of the proton-transfer reaction increases the rate constant.
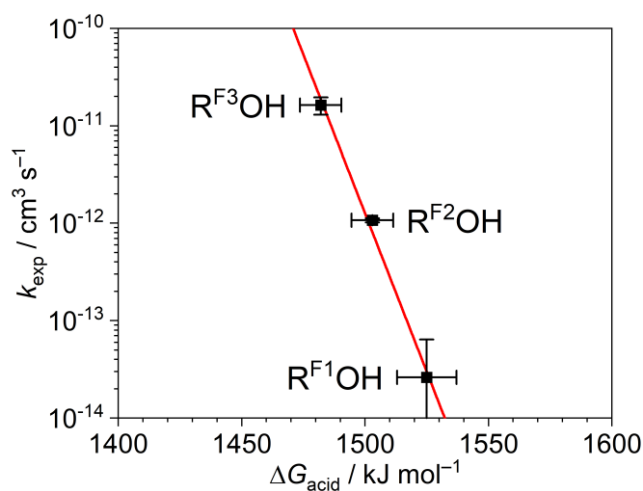

Figure 47: Correlation of the experimental rate constant k_{exp} with the gas-phase acidity of the denoted proton donors R'OH for Ph_3Zn^- and linear fit ($m = -0.07$, $R^2 = 0.99$).

Next, the reactions of Ph_3Zn^- with the proton donors R'OH were computed quantum-chemically. The structures of the species along the reaction pathway were optimized with the long-range corrected hybrid density functional ωB97X-D3 and def2-TZVP basis sets. Afterwards, electronic single-point energy calculations with the coupled-cluster method DLPNO-CCSD(T) and correlation-consistent basis sets cc-pVnZ (n = T; Q) were performed. In all systems, a double-well potential in terms of the enthalpy at 0 K, ΔH_0, was obtained as would be expected. However, from $R^{F3}OH$ to H_2O the reaction became less and less exothermic (from -109 to -52 kJ mol^{-1}). The change in the reaction energy $\Delta_r H_0$ was accompanied by the increase of the central barrier $\Delta H_0^{\ddagger}$. Whereas the energies of the TS and the product complex correlate fairly linearly with the reaction energy, this is much less given for the energy of the pre-reactive complex where the encounter complexes for the protonation by $R^{F0}OH$, $R^{F1}OH$ and $R^{F2}OH$ have very similar energies (Figure 48).
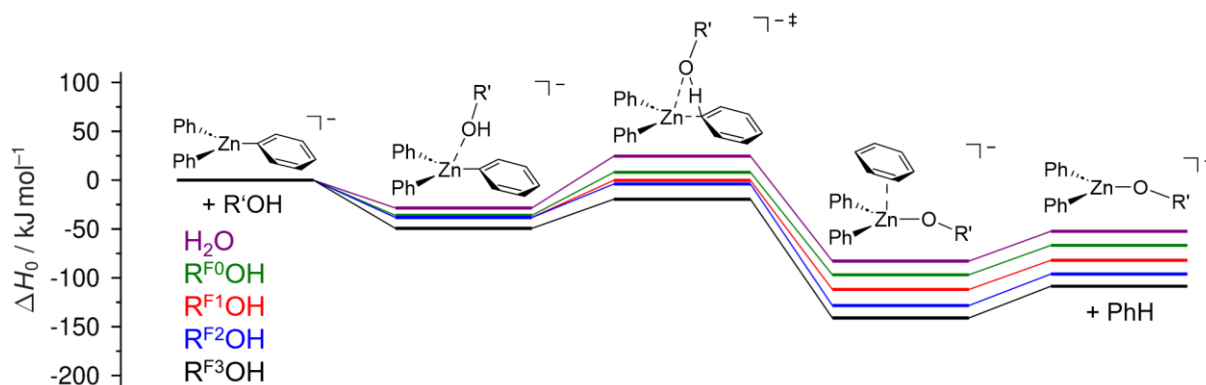
Figure 48: Reaction pathways for the protonation of Ph_3Zn^- by the proton donors R'OH (R' = CF_3CH_2, CF_2HCH_2, CFH_2CH_2, CH_3CH_2, H) as obtained from quantum-chemical calculations (DLPNO-CCSD(T)/cc-pV[T;Q]Z//ωB97X-D3/def2-TZVP).

Table 6: Energies of the stationary points along the reaction pathway for the protolysis reactions of Ph_3Zn^- by the different proton donors R'OH as obtained from quantum-chemical calculations (DLPNO-CCSD(T)/cc-pV[T;Q]Z//ωB97X-D3/def2-TZVP). The energies are given in terms of the enthalpy at 0 K, ΔH_0, relative to the reactants.

R'OH	ΔH_0 / kJ mol^{-1}			
	Pre-reactive complex	TS	Product complex	Products
$R^{F3}OH$	−49	−20	−141	−109
$R^{F2}OH$	−38	−4	−128	−96
$R^{F1}OH$	−38	0	−112	−82
$R^{F0}OH$	−36	+8	−97	−67
H_2O	−28	+25	−83	−52

A linear dependence of the central barrier $\Delta H_0^{\ddagger}$ on the reaction energy $\Delta_r H_0$ was found with a slope of m = +0.70±0.09 and an intercept of b = +59±8 (Figure 49, left). The slope is a measure of the sensitivity which is modulated by changes of the reaction energy. Furthermore, the intercept describes the central barrier for the (hypothetical) thermoneutral reaction between Ph_3Zn^- and a (hypothetical) proton donor R'OH and could be interpreted as the intrinsic barrier for such reactions.

The Brønsted-type correlation is similar to the LFER found for changing the basicity of the aryl moiety Ar^X via the *para*-substituents X (NMe$_2$, OMe, Me, H, F, Cl) as detailed in the beginning of section 3.1.1.1. Consequently, the theoretical rate constants k_{theo} which were obtained from Master-equation calculations decreased from the most acidic $R^{F3}OH$ to the least acidic H_2O as proton donors. The correlation between the logarithmic theoretical rate constants k_{theo} and the experimental gas-phase acidity ΔG_{acid} is only fairly linear which is due to the data points for $R^{F2}OH$ and H_2O. In the case of $R^{F2}OH$, the outlying can be traced back to the calculated central barrier $\Delta H_0^{\ddagger}$ that is, compared to its reaction energy, unexpectedly high (Figure 49, right).
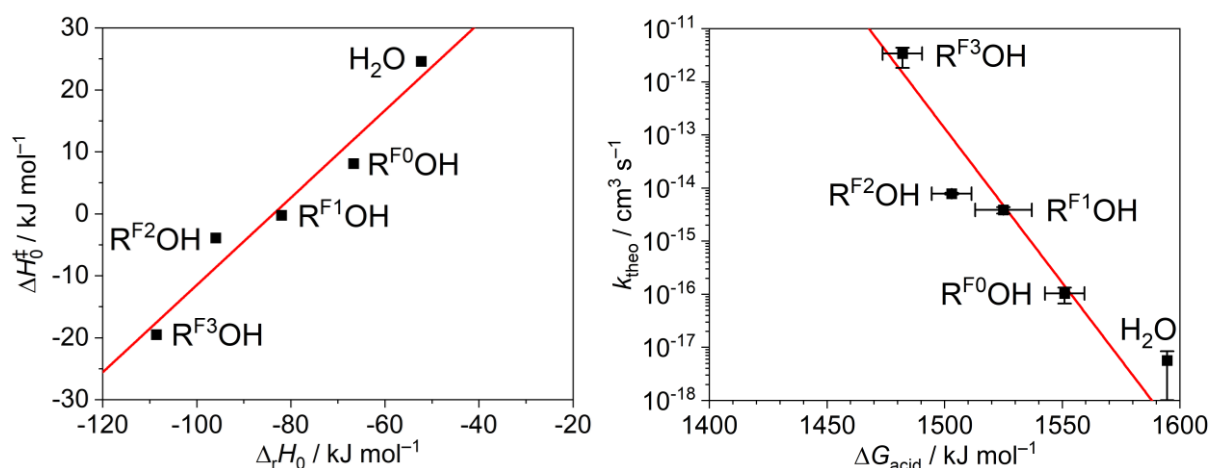
Figure 49: Correlation of the calculated central barrier $\Delta H_0^{\ddagger}$ with the reaction energy $\Delta_r H_0$ (left) as well as of the theoretical rate constant k_{theo} with the gas-phase acidity ΔG_{acid} (right) for the reaction of Ph_3Zn^- with the denoted proton donors R'OH (right). The data was fitted with linear regressions each (left: m = 0.70, b = +60; R^2 = 0.94; right: m = −0.04, R^2 = 0.55).

Interestingly, when the error bars for the theoretical rate constants were determined which result from the temperature uncertainty in the experiment T = (310±20) K, it was found that the temperature dependence of k_{theo} is reversed for low and high central barriers. For low central barriers ($\Delta H_0^{\ddagger}$ < −4 kJ mol^{-1}), k_{theo} decreases with increasing temperatures because

the reaction rate is largely dependent on the collision rate which, in turn, is proportional to $T^{-1/2}$. In contrast, for high central barriers ($\Delta H_0^{\ddagger} > -4$ kJ mol^{-1}) higher temperatures will also result in higher k_{theo} since the thermal distribution of the reactants is decisive for the reaction rate according to RRKM theory. With higher temperatures come higher internal energies of the reactants and thus, the number of particles with energies above the activation energy is increased rendering the reaction faster. Therefore, temperature-dependent kinetic measurements of ion-molecule reactions could give semi-quantitative information about the height of the associated barriers via the sign of the correlation of the temperature and rate constant. A more detailed analysis of the enthalpic and entropic contributions to the barriers is feasible by conducting an Eyring study.

The same experiments were carried out for the protolysis of Me$_3$Zn$^-$ by the proton donors R'OH (R' = CF$_3$CH$_2$, CF2HCH$_2$, CFH$_2$CH$_2$, CH$_3$CH$_2$, H). In all cases, the reaction rates were higher than for Ph$_3$Zn$^-$ by around one order of magnitude indicating that the barriers for the Me$_3$Zn$^-$ protolysis are always significantly reduced. This is in line with the results described in section 3.1.1.1. Similarly, a linear correlation between the experimental rate constant k_{exp} and gas-phase acidity ΔG_{acid} was observed demonstrating the effect according to the Hammond-Leffler postulate (Figure 50).
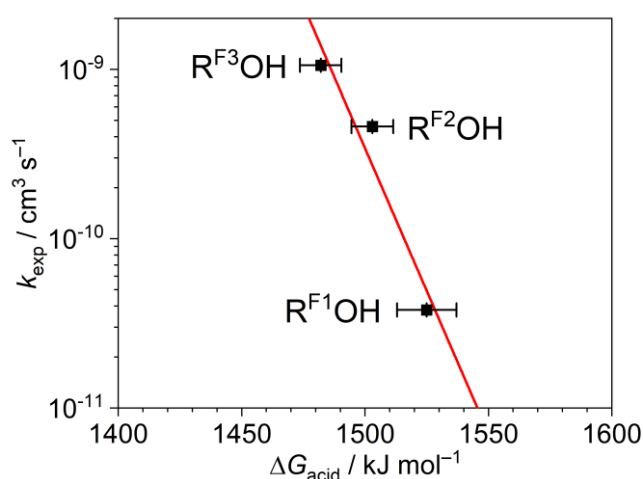
Figure 50: Correlation of the experimental rate constant k_{exp} with the gas-phase acidity of the denoted proton donors R'OH for Me$_3$Zn$^-$ and linear fit ($m = -0.03$, $R^2 = 0.86$).

The quantum-chemical calculations of the stationary points for the reaction of Me$_3$Zn$^-$ with R'OH were found to be similar to that of the Ph$_3$Zn$^-$ reactions (Figure 51). However, the reactions involving the trismethylzincate featured overall higher exothermicities and lower central barriers. The latter agrees well with the observed trend in the experiments. As for Ph$_3$Zn$^-$, the energies of the pre-reactive complexes scale much less directly with the reaction energy.
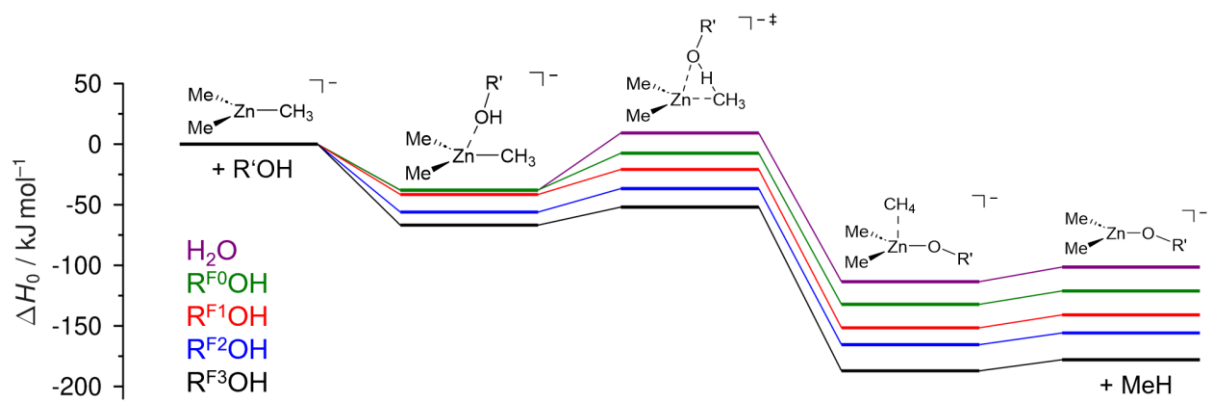
Figure 51: Reaction pathways for the protonation of Me_3Zn^- by the proton donors R'OH (R' = CF_3CH_2, CF_2HCH_2, CFH_2CH_2, CH_3CH_2, H) as obtained from quantum-chemical calculations (DLPNO-CCSD(T)/cc-pV[T;Q]Z//ωB97X-D3/def2-TZVP).

Table 7: Energies of the stationary points along the reaction pathway for the protolysis reactions of Me$_3$Zn$^-$ by the different proton donors R'OH as obtained from quantum-chemical calculations (DLPNO-CCSD(T)/cc-pV[T;Q]Z//ωB97X-D3/def2-TZVP). The energies are given in terms of the enthalpy at 0 K, ΔH_0, relative to the reactants.

| R'OH	ΔH_0 / kJ mol^{-1}			
	Pre-reactive complex	TS	Product complex	Products
R^{F3}OH	−67	−52	−187	−178
R^{F2}OH	−56	−37	−165	−156
R^{F1}OH	−42	−21	−152	−141
R^{F0}OH	−38	−7	−132	−121
H$_2$O	−38	+9	−114	−101

The quantitative assessment of the dependence of the central barrier $\Delta H_0^{\ddagger}$ on the reaction energy $\Delta_r H_0$ reveals a linear energy relationship with a slope of m = +0.81±0.03 and an intercept of b = +91±4 (Figure 52, left). The slope m as the sensitivity parameter agrees with that for Ph$_3$Zn$^-$. In contrast, the intercept b, which can be interpreted as the intrinsic barrier, is apparently much higher. This is in line with the finding that Ph protonation is favored over Me protonation in the mixed aryl-alkyl zincate anions Ph$_2$ZnMe$^-$ and PhZnMe$_2^-$ (cf. section 3.1.1.1).

In addition, the theoretical rate constants k_{theo} for the proton-transfer reactions of Me$_3$Zn$^-$ and R'OH (R' = CF$_3$CH$_2$, CF2HCH$_2$, CFH$_2$CH$_2$, CH$_3$CH$_2$, H) were obtained by carrying out Master-equation calculations with the program MESMER 6.0 based on the computed structures and energies of the stationary points. The methyl torsions were treated as low-frequency vibrations. All rate constants were higher than for the Ph$_3$Zn$^-$ set which is in agreement with the experiment. The Eigen-type correlation of the logarithmic rate constant k_{theo} as a function of the gas-phase acidity ΔG_{acid} gives a linear dependence and illustrates, in conjunction with the Brønsted-type plot, how the increase of the exothermicity resulting from the higher gas-phase acidity of the proton donors R'OH causes the activation barrier to decrease and, thereby, to accelerate the proton transfer (Figure 52, right).
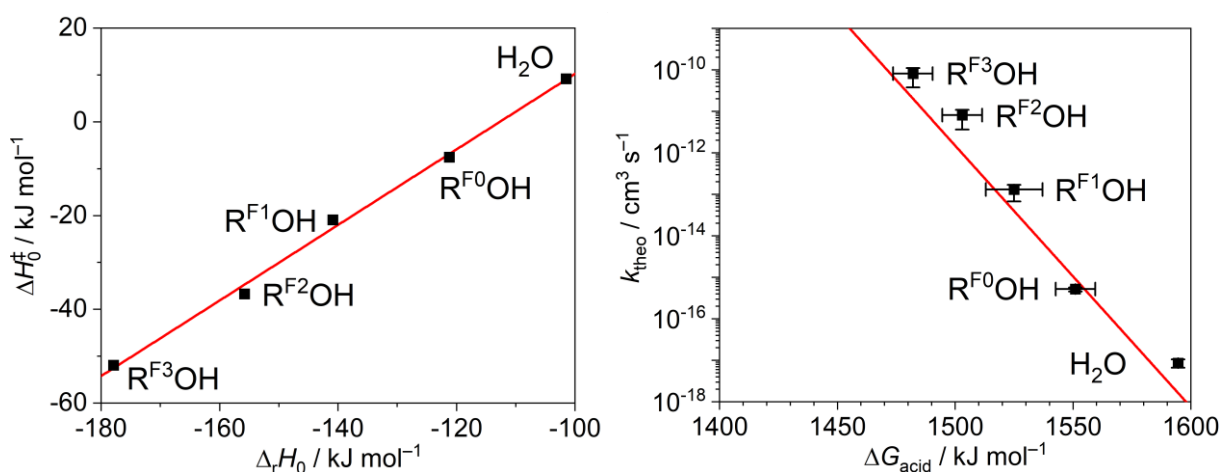
Figure 52: Correlation of the central barrier $\Delta H_0^{\ddagger}$ with the calculated reaction energy $\Delta_r H_0$ (left) as well as of the theoretical rate constant k_{theo} with the gas-phase acidity ΔG_{acid} (right) for the reaction of Me$_3$Zn$^-$ with the denoted proton donors R'OH (right). The data was fitted with linear regressions each (left: m = 0.81, b = +91; R^2 = 0.99; right: m = −0.06, R^2 = 0.90).

3.1.2.2   Reaction with formic acid

To probe the effects caused by the use of the more acidic carboxylic acids R'COOH, mass-selected Ph_3Zn^- was subjected to an ion-molecule reaction with formic acid (HCOOH). In analogy to the reactions with alcohols $R^{Fn}OH$ (n = 1, 2, 3), the protonation reaction converting Ph_3Zn^- into the protolyzed product $(HCOO)ZnPh_2^-$ was observed (k_{exp} = $(4.2\pm0.1) \times 10^{-11}$ cm^3 s^{-1}). In addition, the second protonation was observed giving the organozincate anions $(HCOO)_2ZnPh^-$ although the reaction was 63 times slower with k_{exp} = $(6.7\pm2.0) \times 10^{-13}$ cm^3 s^{-1} (Figure 53). It seems that the first protonation drastically deactivates the zincate for the second protonation. This can easily be rationalized with chemical intuition. For one, the coordination sphere of the metal center changes from trigonal in Ph_3Zn^- to tetragonal in $(HCOO)ZnPh_2^-$ because $HCOO^-$ will likely coordinate the metal center in a bidentate fashion. Thereby, the access of HCOOH to the other phenyl moieties is hampered. Moreover, it is likely that an electronic effect is in action. The changing of Ph^- to $HCOO^-$ lowers the overall electron density in the organozincate system. Thus, also the electron density at the remaining phenyl moieties is reduced which increases the barrier for the consecutive protonation.
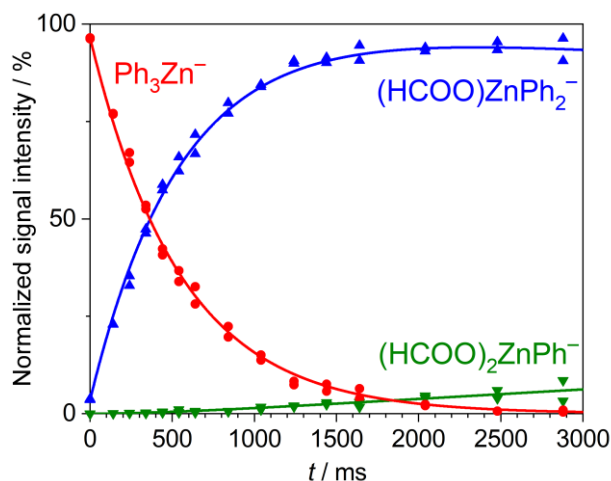
Figure 53:   Kinetic measurement (MS^n) of the gas-phase reaction of mass-selected Ph_3Zn^- with formic acid (HCOOH; $N_{substrate}/V$ = 4.4 × 10^{10} cm^{-3}).
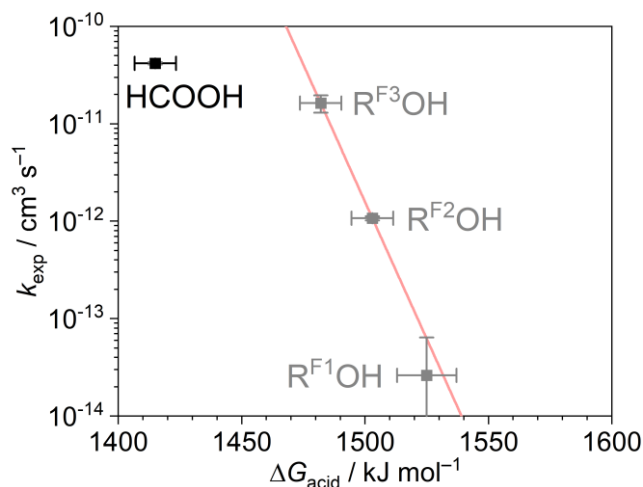
Figure 54:   Correlation of the experimental rate constant k_{exp} with the gas-phase acidity of the denoted proton donors R'OH for Ph_3Zn^- and linear regressions (red line) of the data (m = −0.06, R^2 = 0.99). Evidently, HCOOH does not match the linear fit and was thus disregarded.

If the obtained experimental rate constant for the first protonation of Ph_3Zn^- (to $(HCOO)ZnPh_2^-$) is added in the Eigen-type correlation of the logarithmic rate constants k_{exp} with the gas-phase acidities ΔG_{acid} for the alcohols $R^{Fn}OH$, it appears that the data point does not match the linear trend. This hints to a change in the reaction mechanism. Indeed, a six-membered transition structure is found instead of a four-membered TS for the reactions with the alcohols (Figure 55).
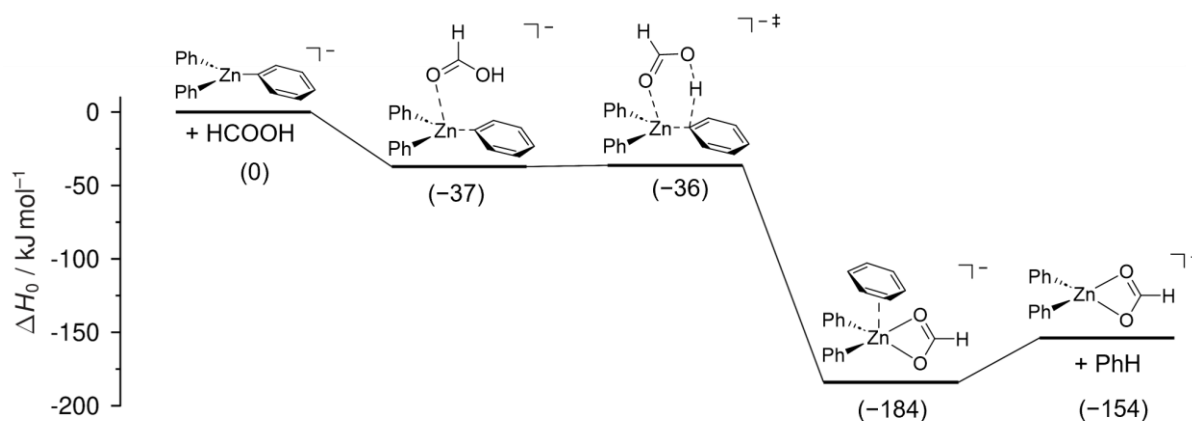
Figure 55: Reaction pathway for the reaction of Ph_3Zn^- with HCOOH as obtained from quantum-chemical calculations (DLPNO-CCSD(T)/cc-pV[T;Q]Z//ωB97X-D3/def2-TZVP).

Based on the quantum-chemical computations a theoretical rate constant of k_{theo} = 4.5×10^{-10} cm^3 s^{-1} was calculated. The experimental and theoretical rate constants k_{exp} and k_{theo}, respectively, for the protolysis of Ph_3Zn^- by the proton donors $R^{Fn}OH$ (n = 1, 2, 3) and HCOOH were compared with each other. For $R^{F3}OH$, $R^{F1}OH$ and HCOOH k_{exp} and k_{theo} agree within factors of 5, 7 and 11. In marked contrast, k_{theo} is more than two orders of magnitude lower than the experimental value for Ph_3Zn^-/$R^{F2}OH$ (Figure 56). Just as in Figure 49, this suggests that the calculated central barrier $\Delta H_0^{\ddagger}$ for $R^{F2}OH$ is too high. It could also indicate the increasing relevance of proton tunneling for the proton-transfer reaction.
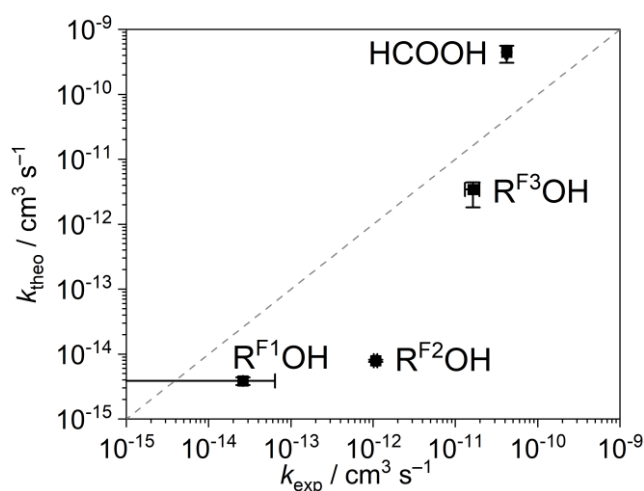
Figure 56: Comparison of the experimental and theoretical rate constants k_{exp} and k_{theo}, respectively, for the protolysis reactions of Ph_3Zn^- with the denoted proton donors.

R'OH	k_{exp}[a] / 10^{-12} cm^3 s^{-1}	φ_{exp}[b] / %	k_{theo}[c] / 10^{-12} cm^3 s^{-1}	k^{min}_{theo}[c] / 10^{-12} cm^3 s^{-1}	k^{max}_{theo}[c] / 10^{-12} cm^3 s^{-1}
R^{F3}OH	16.3±0.3	1.3	3.4	2.5	5.0
R^{F2}OH	1.1±0.1	0.15	0.0079	0.0076	0.0082
R^{F1}OH	0.026±0.038	0.0021	0.0039	0.0034	0.0044
HCOOH	41.8±1.3	2.9	448	335	588

[a] The experimental uncertainty corresponds to the statistical error from two independent measurements (95% confidence interval). [b] The reaction efficiency φ_{exp} was calculated by dividing the experimental rate constant by the collision rate according to the capture theory by Su and Chesnavich. [c] In the theoretical modelling of the reaction kinetics, the symmetry number of Ph$_3$Zn$^-$ was taken into account.

The reaction of Me$_3$Zn$^-$ with formic acid was studied. Although the consecutive protonation reactions were observed as well, the kinetic measurement of the ion-molecule reaction of Me$_3$Zn$^-$/HCOOH deviated distinctively from that of Ph$_3$Zn$^-$/HCOOH because extensive amounts of formate HCOO$^-$ and the proton-bound formate dimer (HCOO)H(OOCH)$^-$ were present in the experiments (Figure 57).
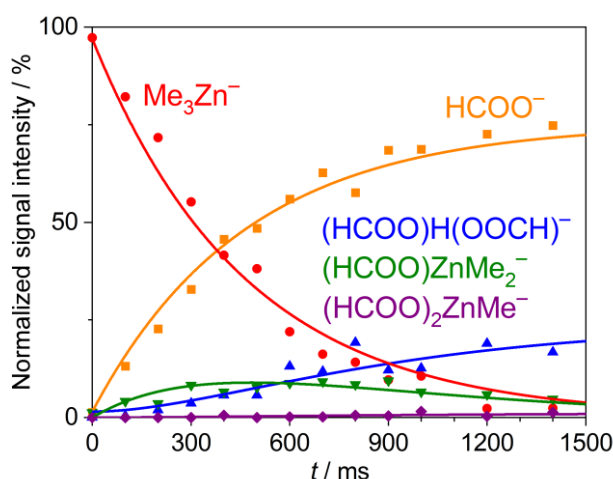
Figure 57: Kinetic measurement (MS^2) of the gas-phase reaction of mass-selected Me$_3$Zn$^-$ with formic acid (HCOOH; $N_{substrate}/V = 4.4 \times 10^{10}$ cm^{-3}).

Accordingly, the kinetic analysis of the experimental data is much more challenging due to the number of possible branches in the reaction network. In this case, the reaction network was assumed to be as depicted in Scheme 14 because it gave a visually appropriate fit of the data. In this framework, the collision of HCOOH with the organozincate anions Me$_3$Zn$^-$ and (HCOO)ZnMe$_2^-$ can either result in the protolysis according to the typical proton-transfer mechanism giving (HCOO)ZnMe$_2^-$ or (HCOO)$_2$ZnMe$^-$. Alternatively, some kind of "stripping" proton transfer occurs in which the formic acid transfers the proton onto one methyl moiety without coordinating to the zinc center. Thereby, an adduct of ZnMe$_2$ and MeH forms which will quickly dissociate subsequently. Experimental rate constants of k_{exp} = (1.3±0.2) × 10^{-11} and (2.2±0.3) × 10^{-12} cm^3 s^{-1} and for the first and second protonation, respectively, were obtained.

$$Me_3Zn^- \xrightarrow[-MeH]{+HCOOH} (HCOO)ZnMe_2^- \xrightarrow[-MeH]{+HCOOH} (HCOO)_2ZnMe^-$$

$$\Big\downarrow \begin{matrix} -ZnMe_2 \\ -MeH \end{matrix} +HCOOH \qquad \Big\downarrow \begin{matrix} -ZnMe_2 \\ -MeH \end{matrix} +HCOOH$$

$$HCOO^- \qquad\qquad (HCOO)H(OOCH)^-$$
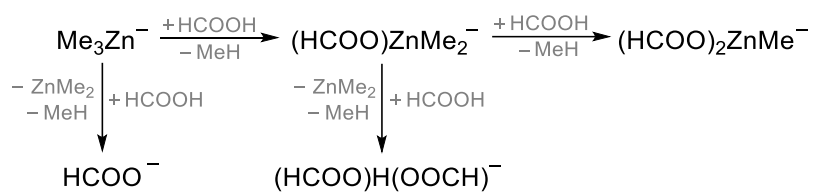
Scheme 14:   Reaction scheme as applied to fit the kinetic measurement of the gas-phase reaction of Me_3Zn^- with HCOOH.

However, the reaction dynamics of the system Me_3Zn^-/HCOOH are not clear at all. Therefore, a more detailed and systematic analysis of the experimental data is required.

As the experiment is not sufficiently understood yet, quantum-chemical calculations will not be reported on at this point.

3.2 Protonation of organoferrate anions

Organoiron species are of increasing interest as the play vital roles in iron-catalyzed cross-coupling reactions.[157] Koszinowski and coworkers identified various organoferrate species in such reactions and characterized their unimolecular reactivity and behavior towards oxidative addition.[103,158–162] Aside from their chemical meaning, they also pose more complex model systems for the investigation of the barriers of protonation reactions of organometallics as they often feature open-shell electronic configuration. In that sense, the scope of the species investigated within this thesis was expanded by switching the metal center from the closed-shell $Zn(+II)$ ($3d^{10}$) to $Fe(+II)$ with the open-shell electronic configurations $3d^6$. Just as their zincate congeners, the organoferrate anions R_3Fe^- (R = Ph, Mes ($C_6H_2(CH_3)_3$), Tol (p-$C_6H_4CH_3$)) and Mes_2FeBr^- featured three negatively charged substituents. After establishing the effects of the substituents themselves, the influence of the spin-electronic effects onto the intrinsic reactivity could be probed in such a research design.

The following results largely emerged in the context of the "Fe-MAN" challenge which stands for "Ferrates – Microkinetic Assessment of Numerical quantum chemistry".[163] The experimental work was carried out by the author of this dissertation, whereas the theoretical calculations originate from the participants of the challenge. In this section, the quantum-chemical calculations by Kosala N. Amarasinghe, Muhammad Shafique and Milica Feldt from the Leibniz Institute for Catalysis (LIKAT) in Rostock, Germany, as well as of Luxuan Guo and Jeremy N. Harvey, KU Leuven, were used. The idea of such a blind challenge is to rigorously separate the experimental from the theoretical studies, i.e. experimental groups determine the values of the specified observable and keep them secret. In the meantime, computational chemistry groups calculate the values of said observable without their knowing of the experimental results. Only afterwards, experiment and theory are compared. In such a fashion, it is possible to benchmark the predictive performance of the computational methods against experimental reference data.

In this section, the reactions of the organoferrate anions R_3Fe^- and R_2FeBr^- (R = Ph, Mes, Tol) (Scheme 15) with 2,2,2-trifluoroethanol ($R^{F3}OH$) or 2,2-difluoroethanol ($R^{F2}OH$) were studied. Condensed-phase experiments with Mes_3Fe^- suggest that these iron species are high spin (S = 2).[164] Therefore, quantum-chemical calculations were carried out assuming that the organoferrate anions were in a quintett state and remained in such throughout the course of the protolysis reaction series.
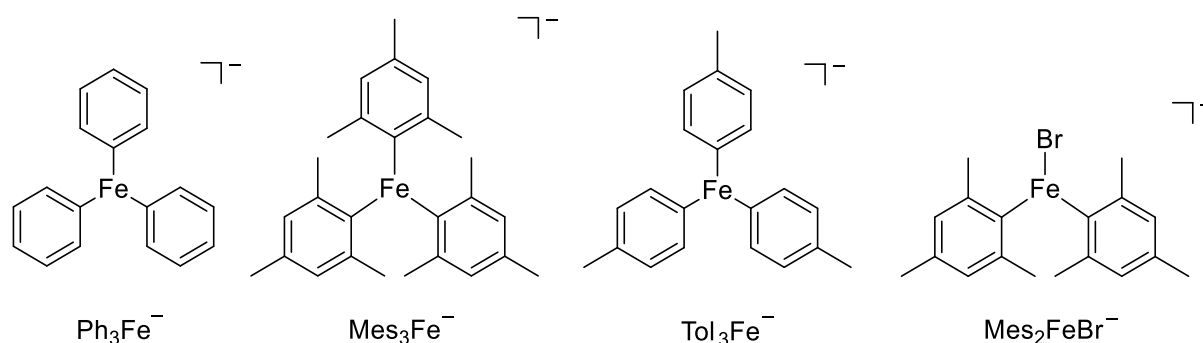
Scheme 15: Organoferrate anions R_3Fe^- (R = Ph, Mes, Tol) and Mes_2FeBr^- whose protolysis reaction by $R^{F3}OH$ or $R^{F2}OH$ were studied in this section.

3.2.1 Variation of the proton acceptor

The negative ion-mode electrospray ionization mass spectrum of a solution of Fe(acac)$_3$ (acac: acetylacetonate) and PhMgCl (4 equiv.) in THF (10 mM) at 273 K showed the three species Ph$_4$Fe$^-$, Ph$_3$Fe$^-$ and Ph$_2$Fe$^-$ featuring the iron center in the oxidation states +III, +II and +I, respectively. Ph$_3$Fe$^-$ was the most abundant ion present (Figure 58, left).

As an Fe(+III) salt was used as the iron source, the Fe(+I) and Fe(+II) species must originate from chemical reactions in the sample solution or the ESI source. Either the Fe(+III) species was reduced by the Grignard reagent or by electrochemical reduction as a consequence of the applied high voltage in the electrospraying process. Ph$_2$Fe$^-$ most probably resulted from in-source CID wherein Ph$_4$Fe$^-$ undergoes reductive elimination. This hypothesis is supported by the fact that Ph$_2$Fe$^-$ had not been observed previously at presumably "softer" ESI settings at the same mass spectrometer but in gas-phase fragmentation experiments.[158,160–162]

The organoferrate anion Ph$_3$Fe$^-$ was mass-selected and subjected to an ion-molecule reaction with 2,2,2-trifluoroethanol (R^{F3}OH) in the 3D quadrupole ion trap at $T = (310\pm20)$ K.[14] The complete protolysis of the ion with three consecutive protonation reactions occured which is in contrast to the protolysis of Ph$_3$Zn$^-$ by R^{F3}OH where only the first protonation could be observed. First, Ph$_3$Fe$^-$ reacted with R^{F3}OH to give (R^{F3}O)FePh$_2^-$ and, by means of mass balance, benzene (PhH). Second, (R^{F3}O)FePh$_2^-$ was protonated by R^{F3}OH at the phenyl site resulting in (R^{F3}O)$_2$FePh$^-$ (and PhH). At last, the reaction of (R^{F3}O)$_2$FePh$^-$ and R^{F3}OH yielded the trisalkoxyferrate anion (R^{F3}O)$_3$Fe$^-$ (and PhH). Furthermore, the side reaction of Ph$_3$Fe$^-$ with residual HCOOH in the QIT was found giving (HCOO)FePh$_2^-$ and benzene. Within a reaction time t of 1000 ms, almost all Ph$_3$Fe$^-$ was consumed. (Figure 58, right).
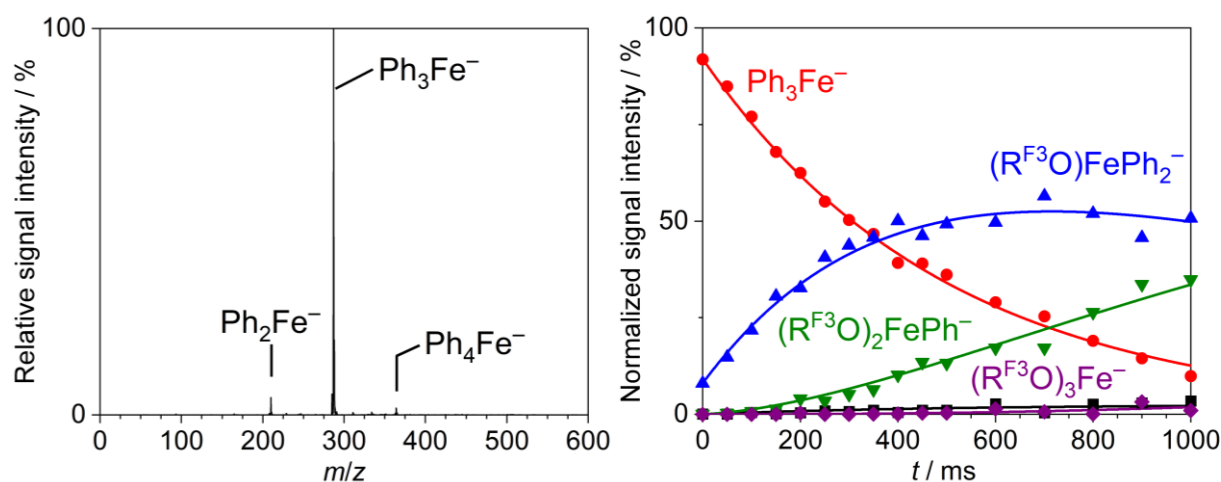
Figure 58: Left: Negative ion-mode electrospray ionization (ESI) mass spectrum (MS^1) of a solution of the products formed in the reaction of Fe(acac)$_3$ with PhMgCl (4 equiv.) in THF (10 mM) at 273 K. Right: Kinetic measurement (MS^2) of the gas-phase reaction of mass-selected Ph$_3$Fe$^-$ with 2,2,2-trifluoroethanol (R^{F3}OH; $N_{substrate}/V = 8.5 \times 10^{10}$ cm^{-3}). The side reaction with HCOOH was observed (black) and accounted for in the kinetic modelling.

---

[14] The ion-molecule reaction of Ph$_4$Fe$^-$ with R^{F3}OH was too slow to be observed within the experimental time window ($k_{exp} < 10^{-14}$ cm^3 s^{-1}). In the kinetic measurement of Ph$_2$Fe$^-$ with R^{F3}OH, so many side reactions with unknown substrates took place that no meaningful analysis was feasible as the signals could not be attributed properly. The protonation reaction under scrutiny occurred only to a small degree relative to the side reactions.

To support the validity of the kinetic measurements, gas-phase experiments with varying amounts of $R^{F3}OH$ were carried out. As the ion-molecule reaction proceeds under pseudo-first order conditions with an excess of the substrate 2,2,2-trifluoroethanol, it is expected that the effective rate constant k_{eff} scales linearly with the volume $V_{substrate}$ that was introduced into the QIT. In fact, such linear correlations were obtained for the reactions of Ph_3Fe^- and $(R^{F3}O)FePh_2^-$ with $R^{F3}OH$ which strongly supports the validity of the experimental setup (Figure 59).
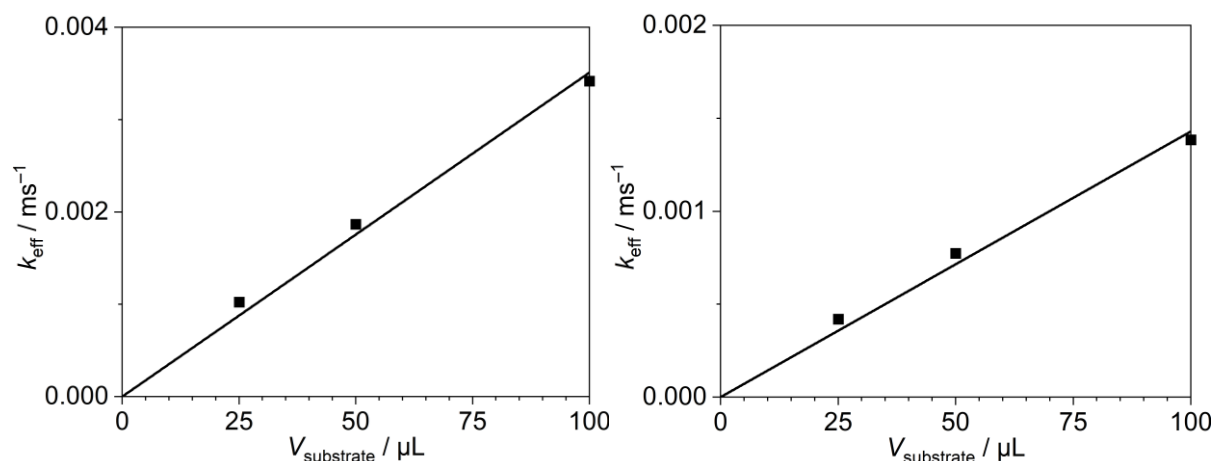
Figure 59: Correlations of the effective rate constant k_{eff} with the used substrate volume $V_{substrate}$ for the protonation of mass-selected Ph_3Fe^- (left) and $(R^{F3}O)FePh_2^-$ (right) by the substrate 2,2,2-trilfuoroethanol ($R^{F3}OH$). The substrate volumina $V_{substrate}$ of 25, 50 and 100 µL correspond to substrate concentrations $N_{substrate}/V$ of 4.3×10^{10}, 8.5×10^{10} and 1.7×10^{11} cm^{-3}, respectively. The data points are well fitted by linear regressions with their intercepts set to 0 ($R^2 = 0.997$ and 0.998, respectively).

From the kinetic measurements, bimolecular rate constants k_{exp} of $(2.2\pm0.3) \times 10^{-11}$, $(9.1\pm1.4) \times 10^{-12}$ and $(9.3\pm9.0) \times 10^{-13}$ cm^3 s^{-1} were determined for the first, second and third proton-transfer reaction, respectively. Because the last protonation was so slow, the rate constant is associated with an unusually high uncertainty. For the first and second protonation, the rate constants correspond to reaction efficiencies φ_{exp} of 1.8% and 0.7% which indicates significant central barriers associated with the proton-transfer reaction. The order of the rate constants suggests that the preceding protonation reaction deactivates the organoferrate for the subsequent one.

For more detailed insight into the mechanisms of the proton-transfer reactions, quantum-chemical calculations ($S(Fe(+II)) = 2$) were performed by Amarasinghe, Shafique and Feldt. In line with the previously applied computational protocol, they optimized the structures of the stationary points along the reaction pathway with the long-range corrected hybrid density functional ωB97X-D3[137–139] and Ahlrichs' def2-TZVP basis sets[140] with the program suite ORCA by Neese and coworkers.[116,117] Thereafter, electronic single-point energy calculations with the local coupled-cluster method DLPNO-CCSD(T) were run with ORCA. However, they used def2-TZVP basis sets (instead of Dunning's correlation-consistent cc-pVnZ (n = T; Q) basis sets) which is slightly different from the previous workflow for the quantum-chemical calculations.

Amarasinghe, Shafique and Feldt obtained double-well potentials for protonation of Ph_3Fe^- and $(R^{F3}O)FePh_2^-$ by $R^{F3}OH$ in terms of the enthalpy at 0 K, ΔH_0, which is the most suitable energy to describe gas-phase reactions under low-pressure conditions (microcanonical ensemble). Both reactions are strongly exothermic with reaction enthalpies $\Delta_r H_0$ of −110

and −122 kJ mol^{-1} and central barriers of $\Delta H_0^{\ddagger}$ of −23 and −19 kJ mol^{-1}, respectively. In agreement with the experimental result, the activation barrier for the second protonation was found to be higher than for the first one. Moreover, the calculations suggest that the reaction kinetics are not directly connected to the thermochemistry as the reaction with the higher central barrier also features the higher exothermicity (Figure 60). This is in contrast to the findings for the protolysis of the trisarylzincate anions where an increase in the gas-phase acidity was always associated with a lowering of the central barrier (cf. section 3.1.1.1). Perhaps, that hints to shortcomings of the theoretical calculations for the case of the Ph$_3$Fe$^-$ protonation.
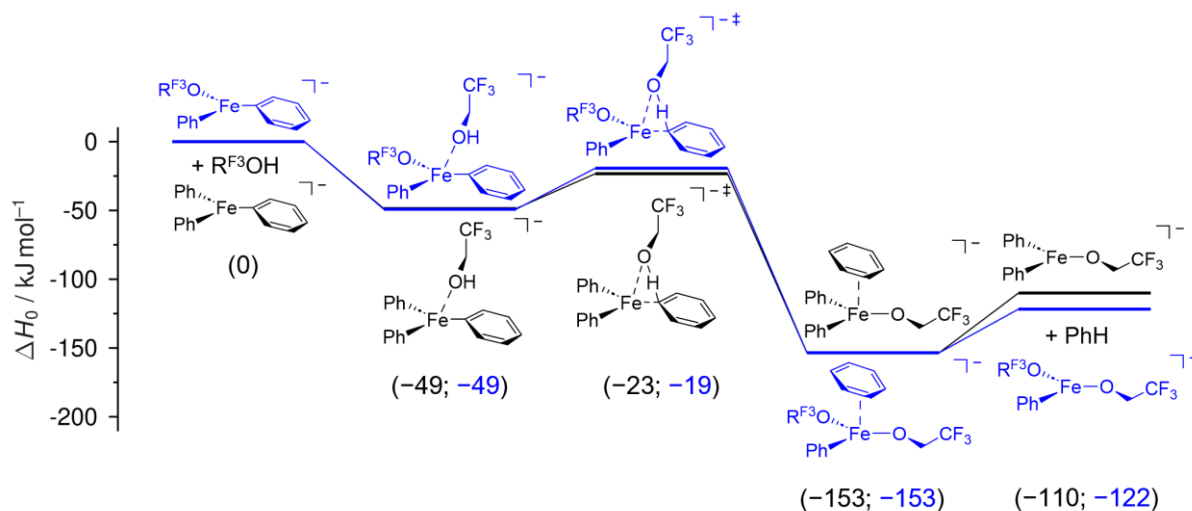
Figure 60: Reaction pathway for the phenyl protonation reaction of Ph$_3$Fe$^-$ (black) and (R^{F3}O)FePh$_2^-$ (blue) with 2,2,2-trifluoroethanol (R^{F3}OH) as obtained from quantum-chemical calculations (DLPNO-CCSD(T)/def2-TZVP//ωB97X-D3/def2-TZVP). The calculations were carried out by Kosala N. Amarasinghe, Muhammad Shafique and Milica Feldt.

Next, the species Mes$_3$Fe$^-$ was investigated. It was prepared from electrospraying a solution of Fe(acac)$_3$ and MesMgBr (4 equiv.) in THF (10 mM) at 273 K. Interestingly, the negative ion-mode ESI mass spectrum showed minor amounts of Mes$_2$FeBr$^-$ (identified by the *m/z* ratio and the distinct Br isotope pattern) but no intensities for the Fe(+I) species Mes$_2$Fe$^-$ or the Fe(+III) species Mes$_4$Fe$^-$.[158,160–162] Apparently, due to the steric demand of the mesityl moieties Mes$_4$Fe$^-$ cannot form or readily undergoes some kind of reduction or radical loss to give Mes$_3$Fe$^-$. As there was no Mes$_4$Fe$^-$, no reductive elimination could take place to give the Fe(+I) species Mes$_2$Fe$^-$ (Figure 61, left).

In the gas-phase ion-molecule reaction of isolated Mes$_3$Fe$^-$ with 2,2,2-trifluoroethanol (R^{F3}OH), the entire protolysis with the three consecutive protonation reactions giving (R^{F3}O)FeMes$_2^-$, (R^{F3}O)$_2$FeMes$^-$ and (R^{F3}O)$_3$Fe$^-$, respectively, was observed. This is similar to the system Ph$_3$Fe$^-$/R^{F3}OH. In contrast though, the product of the first protonation is only present in very small intensities. Apparently, the first protonation is very slow, but the second is so fast that (R^{F3}O)FeMes$_2^-$ is virtually instantaneously transformed into (R^{F3}O)$_2$FeMes$^-$.

Although the overall reaction time (*t* = 5000 ms) was much longer, only 50% of the reactant ion Mes$_3$Fe$^-$ were converted. The protolysis of Mes$_3$Fe$^-$ appears to be surprisingly slow. The kinetic analysis gave experimental rate constants of k_{exp} = (8.2±1.5) × 10^{-13}, (3.4±2.4) × 10^{-11} and (7.2±5.1) × 10^{-13} cm^3 s^{-1} for the first, second and third protonation, respectively. The second and third rate constants bear large experimental uncertainties.

Figure 61: Left: Negative ion-mode electrospray ionization (ESI) mass spectrum (MS[1]) of a solution of the products formed in the reaction of Fe(acac)$_3$ with MesMgBr (4 equiv.) in THF (10 mM) at 273 K. Right: Kinetic measurement (MS[n]) of the gas-phase reaction of mass-selected Mes$_3$Fe$^-$ with 2,2,2-trifluoroethanol (R^{F3}OH; $N_{substrate}/V = 1.7 \times 10^{11}$ cm^{-3}). Side reactions with HCOOH were observed (gray, black) and accounted for in the kinetic modelling.

Amarasinghe, Shafique and Feldt performed quantum-chemical calculations (DLPNO-CCSD(T)/def2-TZVP//ωB97X-D3/def2-TZVP) considering Fe(+II) to be in a quintett spin state ($S = 2$). This time, however, they only managed to compute the reaction pathway for the second protonation reaction from (R^{F3}O)FeMes$_2^-$ to (R^{F3}O)$_2$FeMes$^-$. They found that the central barrier of $\Delta H_0^\ddagger = -35$ kJ mol^{-1} is lower than for (R^{F3}O)FePh$_2^-$/R^{F3}OH which is in line with the experimentally determined rate constants where the second protonation within the Mes$_3$Fe$^-$ protolysis series is faster than in the Ph$_3$Fe$^-$ series (Figure 62).
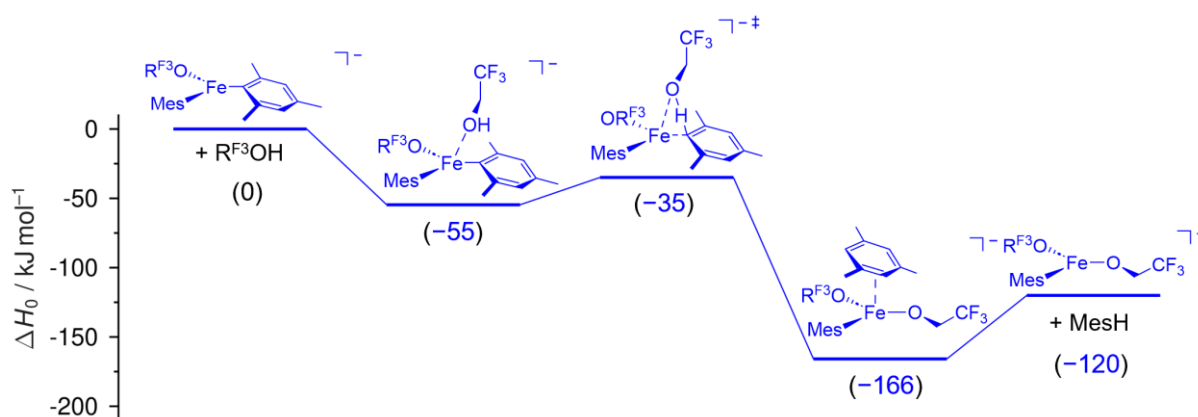
Figure 62: Reaction pathway for the mesityl protonation reaction of (R^{F3}O)FeMes$_2^-$ (blue) with 2,2,2-trifluoroethanol (R^{F3}OH) as obtained from quantum-chemical calculations (DLPNO-CCSD(T)/def2-TZVP//ωB97X-D3/def2-TZVP). The calculations were carried out by Kosala N. Amarasinghe, Muhammad Shafique and Milica Feldt.

It seems that the second protonation is the fastest in the protolysis series which is in contrast to Ph$_3$Fe$^-$/R^{F3}OH where the rate constants decreases from the first over the second to the third reaction. The observed reactivity is likely the consequence of the mesityl groups, i.e. their steric effects. In the first protonation reaction from Mes$_3$Fe$^-$ to (R^{F3}O)FeMes$_2^-$, the proton transfer to the accepting carbon atom of the mesityl is hampered by the methyl groups of the mesityl residues resulting in an increased barrier and low rate. For the second protonation from (R^{F3}O)FeMes$_2^-$ to (R^{F3}O)$_2$FeMes$^-$, however, the methyl

groups of the mesityl moiety no longer hamper sterically but instead act as electronic facilitators. As electron-donating groups they raise the electron density at the accepting carbon atom and thereby lower the central barrier for the proton transfer. The influence is similar to the effect in the Hammett study of the organozincate anions $Ar^XZnPh_2^-$ with X = OMe and Me (cf. section 3.1.1.1).

To validate the hypothesis above, the *para*-substituted tristolylferrate Tol_3Fe^- was prepared from a solution of $Fe(acac)_3$ and TolMgBr (4 equiv.) in THF at 273 K. The negative ion-mode ESI source mass spectrum showed the Fe(+III), Fe(+II) and Fe(+I) species Tol_4Fe^-, Tol_3Fe^- and Tol_2Fe^-, respectively. Tol_2Fe^- was likely formed from the reductive elimination of Tol–Tol from Tol_4Fe^- in an in-source CID process. Moreover, minor amounts of Tol_2FeBr^- as in the $Fe(acac)_3$/MesMgBr mass spectrum were observed. Interestingly, even the protolysis product $(R^{F3}O)FeTol_2^-$ was present in the ESI mass spectrum. That indicates that Tol_3Fe^- is more reactive than Mes_3Fe^- and Ph_3Fe^- as the protonation reaction can occur even within the short time of the mass scan (only a few ms) within the QIT (Figure 63, left).

Tol_3Fe^- was mass-selected and allowed to react with the proton donor 2,2,2-trifluoroethanol ($R^{F3}OH$) in the gas phase. Just as for Ph_3Fe^-, the entire protolysis series with the three protonation steps was observed, each releasing TolH and attaching $R^{F3}O^-$ to the iron center. Within 1000 ms the reactant ion was completely consumed. From the kinetic analysis, bimolecular rate constants of k_{exp} = (3.5±0.3) × 10^{-11}, (1.2±0.1) × 10^{-11} and (9.1±2.6) × 10^{-13} $cm^3\ s^{-1}$ were obtained for the three consecutive proton-transfer reactions (Figure 63, right). The rate constants decrease with each protonation step meaning that substituting a Tol for a $R^{F3}O$ substituent at the metal center lowers the intrinsic reactivity of the organoferrate anion. This is probably caused by an increase of the Lewis acidity of the Fe(+II) which renders the residual Tol groups less basic. The effect is the same as in the reaction of Ph_3Fe^- with $R^{F3}OH$.
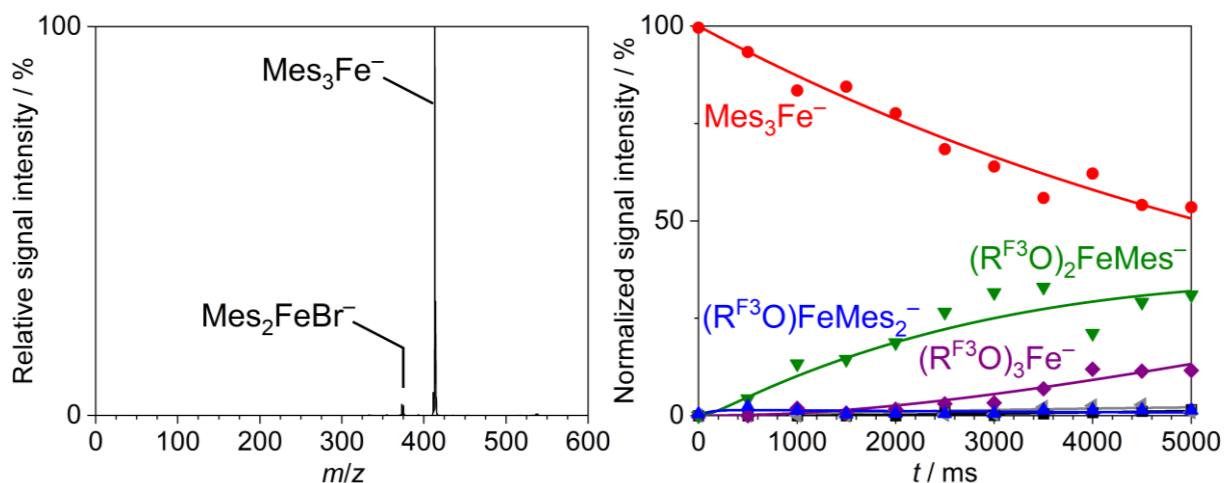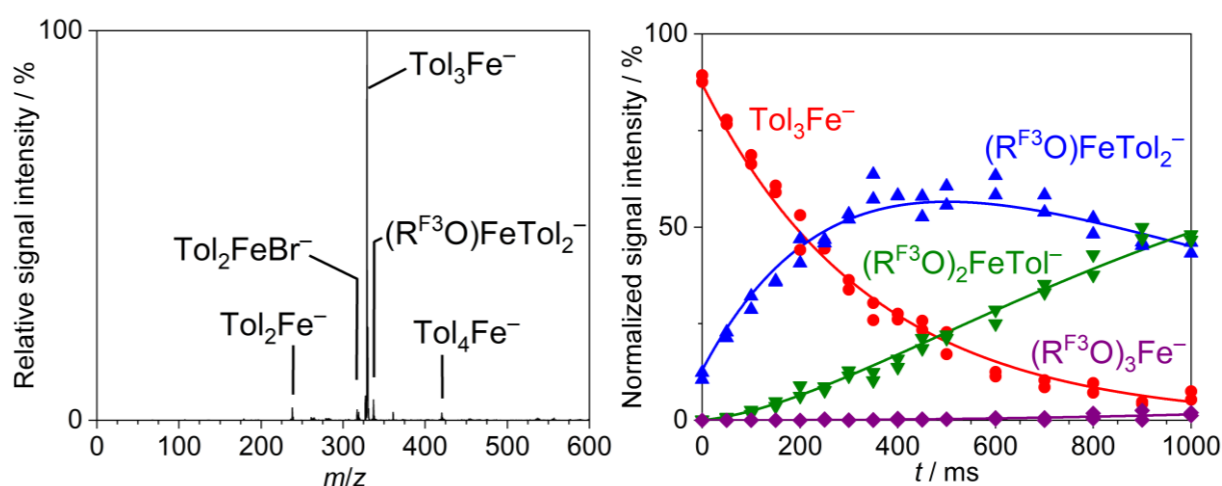

Figure 63:　Left: Negative ion-mode electrospray ionization (ESI) mass spectrum (MS[1]) of a solution of the products formed in the reaction of $Fe(acac)_3$ with TolMgBr (4 equiv.) in THF (10 mM) at 273 K. Right: Kinetic measurement (MS[2]) of the gas-phase reaction of mass-selected Tol_3Fe^- with 2,2,2-trifluoroethanol ($R^{F3}OH$; $N_{substrate}/V$ = 8.5 × 10^{10} cm^{-3}).

At last, the organoferrate anion Mes_2FeBr^- was subjected to an ion-molecule reaction with $R^{F3}OH$. Aside from the side reaction with HCOOH, two reactions were observed, i.e. the first protonation from Mes_2FeBr^- to $(R^{F3}O)MesFeBr^-$ as well as the second protonation from $(R^{F3}O)MesFeBr^-$ to $(R^{F3}O)_2FeBr^-$. The protonation of the Br group was not observed

(Figure 64). This is in line with the results from the protolysis of the organozincate anions Et_2ZnX^- (X = F, Cl) where F protonation was observed but Cl protonation not due to the higher gas-phase acidity of HCl (cf. section 3.1.1.2). As HBr features an even higher gas-phase acidity than HCl, Br protonation is not expected.

The experimental rate constants were determined to be k_{exp} = (1.4±0.2) × 10^{-11} and (5.4±3.0) × 10^{-13} cm^3 s^{-1}. Those values are smaller than for the second and third protonation in the $Mes_3Fe^-/R^{F3}OH$ series. The finding could be interpreted in such a way that the Br group exerts a slightly more deactivating effect onto the ferrate than $R^{F3}O$ which would be similar to the indirect effect of the X substituent in the Et_2ZnX^- (X = H, Et, OH, F, Cl) protonation wherein the less basic X caused a slower protonation of the Et moieties (cf. section 3.1.1.2).
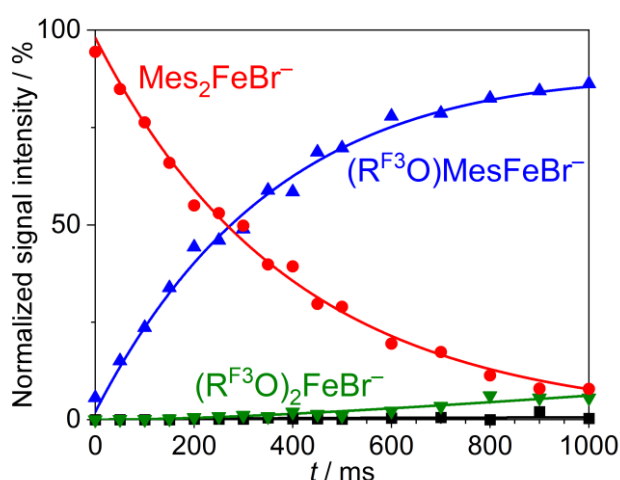
Figure 64: Kinetic measurement (MS^2) of the gas-phase reaction of mass-selected Mes_2FeBr^- with 2,2,2-trifluoroethanol ($R^{F3}OH$; $N_{substrate}/V$ = 1.7 × 10^{11} cm^{-3}).

3.2.2 Variation of the proton donor

For the protolysis of the trisarylferrate anions Ph_3Fe^-, the proton donor was changed from 2,2,2-trifluoroethanol ($R^{F3}OH$) to the less acidic 2,2-difluoroethanol ($R^{F2}OH$). Just as for the reaction with $R^{F3}OH$, three protonation reactions were observed in the protolysis series of Ph_3Fe^- by $R^{F2}OH$. First, Ph_3Fe^- reacted to ($R^{F2}O)FePh_2^-$ and benzene, which further reacted to ($R^{F2}O)_2FePh^-$ (and benzene). In the last step, ($R^{F2}O)_2FePh^-$ is converted into ($R^{F2}O)_3Fe^-$. The consumption of the reactant ion Ph_3Fe^- by $R^{F2}OH$ lasted approx. 4000 ms which is about four times longer than in the reaction with $R^{F3}OH$. Side reactions of Ph_3Fe^- with HCOOH and $R^{F3}OH$ as traces in the QIT were observed to minor extents (Figure 65). The kinetic measurements determined the bimolecular rate constants for the first, second and third protonation to be k_{exp} = (2.8±0.3) × 10^{-12}, (1.5±0.2) × 10^{-12} and (1.0±1.2) × 10^{-12} cm^3 s^{-1}, respectively. The rates of the proton-transfer steps decrease from the preceding to the subsequent one. The same trend was observed in the reaction of Ph_3Fe^- with $R^{F3}OH$. Even the ratio between the first and second protonation step is about the same (2:1).
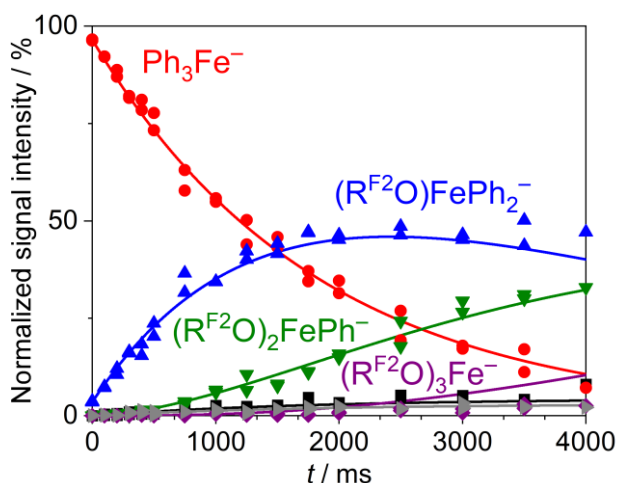
Figure 65: Kinetic measurement (MS^n) of the gas-phase reaction of mass-selected Ph$_3$Fe$^-$ with 2,2-difluoroethanol (R^{F2}OH; $N_{substrate}/V = 1.8 \times 10^{11}$ cm^{-3}).

Quantum-chemical calculations of the first and second proton-transfer reactions (S(Fe(+II)) = 2) were conducted by Amarasinghe, Shafique and Feldt (DLPNO-CCSD(T)/def2-TZVP//ωB97X-D3/def2-TZVP). Both reaction profiles are double-well potentials with the first protonation being more exothermic ($\Delta_rH_0 = -123$ vs. -109 kJ mol^{-1}) and featuring the lower central barrier ($\Delta H_0^\ddagger = -15$ vs. $+1$ kJ mol^{-1}). This is in contrast to the computations for Ph$_3$Fe$^-$/R^{F3}OH but matches the expected trend that the lower gas-phase acidity of the proton donor would raise the intrinsic barrier. Furthermore, the relative barrier heights agree with the relative experimental rate constants (Figure 66).
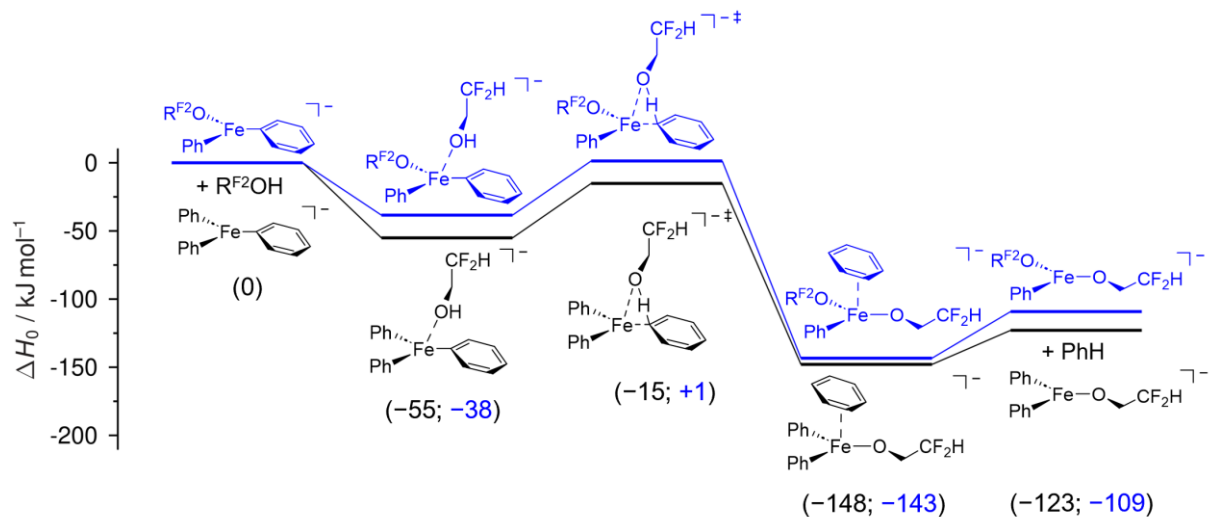
Figure 66: Reaction pathway for the phenyl protonation reaction of Ph$_3$Fe$^-$ (black) and (R^{F2}O)FePh$_2^-$ (blue) with 2,2-difluoroethanol (R^{F2}OH) as obtained from quantum-chemical calculations (DLPNO-CCSD(T)/def2-TZVP//ωB97X-D3/def2-TZVP). The calculations were carried out by Kosala N. Amarasinghe, Muhammad Shafique and Milica Feldt.

3.2.3 Comparison of experimental and theoretical rate constants

The aim of the Fe-MAN blind challenge is to evaluate the performance of different quantum-chemical methods by comparing predicted theoretical rate constants k_{theo} against their experimental references k_{exp}. From the kinetic measurements, only six were considered for the benchmarking challenge (Table 9). For Reaction 0, the participants were given the experimental rate constant and an estimate of the central barrier ($\Delta H_0^{\ddagger} = (30\pm4)$ kJ mol^{-1}) as a training set for their theoretical method. The reactions 1–5 were the test set.

Table 9: Protonation reactions of organoferrate anions by the fluorinated alcohols considered for the Fe-MAN challenge.

Reaction #	Reactant ion[a,b]	Proton donor[b]	k_{exp} / cm^3 s^{-1}
0	Ph_3Fe^-	$R^{F3}OH$	$(2.2\pm0.3) \times 10^{-11}$
1	$(R^{F3}O)FePh_2^-$	$R^{F3}OH$	$(9.1\pm1.4) \times 10^{-12}$
2	Ph_3Fe^-	$R^{F2}OH$	$(2.8\pm0.3) \times 10^{-12}$
3	$(R^{F2}O)FePh_2^-$	$R^{F2}OH$	$(1.5\pm0.3) \times 10^{-12}$
4	Mes_3Fe^-	$R^{F3}OH$	$(8.2\pm0.2) \times 10^{-13}$
5	$(R^{F3}O)FeMes_2^-$	$R^{F3}OH$	$(3.4\pm2.4) \times 10^{-11}$

[a] Ph = C_6H_5, Mes = $C_6H_2(CH_3)_3$, [b] $R^{F3}OH$: CF_3CH_2OH, $R^{F2}OH$: CF_2HCH_2OH.

The test reactions are well chosen as their rate constants k_{exp} span over two orders of magnitude (10^{-13} to 10^{-11} cm^3 s^{-1}) and are evenly distributed over that range. The order of the rate constants $k_{exp,i}$ (i: number of the reaction) is: $k_{exp,5} > k_{exp,0} > k_{exp,1} > k_{exp,2} > k_{exp,3} > k_{exp,4}$ (Figure 67). The chemical reasons for this order have been discussed in the previous sections.
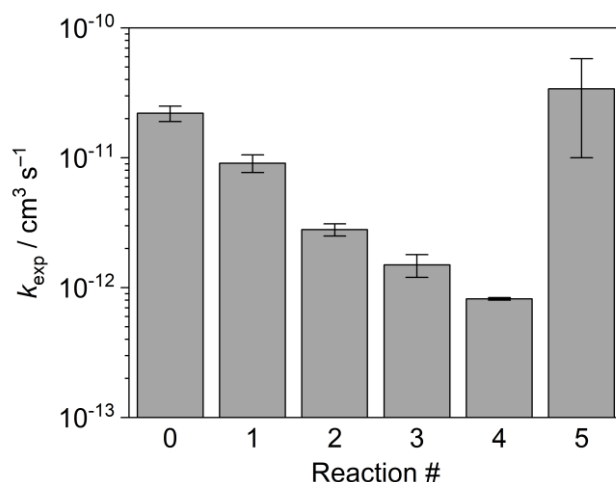
Figure 67: Experimental rate constants $k_{exp,i}$ for the reactions 0–5 of the Fe-MAN challenge.

3.2.3.1 Variation of the wave-function method

The first three data sets stem from the group of Milica Feldt. For all three, they searched and optimized the reactants, intermediates, transition structure and products of the Reactions 0–3 and 5 with the long-range corrected hybrid density functional ωB97X-D3 and def2-TZVP basis sets with the software package ORCA. Thereafter, they employed the local coupled-cluster methods DLPNO-CCSD(T), LUCCSD(T) and PNO-LCCSD(T)-F12 with def2-TZVP basis sets for the electronic single-point energy calculations. This approach offers the possibility to assess the performance of the three different wave-function methods.

The theoretical rate constants of the method DLPNO-CCSD(T) range from 1.3×10^{-16} cm^3 s^{-1} for Reaction 3 to 2.8×10^{-11} cm^3 s^{-1} for Reaction 0. The relative order of the rate constants does not agree well with the experimental reference. Only $k_{\text{theo},3}$ was correctly predicted to be smaller than $k_{\text{theo},2}$ (Figure 68).
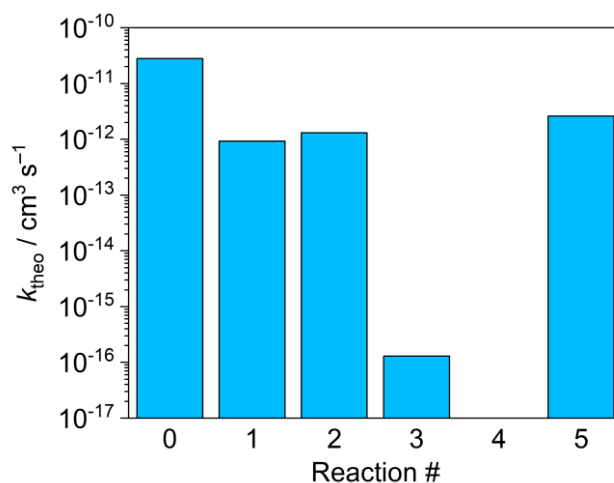
Figure 68: Theoretical rate constants k_{theo} as obtained from Master-equation calculations based on the stationary point calculations with the quantum-chemical methods DLPNO-CCSD(T)/def2-TZVP//ωB97X-D3/def2-TZVP by Amarasinghe, Shafique and Feldt.

In contrast, the order of the theoretical rate constants from the method LUCCSD(T) totally agree with the experimental one (Figure 69, left). Such qualitative agreement for all but one reaction was also achieved in the case of the PNO-LCCSD(T)-F12 calculations (Figure 69, right).
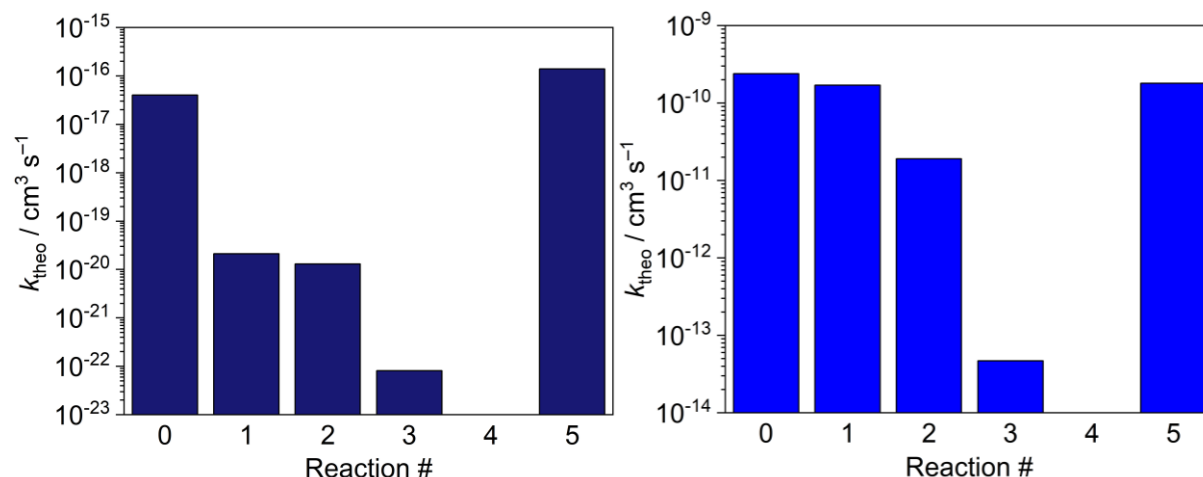
Figure 69: Theoretical rate constants k_{theo} as obtained from Master-equation calculations based on the stationary point calculations with the quantum-chemical methods LUCCSD(T)/def2-TZVP//ωB97X-D3/def2-TZVP (left) and PNO-LCCSD(T)-F12 (right) by Amarasinghe, Shafique and Feldt.

Next, the accuracy of the three wave-function methods was assessed quantitatively by correlating the theoretical rate constants k_{theo} against their experimental congeners k_{exp}. Evidently, the rate constants from LUCCSD(T) calculations are too small by several orders of magnitude. This corresponds to central barriers $\Delta H_0^{\ddagger}$ that were computed much too high. The agreement between experiment and theory for the methods DLPNO-CCSD(T) and PNO-LCCSD(T)-F12 is much better. Disregarding Reaction 3 (($R^{F2}O$)FePh$_2^-$/$R^{F2}OH$), the deviation is within factors of up to 13 and 19 for DLPNO-CCSD(T) and PNO-LCCSD(T)-

F12, respectively. Apparently, the DLPNO-CCSD(T) rate constants underestimate (overestimate) the rate constants (central barriers). This is in line with most of the organozincate results where the theoretical rate constants were almost always predicted to be smaller than the measured ones. In contrast, the PNO-LCCSD(T)-F12 computations overestimate (underestimate) the rate constants (central barriers). Both findings suggest that contributions to the correlation energy are neglected as a consequence of the respective localization schemes. Better theoretical predictions could be obtained by adjusting these schemes, although this would come at higher computational costs (Figure 70).
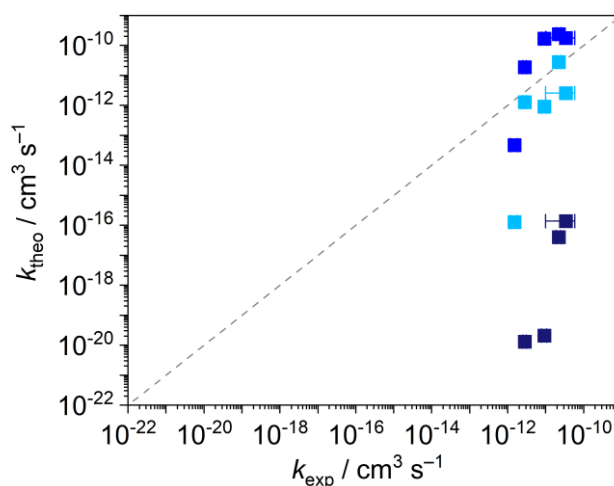
Figure 70: Correlation of the theoretical rate constants k_{theo} with the experimental ones k_{exp} for the Reactions 0–3 and 5 for the quantum-chemical methods DLPNO-CCSD(T) (bright blue), LUCCSD(T) (darkblue) and PNO-LCCSD(T)-F12 (blue) by Amarasinghe, Shafique and Feldt. The gray dashed line corresponds to ideal agreement between experiment and theory.

3.2.3.2 Influence of the kinetic model

Another data set was provided by Luxuan Guo and Jeremy N. Harvey who computed the reaction pathways with the DFT method B3LYP-D3BJ and def2-SVP or def2-TZVPD basis sets. They submitted rate constants that were calculated using a classical canonical transition state theory (TST) model. Therein, multiple conformers for the transition structure were considered and all their contributions taken into account to obtain the overall rate constant. Vibrational frequencies below 50 cm^{-1} were set to the afore-mentioned value. The capture rate constants were assumed to be 2.0×10^{-9} cm^3 s^{-1} for all reactions. With the same approximations, microcanonical rate constants were also calculated with the Master-equation solver MESMER based on their computed structures and energies. This design allows for the evaluation of the applied kinetic model (canonical vs. microcanonical).

Neither within the canonical nor the microcanonical the order of the rate constants was predicted correctly indicating that the underlying quantum-chemical computations did not succeed in the calculation of the correct relative barrier heights. Moreover, it is apparent that the theoretical rate constants k_{theo} are always lower than the canonical ones by about about one order of magnitude (Figure 71).
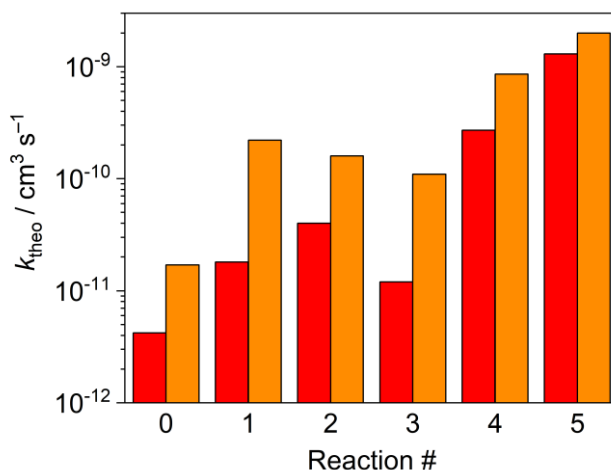
Figure 71:   Theoretical rate constants k_{theo} for the Reactions 0–5 as obtained from a microcanonical (red) and canonical (orange) model based on the B3LYP-D3BJ/def2-TZVPD structures and energies by Guo and Harvey.

The quantitative comparison of the experimental rate constants k_{exp} to the theoretical ones k_{theo} as obtained from the canonical and microcanonical kinetic model shows that the overall agreement is better for the microcanonical model than for the canonical one. Disregarding Reaction 4, the maximum deviations amount to 39 and 72 within the microcanonical and canonical model, respectively, which is far from chemical accuracy ($\Delta\Delta H_0^{\ddagger} < 4$ kJ mol^{-1}; deviating factor < 5). The huge mismatch for Reaction 4 hints to significant errors in the calculation of its stationary points (Figure 72).
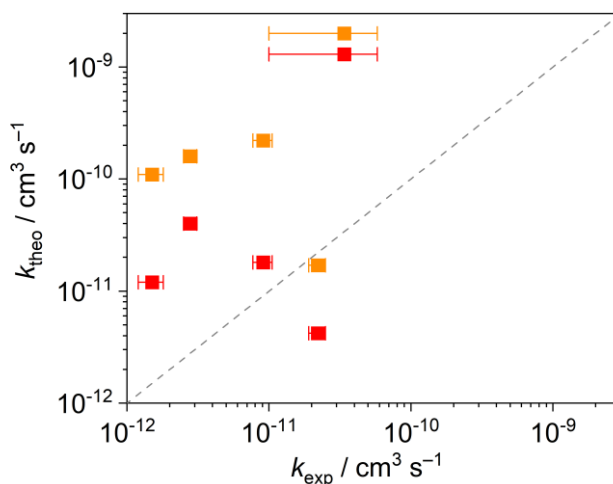
Figure 72:   Correlation of the theoretical rate constants k_{theo} with the experimental ones k_{exp} for the Reactions 0–5 for the microcanonical (red) and canonical (orange) model based on the computations by Guo and Harvey. The gray dashed line corresponds to ideal agreement between experiment and theory.

The overall agreement between experiment and theory appears to be better for the microcanonical than for the canonical model. However, at this point it is unclear whether the better agreement results from the description of the reaction ensemble as microcanonical or canonical, respectively, or from the consideration of multiple conformers of the transition structure as in the canonical model.

Table 10: Experimental and theoretical rate constants, k_{exp} and k_{theo}, for the Reactions 0–5 of the Fe-MAN challenge.

Reaction #	Experiment k_{exp} / cm³ s⁻¹	DLPNO-CCSD(T)[a]	LU-CCSD(T)[a]	PNO-LCCSD(T)[a] k_{theo} / cm³ s⁻¹	B3LYP [b]	B3LYP canonical[c]
0	$(2.2\pm0.3) \times 10^{-11}$	2.8×10^{-11}	4.0×10^{-17}	2.4×10^{-10}	4.2×10^{-12}	1.7×10^{-11}
1	$(9.1\pm1.4) \times 10^{-12}$	9.2×10^{-13}	2.1×10^{-20}	1.7×10^{-10}	1.8×10^{-11}	2.2×10^{-10}
2	$(2.8\pm0.3) \times 10^{-12}$	1.3×10^{-12}	1.3×10^{-20}	1.9×10^{-11}	4.0×10^{-11}	1.6×10^{-10}
3	$(1.5\pm0.3) \times 10^{-12}$	1.3×10^{-16}	8.1×10^{-23}	4.7×10^{-14}	1.2×10^{-11}	1.1×10^{-10}
4	$(8.2\pm0.2) \times 10^{-13}$	–	–	–	2.7×10^{-10}	8.6×10^{-10}
5	$(3.4\pm2.4) \times 10^{-11}$	2.6×10^{-12}	1.4×10^{-16}	1.8×10^{-10}	1.3×10^{-09}	2.0×10^{-9}

[a] Stationary-point calculations by Amarasinghe, Shafique and Feldt were used for the microcanonical Master-equation calculations. [b] Stationary-point calculations by Guo and Harvey were used for the microcanonical Master-equation calculations. [c] Guo and Harvey provided rate constants calculated with canonical TST.

3.3 Synopsis

3.3.1 Protonation reactions of organometallics

The gas-phase protolysis of organometallic ions features distinct properties. The aim of this section is to underline similarities and differences between the intrinsic reactivities of gaseous metalates depending on their structure. The following considerations are based on the previous experimental and theoretical results about the protonation of anionic residues in the terminal positions of the organozincate species R_3Zn^- (R = alkyl, aryl) and Et_2ZnX^- (X = H, Et, OH, F, Cl) as well as the organoferrate species Ar_3Fe^- (Ar = Ph, Mes).

3.3.1.1 The typical reaction pathway

The typical pathway for the protonation of such organometallic anions in the gas phase is a double-well potential in terms of the enthalpy at 0 K, ΔH_0, which is the most suitable descriptor for the energetics of reactions under low-pressure conditions as they are given in 3D quadrupole ion trap (QIT) mass spectrometers. Due to the lack of thermalization of the species, the reaction ensemble is microcanonical and thus, the Gibbs energy $\Delta G_{(310)}$ is not adequate (cf. section 3.2.3.2).[128] The double-well potential consists of five stationary points which are connected by three reaction steps (cf. Figure 4). The reaction pathway thus agrees qualitatively with the one for gas-phase substitution reactions (S_N2).[44,70] In a way, the proton-transfer reactions herein can be described as the linear combination of the substitution reaction (changing the basic residue for the anion of the acid) and the simultaneous proton-transfer step (from the proton donor to the basic site of the organometallic ion).[55]

First, the reactants, i.e. the ionic organometallic species as the proton acceptor and the polar proton donor (e.g. an alcohol ROH), form the encounter complex which is stabilized by intermolecular interactions, such as ion-dipole interactions or hydrogen bonds. This reaction step is bimolecular and can be described by the capture theory according to Su and Chesnavich.[122–124] Second, the actual proton transfer takes place from the proton donor to the basic site of one residue of the organometallic species. So, the pre-reactive complex progresses to the product complex via the four-membered (or six-membered) transition structure (TS) which features one imaginary frequency that largely corresponds to the motion of the protic hydrogen between the donor and acceptor atom. This unimolecular process is associated with the central barrier $\Delta H_0^{\ddagger}$ and can be modelled kinetically with the statistical rate theory by Rice, Ramsperger, Kassel and Marcus (RRKM).[34,52,54–56] Third, the product complex dissociates into its components, the protolyzed organometalate and the protonated form of the formerly basic residue. Therein, the energy of the intermolecular interactions is overcome (cf. section 3.1.1.1). In most examples in this thesis, the overall reaction is exothermic ($\Delta_r H_0 < 0$).

The generic form of the pathway for the protonation of organometallics was found to be independent of the constituency of the organometallic ions.

3.3.1.2 Barriers associated with the proton transfer

The height of the central barrier, $\Delta H_0^{\ddagger}$, dictates the dynamics of such gas-phase protonation reactions. For low activation barriers, the kinetics are governed by the capture rate of the reactants. In contrast, increasingly high barrier heights will slow down the reaction more and more up to an extent where it does not take place effectively anymore. The central

barrier is a measure of the structure of the TS, which, in turn, reflects onto the intrinsic reactivity of the organometallic ion under scrutiny. Over the course of this dissertation, two key schemes about the barrier heights were found.

The first finding is that the activation barriers (and not the reaction energies) of the proton-transfer reactions decide on the chemoselectivity of the protonation when different kinds of protonation sites are involved. For this finding, the classification by Eigen about normal and non-normal acids and bases turned out to be well applicable. Eigen defined normal acids (bases) as proton donors (acceptors) in whose reactions the proton is transferred instantaneously once the donor and acceptor are in sufficient spatial proximity. Accordingly, their reaction rates are close to the diffusion limit in solution or the collision rate in the gas phase. Normal acids feature $-OH$, $-NH_2$ or $-SH$ functionalities, i.e. protic hydrogen atoms and free electron pairs at the vicinal heteroatom. As a consequence, hydrogen bonds between the proton donor and acceptor form which stabilize the pre-reactive complex and the TS. The TS can even be described as a triple ion in the form $[X^-\cdots H^+\cdots Y^-]^{\ddagger}$ (X, Y = O, N, S) where the negative charges of the donating site Y and accepting site X are already localized in the free electron pairs. As the result of the stabilization by the hydrogen bonds and the low reorganization energy, the activation barriers in the proton-transfer reactions of normal acids and bases are usually (very) low.
The opposite holds true for C–H acids and C bases which are considered non-normal. This originates from the apolar nature of the C–H bond. In the case of proton donation, stabilizing hydrogen bonds cannot be formed. And if a C base accepts a proton, the negative charge which was formerly localized in a free electron pair needs to be delocalized between the carbon and hydrogen atom which requires high reorganization energy. As a result, the intrinsic barrier for the protonation (deprotonation) of C bases (C–H acids) are usually high and the intrinsic rate constants (very) low.

These described reactivities were best observed in the protonation of the organozincate anions Et_2ZnX^- (X = H, Et, OH) by 2,2,2-trifluoroethanol ($R^{F3}OH$) (cf. section 3.1.1.2). There, the protonation of the H and OH sites occurred at the collision rate limit, whereas the ethyl protonation was much slower. This is surprising given that the ethyl moiety is the most basic moiety. The experimental findings aligned with quantum-chemical calculations about the central barrier $\Delta H_0^{\ddagger}$ being higher for X = Et than for X = H, OH. Moreover, the triple-ion character of the transition structure for the proton transfer to Eigen-normal bases was illustrated by the shorter $(R^{F3}O)H-X(ZnEt_2^-)$ bond length for X = H, OH.

The second key finding is that within one class of protonation site, the reaction energy $\Delta_r H_0$ scales proportionally with the central barrier $\Delta H_0^{\ddagger}$. The dependence of the central barrier $\Delta H_0^{\ddagger}$ on the reaction energy $\Delta_r H_0$ was studied in two ways.
First, the reaction energy $\Delta_r H_0$ was adjusted by changing the *para*-substituents X of the trisarylzincate anion $Ar^X ZnPh_2^-$ (X = OMe, Me, H, F, Cl). Again, a linear correlation between $\Delta H_0^{\ddagger}$ and $\Delta_r H_0$ was found. Interestingly though, this time the slope m for the correlation was different ($m = +0.19\pm0.04$) (cf. section 3.1.1.1) than for the variation of the proton donor $R^{Fn}OH$ in the Ph_3Zn^- protonation ($m = +0.70\pm0.09$). Apparently, the proton-transfer reaction is more sensitive towards changing the donor than the acceptor site. The observation suggests an "imbalance" of the TS as conceptualized by Jencks[28] and Bernasconi[32,38,39] meaning that the proton transfer and the electronic reorganization are not concurrent but the electronic rearrangement lags behind the proton transfer. This is in line with the proposed triple-ion picture of the TS because the proton is transferred first transforming

X$^-$⋯H–Y into [X$^-$H$^+$⋯Y$^-$]‡ and only afterwards the charge is relocated giving X–H⋯Y$^-$ (X = (Ar$_2$Zn)Ar; Y = R^{F3}O). The situation is depicted in the More O'Ferrall–Jencks diagram in Figure 73 (red curve).
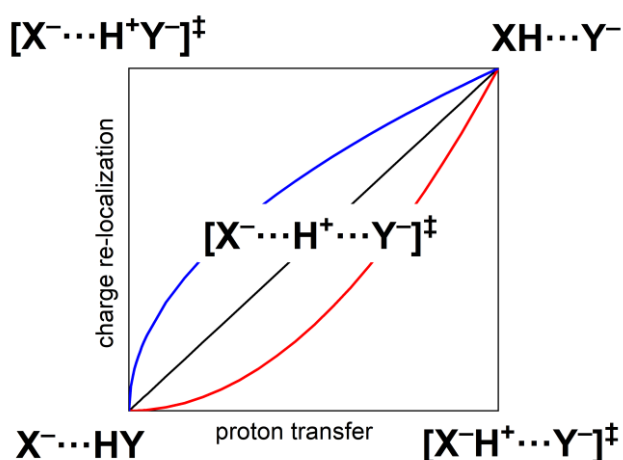
Figure 73: Schematic More O'Ferrall–Jencks diagram for the proton transfer-reaction from the donating site Y to the accepting site X. The transfer of the proton and the charge re-localization are not concurrent (black line) but the charge re-localization lags behind the proton transfer (red curve) or vice versa (blue curve).

Second, the gas-phase acidity of the proton donor was varied. For that purpose, the fluorinated alcohols R^{Fn}OH (n = 0–3) were used for the protolysis of Me$_3$Zn$^-$ and Ph$_3$Zn$^-$. In both cases, the central barrier increased linearly with the reduction of the exothermicity. This linear energy relationship matches the expectations from the Marcus theory within the so-called normal regime (cf. section 3.1.2.1).

3.3.2 Theory vs. experiment benchmarking

The evaluation of the performance of various computational methods against experimental reference data was another key element of this dissertation. This theory-vs.-experiment benchmarking poses the core of the RTG BENCh and will thus be elaborated on in this section. To achieve agreement and disagreement for the right reasons, the possible shortcomings in both the experimental and theoretical determination of the rate constants for the protonation reactions of organometallic ions will be assessed critically. Then, the experimental and theoretical rate constants, k_{exp} and k_{theo}, will be compared quantitatively for a selection of the organozincate and organoferrate systems and inferences will be drawn from the agreement or disagreement.

The experimental rate constants k_{exp} were determined from gas-phase ion-molecule reactions in a 3D quadrupole ion trap (QIT) in which the substrate (proton donor) was introduced via a home-built gas-mixing and inlet apparatus. The reactions took place with an excess of the substrate under pseudo-first order conditions at the concentration $N_{substrate}/V$ and the temperature T = (310±20) K. The experimental uncertainty of the rate constants arises from statistical and systematic errors.

To account for the statistical deviations, each kinetic experiment was performed in two independent measurements and the 95% confidence interval (2σ) was given as the experimental uncertainty throughout this thesis. Typically, this statistical contribution was below 30% of the determined value.

Moreover, a number of systematic sources for errors are conceivable. The most important one is the concentration of the substrate within the QIT due to the difficulties of determining absolute pressures. This error corresponds to an absolute deviation in the rate constants of ±30%.[101] Additionally, the reaction temperature T is not exactly known for the used mass spectrometer and only estimated from a literature-known value. However, it is very unlikely that the actual temperature does not lie within the range of 290 to 330 K because the instrument thermalizes with the ambient temperature of the room it is operated in. Other possible systematic errors could emerge from the data analysis. The neglecting of minor species throughout the kinetic measurements could be a possible shortcoming, too, although it was found that species below 5% relative signal intensity do not change the normalized intensities of the main species significantly. The conceived reaction network, which was applied for the kinetic fitting of the time-species profiles, could also render systematic errors but they would become obvious in the obtained fit of the data.

Even in the worst case, the uncertainty of the experimental rate constants will most likely be within a factor of 2 (estimate by the author).

The theoretical rate constants k_{theo} for the protonation reactions of the organometallic species were computed in two steps. First, quantum-chemical calculations were conducted to obtain the structures and energies of the species along the reaction pathway. Second, Master-equation calculations were performed based on the stationary-point data (rotational constants, vibrational frequencies, enthalpies at 0 K) to simulate the kinetics of the reaction. The rate constants were then extracted from the resulting time-species profiles. Systematic errors may occur in both steps.

The search and optimization of the calculated structures could potentially be flawed in that the found structures do not correspond to the minimum-energy geometries. This is unlikely if the structure search and optimization is carried out carefully. It is also possible that the reaction does not proceed through one single conformer of the transition structure but many. In this case, some kind of conformer averaging would be necessary. For the theoretical rate constants reported in this thesis no such averaging was performed. Further, the rotational constants and vibrational frequencies from the computed structures could be inaccurate which would alter the theoretical rate constants. However, tests found that k_{theo} is not very sensitive to the rotational constants and vibrational frequencies.

Furthermore, the computed energies of the stationary points could be over- or underestimated. In these cases, k_{theo} could change drastically. It was found that the resulting theoretical rate constants are virtually insensitive towards the energy of the pre-reactive complex but highly sensitive towards the energy of the TS, i.e. the central barrier $\Delta H_0^{\ddagger}$ and thus, k_{theo} scales exponentially with $\Delta H_0^{\ddagger}$. As such, overestimating (underestimating) the energy of the TS will lead to the significant underestimation (overestimation) of the theoretical rate constant. For instance, energy differences of 4 and 8 kJ mol^{-1} correspond to the change of k_{theo} by factors of 5 and more than 20, respectively.

Other sources of errors in the determination of the theoretical rate constants stem from the kinetic simulation of the reaction. The formation of the pre-reactive complex is kinetically modelled by the collision rates of the ion and the polar substrate according to the capture theory by Su and Chesnavich but this theory systematically underestimates the collision rates because the ions are treated as point charges with no spatial extent. This error may be negligible for small organometallic ions such as Me$_3$Zn$^-$ but will become more relevant for large ions such as Ph$_3$Zn$^-$ or Mes$_3$Fe$^-$. Moreover, in this thesis theoretical dipole

moments and polarizability volumes for the proton donors were used. If these were inaccurate, they would affect the obtained capture rates. For low reaction barriers, the kinetics are dominated by the encountering of the reactants. For such cases, it was found that the k_{theo} is about 30% smaller than the experimental value. For high central barriers, in contrast, the influence of the capture rate onto k_{theo} is rather small because the reaction kinetics are governed by the proton-transfer process. Another error might come from the simplification of the reaction scheme. For the kinetic simulations in this thesis, the dissociation of the product complex into the products was neglected, i.e. once the pre-reactive complex is formed it directly reacts to the products via the TS. However, this assumption is reasonable. As long as the reaction is sufficiently exothermic, $\Delta H_0^\ddagger$ will be higher than the energy associated with the dissociation and thus, the proton transfer is the rate-determining step. In addition, quantum effects, such as proton tunneling, were not accounted for in the kinetic model but are more and more important for high central barriers around or higher than the entry energy. Without proton tunneling, the rate constants are underestimated. Eventually, the uncertainty of the temperature $T = (310\pm20)$ K in the kinetic experiment is also present in the theoretical simulation. As both the capture rate and the reaction efficiency for the proton transfer are temperature-dependent, k_{theo} is also a function of T. Then, k_{theo} could be over- or underestimated by up to 30% dependent from the height of the central barrier. Disregarding the effect of $\Delta H_0^\ddagger$ onto k_{theo}, the influence of the other error sources could add up to a maximum uncertainty of a factor of 2 (estimate by the author).

The best possible agreement between k_{exp} and k_{theo} for the methodology of this thesis is estimated to be within a factor of 3 which corresponds to an energy difference between the computed and "real" central barrier, $\Delta\Delta H_0^\ddagger$, of 3 kJ mol^{-1}. Every agreement within a factor of 5 can be considered to be excellent as it is chemically accurate ($\Delta\Delta H_0^\ddagger \leq 4$ kJ mol^{-1}). If the experimental and theoretical rate constants deviate by less than a factor of 10 ($\Delta\Delta H_0^\ddagger \leq 6$ kJ mol^{-1}), the agreement can be deemed to be still sufficiently good.

With the knowing of the limitations of the applied methodology, the experimental and theoretical rate constants, k_{exp} and k_{theo}, can be compared quantitatively for selected protolysis reactions of organozincate and organoferrate anions. As the calculated barrier height $\Delta H_0^\ddagger$ plays the decisive role, the comparison allows for the assessment of the performance of the theoretical method for the calculation of the electronic singe-point energies in specific and the quantum-chemical calculations in general.

For the protonation of the organozincate anions, the agreement between experiment and theory is found to be overall excellent in a large regime spanning from rate constants of 10^{-15} to 10^{-9} cm^3 s^{-1}. For 16 out of 21 systems, k_{exp} and k_{theo} agree within a factor of 5. For three more data points the deviation between the experimental and theoretical rate constants is within one order of magnitude. Only two systems feature mismatches with deviating factors larger than 10. Apparently, DLPNO-CCSD(T) is not only an excellent method to compute reaction energies for closed-shell organic and organometallic systems,[147−149] but also to calculate the reaction barriers for such systems.
Interestingly, the theoretical rate constants are underestimated in 19 out 21 cases independent of the magnitude of the rate constant. This suggests that the quantum-chemical calculations with the method DLPNO-CCSD(T)/cc-pV[T;Q]Z//ωB97X-D3/def2-TZVP slightly overestimate the height of the central barrier $\Delta H_0^\ddagger$ (Figure 74, left).

The agreement between experiment and theory is poorer for the organoferrate anions. 7 out of 16 systems feature deviations between k_{exp} and k_{theo} that are larger than a factor of 10. The agreement is within one order of magnitude for five more systems and only 4 of 16 theoretical rate constants agree with their experimental congener within chemical accuracy. The quantum-chemical methods B3LYP-D3BJ/def2-TZVPD/B3LYP-D3BJ/def2-SVP and PNO-LCCSD(T)-F12/def2-TZVP//ωB97X-D3/def2-TZVP appear to underestimate the activation barrier whereas the method DLPNO-CCSD(T)/def2-TZVP//ωB97X-D3/def2-TZVP overestimates it (Figure 74, right).
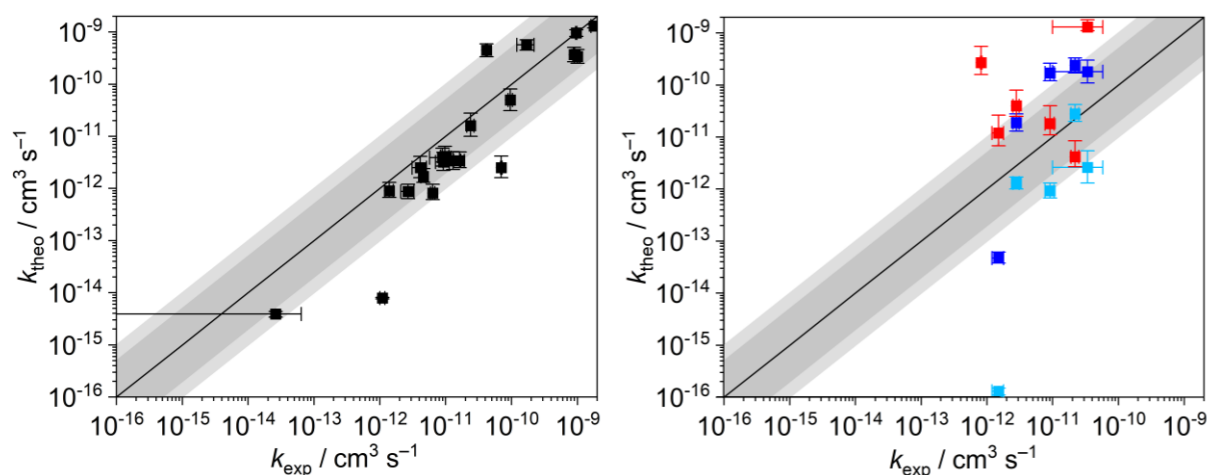
Figure 74: Comparison of the experimental and theoretical rate constants, k_{exp} and k_{theo}, for the protonation of organozincate species (left) and organoferrate species (right). The solid black line corresponds to ideal agreement between experiment and theory, the dark and bright gray area to an agreement within factors of 5 and 10, respectively. The theoretical rate constants for the organozincates (black squares) were computed based on DLPNO-CCSD(T)/cc-pV[T;Q]Z//ωB97X-D3/def2-TZVP calculations. The theoretical rate constants for the organoferrate anions were calculated based on the stationary points from DLPNO-CCSD(T)/def2-TZVP//ωB97X-D3/def2-TZVP (bright blue squares), PNO-LCCSD(T)-F12/def2-TZVP//ωB97X-D3/def2-TZVP (blue squares) and B3LYP-D3BJ/def-TZVPD//B3LYP-D3BJ/def2-SVP (red squares) calculations, respectively.

The findings for the organozincate systems demonstrate that methodology of this dissertation is well suited to investigate the barriers of protonation reactions of organometallics *qualitatively* and *quantitatively*. Their rate constants can be determined experimentally and calculated theoretically with high accuracy for closed-shell organometallic systems. In contrast, the rather poor agreement for the organoferrate anions suggests that current quantum-chemical methods are still far from achieving chemical accuracy and need to be further improved when used for open-shell organometallics. Benchmarking studies are essential in this endeavor and experimental reference data is required for their successful realization.

4   Conclusions and outlook

The aim of this dissertation was to apply the concepts and methods of physical organic chemistry to organometallic species and assess their intrinsic reactivity towards protonation. For this purpose, the activation barriers associated with the proton-transfer reactions of such organometallics were studied. The kinetics of the protonation reactions was investigated both experimentally and theoretically. In the experiment, gaseous organometallic species were prepared by electrospray ionization (ESI) and subsequently subjected to ion-molecule reactions with proton donors in a 3D quadrupole ion trap (QIT). In theory, kinetic simulations of these reactions were performed based on high-level quantum-chemical calculations. The interplay of experiment and theory in general and the comparison of experimental and theoretical rate constants in particular revealed new insights into the protonation reactions and the intrinsic properties of organometalate anions in the gas phase.

4.1   Protonation of organozincate anions

At the instance of various organozincate anions, the effects that different basic sites exert onto the intrinsic reactivity of the organometallic species were studied. In most cases, 2,2,2-trifluoroethanol ($R^{F3}OH$) was used as the proton donor. Experiments found that the protonation proceeded rather slowly when the proton acceptor featured C bases as the accepting sites. For the reaction of the trisphenylzincate anion Ph_3Zn^- with $R^{F3}OH$ to $(R^{F3}O)ZnPh_2^-$ and PhH, the reaction efficiency amounted to less than 2% indicating significant barriers associated with the protonation. The proton transfer to the trisalkylzincate species R_3Zn^- (R = Me, Et) giving $(R^{F3}O)ZnR_2^-$ occurred somewhat faster although it was still well below the collision-rate limit. The observations illustrate the "non-normal" character of carbon bases as it had previously been described by Eigen. Because C bases (and C–H acids) feature less localized negative charges and cannot form hydrogen bonds that mediate the proton transfer between donor and acceptor, the intrinsic barriers for their protonation (deprotonation) are much higher and thus, their proton-transfer reactions will be slow.

Quantum-chemical calculations of the reactions informed about the typical reaction pathway which is a double-well potential in terms of the enthalpy at 0 K, ΔH_0, which best represents the reaction energetics under low-pressure conditions for microcanonical ensembles. Most reactions featured reaction energies of $\Delta_r H_0 < -100$ kJ mol^{-1} and central barriers of $\Delta H_0^{\ddagger} < -10$ kJ mol^{-1}. In the Hammett study for the reaction of $Ar^X ZnPh_2^-$ ($Ar^X = p$-X-C_6H_4; X = OMe, Me, H, F, Cl) with $R^{F3}OH$, a Brønsted-type LFER between $\Delta H_0^{\ddagger}$ and $\Delta_r H_0$ was found.

Kinetic simulations, in which the encounter of the reactants was modelled with the capture theory by Su and Chesnavich and the proton transfer with classical RRKM theory, achieved excellent agreement with the experiments which rendered strong confidence into the full qualitative and quantitative understanding of the systems.

The influence of hydride, hydroxide, fluoride and chloride as the accepting site onto the intrinsic reactivity of the organozincate species Et_2ZnX^- (X = H, OH, F, Cl) towards 2,2,2-trifluoroethanol ($R^{F3}OH$) was investigated. Surprisingly, in most of these systems the protonation of the X site was favored over that of the Et moieties despite its more favorable

thermochemistry. For the so-called Eigen normal base with X = OH, the protonation proceeded with unity efficiency because the negative charge is largely localized in the anionic substituents and hydrogen bonds in the pre-reactive complex pre-organize and thereby facilitate the actual proton transfer. In contrast, the protonation of the fluoride moiety was much slower and the chloride site was not protonated at all. Despite their "normal" nature, their protonation is barely exothermic or even endothermic and so, unfavorable reaction energy prevents the protolysis to take place. In addition to this direct substituent effect, an indirect one was determined. With the decreasing gas-phase basicity of X^-, the protonation of the ethyl moieties in Et_2ZnX^- is more and more hampered which is probably brought about by the increased Lewis acidity of the metal center. The indirect effect could be described in terms of a Brønsted-type relationships between central barrier $\Delta H_0^{\ddagger}$ and the reaction energy $\Delta_r H_0$ as well as an Eigen-type correlation between the logarithmic protonation rate constant k_{exp} and the gas-phase acidity ΔG_{acid} of XH (X = H, OH, F, Cl).

In order to conclude the studies of such substituent effects, additional experiments and calculations should be performed. First, the protolysis reaction of an organozincate Et_2ZnX^- with a N base (e.g. X = NH_2, NHR or NR_2; R: alkyl) should be measured experimentally and calculated theoretically. In preliminary experiments, the preparation of such species was not possible because the desired anion $Et_2Zn(NMe_2)^-$ was presumably hydrolyzed in the ion source giving $Et_2Zn(OH)^-$. One possibility might be to switch from Et_2ZnX^- to Ph_2ZnX^- with overall higher protonation barriers. Second, the ion-molecule reaction of $Et_2Zn(CH_3)^-$ (instead of Et_3Zn^-) with $R^{F3}OH$ should be carried out as X = CH_3 is more comparable to X = H, NH_2, OH, F. At last, kinetic isotope effects for the reaction of Et_2ZnX^- (X = H, D) with $R^{F3}OH$ could be probed. Et_2ZnD^- can be readily prepared via the gas-phase β-hydride elimination of $Et_2Zn(C_4D_9)^-$.

Furthermore, the dependence of the reaction kinetics on the reaction energy was demonstrated by changing the proton donor 2,2,2-trifluoroethanol ($R^{F3}OH$) for 2,2-difluoro-($R^{F2}OH$) and 2-fluoroethanol ($R^{F2}OH$) in the protolysis of Me_3Zn^- and Ph_3Zn^-. In both cases, the kinetics and thermochemistry obeyed a Brønsted-type relation where the height of the protonation barrier $\Delta H_0^{\ddagger}$ scaled linearly with the exothermicity $\Delta_r H_0$. For Ph_3Zn^-, indications for a so-called "imbalance" of the transition structure were found which can be rationalized in a More O'Ferrall–Jencks picture: The re-localization of the negative charge (electronic change) lags behind the transfer of H^+ (geometric change). Here, more sophisticated quantum-chemical calculations, in which the proton is treated quantum-mechanically, too, could shed light onto the quantum effects at play.

In the reaction of Me_3Zn^- with HCOOH, the kinetic measurement showed an extraordinary complexity which rendered the analysis of the experimental data difficult. Therefore, the data analysis should be enhanced. In a collaboration with the Proppe group, the software package iKiNetX will be developed which will automate the data analysis and allow for the more detailed quantification of the experimental uncertainty. Especially, iKiNetX will provide an opportunity to evaluate the relevance of single reaction steps in the reaction network that was applied to the fitting of the experimental data and so, opens up the possibility to reduce a large reaction network to the most essential parts that are sufficient to explain the observed reactions.

For most of the organozincate systems, remarkably good agreement within the limits of chemical accuracy was found between experimental and theoretical rate constants. Thus,

the combination of ion-molecule experiments with quantum-chemical calculations and kinetic simulations proved to be suitable for the investigation of the barriers of protonation reactions of organometallics as well as the benchmarking of theoretical methods against experimental reference data.

4.2   Protonation of organoferrate anions

The reaction of the organoferrate anions Ar_3Fe^- (Ar = Ph, Mes) was found to be similar to that of the organozincate species. The protonation by 2,2,2-trifluoroethanol ($R^{F3}OH$) or 2,2-difluoroethanol ($R^{F2}OH$) yielded products of the type $(R'O)FeAr_2^-$ plus ArH. Quantum-chemical calculations showed that the reaction pathway is again a double-well potential with high exothermicities $\Delta_r H_0 < 0$ and significant central barriers $\Delta H_0^{\ddagger}$ which drastically slow down the reaction rates. In contrast to the trisarylzincates, however, the complete protolysis with all three consecutive protonation reactions was observed for the trisarylferrate anions. This illustrates the effect of metal center onto the intrinsic reactivity of the species. The subsequent protonation reactions were found to be slower than their preceding ones which can be rationalized via the deactivating effect of the alkoxide substituents. The hypothesis was also corroborated by the protolysis of Mes_2FeBr^-. The substituent effects were comparable to that of the X residues in the zincate systems $Et_2ZnX^-/R^{F3}OH$. Moreover, steric influences were demonstrated by the gas-phase reaction of Mes_3Fe^- with $R^{F3}OH$ where the second reaction occurred much faster than the first one because the access of the proton donor to the basic site was less hindered in $(R^{F3}O)FeMes_2^-$.

The experimental bimolecular rate constants for the protonation of the organoferrate anions served as the reference data for the BENCh blind challenge "Ferrates – Microkinetic Assessment of Numerical Quantum Chemistry" (Fe-MAN). The project aimed for the evaluation of the predictive performance of different quantum-chemical methods. Although more advanced wave-function methods for the calculation of the electronic single-point energies were slightly more accurate than DFT functionals, the overall agreement between experiment and theory was poorer than for the organozincate anions. Here, the need for such experiment-theory benchmarking studies became evident which allow for the systematic improvement of quantum-chemical methods to achieve the desired chemical accuracy even for demanding systems at justifiable computational costs. These enhancements are up to theoretical chemists.

Furthermore, at the example of $Ph_3Fe^-/R^{F3}OH$ it was shown that the ion-molecule reactions did indeed proceed under pseudo-first order conditions which supports the suitability of the chosen instrumentation.

In the future, the experiments could be extended by temperature-dependent kinetic measurements. By cooling (heating) the 3D quadrupole ion trap below (above) room temperature, the ion-molecule reactions could be carried out as a function of the temperature. Thereby, the different influences of ion-molecule reactions could be elucidated. For instance, the role of the capture rate or the entropic contributions to the proton transfer could be resolved. Preliminary tests of such an adaptation of the device turned out tedious and challenging although they rendered confidence in the general feasibility of such an endeavor.

This dissertation about the barriers of protonation reactions of organometallics was successful in that the applicability of the methodology was validated, new insights into the proton-transfer reactions of organometallics and their intrinsic reactivities were found and, lastly, experimental reference data for the assessment of computational methods was generated for future benchmarking studies.

5 Experimental and computational details

5.1 Experimental details

5.1.1 Sample preparation

The sample solution for the mass-spectrometric measurements were routinely prepared under inert-gas conditions using standard Schlenk techniques. Argon (99.999%) was used as the inert gas. Tetrahydrofuran (THF) as the solvent was dried over sodium/benzophenone and freshly distilled for each experimental day. All other chemicals were used as purchased without further purification. Most chemicals were obtained from Sigma Aldrich (Germany).

5.1.1.1 Preparation of organozincate species

Trisarylzincate anions: A Schlenk flask (10 mL) was charged with $ZnCl_2$ (0.027 g, 0.20 mmol), repeatedly evacuated under heating (523 K) and flushed with Ar. After cooling to room temperature, THF (10 mL) was added and the mixture was stirred for 1 h at room temperature. The clear solution was cooled to −195 K and treated with PhLi and a Grignard reagents Ar^XMgBr (Ar^X: p-X-C_6H_4, X = NMe_2, OMe, Me, F, Cl) (Table 11). Subsequently, the solution (20 mM) was allowed to warm up to 273 K under stirring for 10 min and then used for the mass-spectrometric measurement wherein it slowly warmed up to room temperature.

Table 11: Preparations of the sample solutions containing the denoted trisarylzincate anions.

Species	Metal source	Transmetalation reagent(s)	Temperature / K
Ph_3Zn^-	$ZnCl_2$	PhLi (4 equiv.)	273
$Ar^{NMe2}ZnPh_2^-$	$ZnCl_2$	PhLi (2 equiv.) + p-NMe_2-C_6H_4MgBr (2 equiv.)	273
$Ar^{OMe}ZnPh_2^-$	$ZnCl_2$	PhLi (2 equiv.) + p-OMe-C_6H_4MgBr (2 equiv.)	273
$Ar^{Me}ZnPh_2^-$	$ZnCl_2$	PhLi (2 equiv.) + p-Me-C_6H_4MgBr (2 equiv.)	273
$Ar^FZnPh_2^-$	$ZnCl_2$	PhLi (3 equiv.) + p-F-C_6H_4MgBr (1 equiv.)	273
$Ar^{Cl}ZnPh_2^-$	$ZnCl_2$	PhLi (3 equiv.) + p-Cl-C_6H_4MgBr (1 equiv.)	273

Trisalkyl- and alkyl-aryl zincate anions: An empty Schlenk flask (10 mL) was evacuated under continuous heating (523 K) and flushed with Ar. The operation was repeated at least three times. After the flask had cooled to room temperature, THF (10 mL) was filled in and cooled down to 195 K. Then, either $ZnMe_2$ (0.20 mL, 1.0 M) and MeLi (2 equiv.), $ZnEt_2$ (0.20 mL, 1.0 M) and EtLi (2 equiv.) or $ZnMe_2$ (0.20 mL, 1.0 M) and PhLi (1 or 2 equiv.) were added (Table 12). The solution (20 mM) was stirred for less than 5 min at 195 K prior to the mass-spectrometric measurement wherein the solution was continuously held at 195 K.

Table 12: Preparations of the sample solutions containing the denoted organozincate anions.

Species	Metal source	Transmetalation reagent	Temperature / K
Me_3Zn^-	$ZnMe_2$ solution	MeLi (2 equiv.)	195
Et_3Zn^-	$ZnEt_2$ solution	EtLi (2 equiv.)	195
$PhZnMe_2^-$	$ZnMe_2$ solution	PhLi (1 equiv.)	195
Ph_2ZnMe^-	$ZnMe_2$ solution	PhLi (2 equiv.)	195

Substituted ethylzincate anions: Et_2ZnF^- was prepared by heating (523 K) and evacuating an empty Schlenk flask, charging it with THF (10 mL), cooling it down to 195 K and then adding $ZnEt_2$ (0.20 mL, 1.0 M; 1 equiv.) as well as NBu_4F (1.0 M; 1 equiv.). Et_2ZnCl^- was prepared from charging a dried Schlenk flask (10 mL) with NBu_4Cl (0.055 g, 1 equiv.), evacuating it under mild heating (353 K) and flushing it with Ar for several times. THF (10 mL) was added. The mixture was stirred for 1 h, cooled down to 195 K and treated with $ZnEt_2$ (0.20 mL, 1.0 M, 1 equiv.). After stirring for less than 5 min, the sample solutions (20 mM) were used for the mass-spectrometric measurement and kept at 195 K.

5.1.1.2   Preparation of organoferrate species

Trisarylferrate anions: A Schlenk flask (10 mL) was charged with $Fe(acac)_3$ (0.035 g, 0.10 mmol) and repeatedly evacuated under heating (363 K) and flushed with Ar. After cooling to room temperature, $Fe(acac)_3$ was dissolved in THF (10 mL) and the solution was stirred for 1 h. After cooling to 195 K, the red-brown solution was treated with phenylmagnesium chloride (PhMgCl; 2.0 M, 4 equiv.) or mesitylmagnesium bromide (MesMgBr; 1.0 M, 4 equiv.) upon which the color changed to a dark green for Ph_3Fe^- and to a darker brown for Mes_3Fe^-. The solution was stirred for less than 5 min before the mass-spectrometric measurement and continuously cooled at 195 K.

5.1.2   Instrumentation

5.1.2.1   3D quadrupole ion trap

The mass-spectrometric experiments were carried out using a commercial 3D quadrupole ion-trap (QIT) mass spectrometer (HCT by Bruker Daltonik, Bremen, Germany) equipped with an atmospheric-pressure electrospray-ionization (Apollo by Bruker Daltonik, Bremen, Germany; sprayer by Agilent Technologies, Santa Clara, United States of America) source (Figure 75). The instrument settings applied are shown in Table 13.
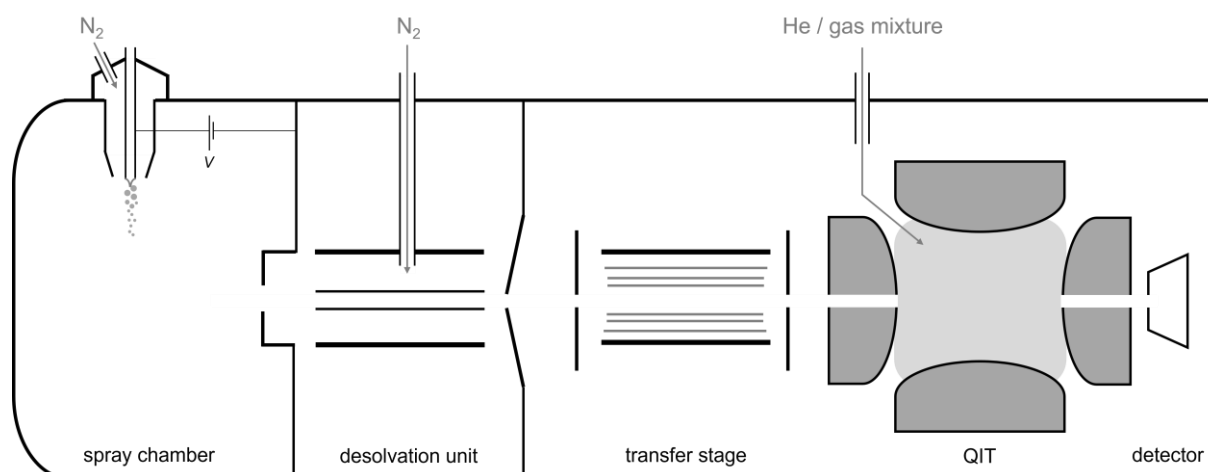
Figure 75:   Schematic representation of the 3D quadrupole-ion trap (QIT) mass spectrometer HCT by Bruker Daltonik used for this work.[165]

The sample solution is electrosprayed under the assistance of a nebulizer gas (N_2). The jet then enters the desolvation unit through the capillary cap. The glass capillary is warmed indirectly by a stream of heated gas (N_2). Subsequently, the ions leave the glass capillary and pass a skimmer into the transfer stage which consists of two octupole ion guides. Therein, the ions are focused into a beam and transferred towards the mass analyzer which they reach after passing two lenses. The mass analyzer is a typical 3D quadrupole ion trap

96

which allows for mass scans, mass isolation and gas-phase experiments such as collision-induced dissociation (CID) or ion-molecule reactions (IMR) by (exciting and) storing mass-selected ions for tunable durations. The so-called trap drive corresponds to a set of the Matthieu parameters. Small trap drives ensure the efficient trapping of lighter ions. Eventually, the ions are ejected from the QIT and detected.[165]

The pressure and temperature within the QIT are assumed to be p_{QIT} = $(0.61 \pm 0.19) \times 10^{-3}$ mbar and T_{QIT} = (310±20) K, respectively.[97,98,101]

Table 13: Instrument settings of the 3D quadrupole-ion trap mass spectrometer HCT used for the experiments of this work.

Source		Tune			
Capillary	+3000 V	Skimmer	−40.0 V		
End Plate Offset	−500 V	Cap Exit	−108.6 V	Mass range	20 – 1000 m/z
Nebulizer	0.7 bar	Oct 1 DC	−12.00 V	Oct RF	139.2 V
Dry Gas	5.0 or 10.0 L min^{-1}	Oct 2 DC	−1.70 V	Lens 1	5.0 V
Dry Temp	333 K	Trap Drive	33.5	Lens 2	60.0 V

5.1.2.2 Substrate inlet apparatus

To conduct ion-molecule reactions within the 3D quadrupole ion trap mass spectrometer, the QIT was charged with a mixture of the gaseous substrate (proton donor R'OH) and He (99.999%). The gas mixture was prepared with a home-built apparatus, which is referred to as the "gas-mixing chamber" (GMC). It was designed and set up by Parchomyk and Koszinowski.[101]
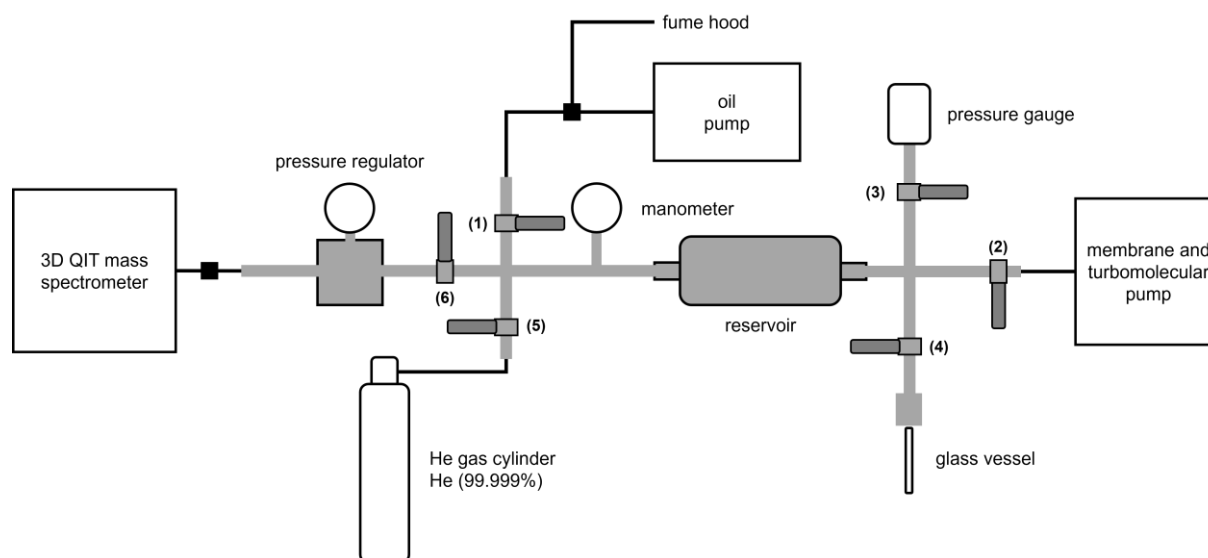
Figure 76: Schematic representation of the substrate-inlet apparatus used for this work. The apparatus allows for the mixing a substrate with He and the subsequent introduction of that mixture into the 3D QIT mass spectrometer through the He inlet of the instrument.[101]

The reservoir is evacuated by an oil pump (valve 1) and subsequently by a membrane and turbomolecular pump (valve 2) to pressures of around 5×10^{-5} mbar (valve 3). At this stage, a certain amount ($V_{substrate}$ = 3 – 100 μL) of the substrate, which is a volatile organic compound (e.g. the proton donor R'OH), is filled into the glass vessel. It is then purified by two cycles of pump (valve 4), freeze and thaw. Eventually, the substrate is evaporated into the gas-mixing chamber (V_{GMC} = 2.5 L) at T_{GMC} = 300 K. From a gas cylinder (valve 5), He (p_{GMC} = 6 bar; 99.999%) is added to give the desired gas mixture with a helium-to-substrate ratio of more than 99.9%. The gas mixture is reduced in pressure (valve 6) and let in to the

3D QIT mass spectrometer through its He inlet. The QIT is repeatedly flushed with the gas mixture before the experiments to ensure steady concentrations. For the actual kinetic measurements, the gas mixture is fed continuously into the QIT.[101]

The concentration of the substrate $N_{substrate}/V$ within the QIT results from the constitution of the gas mixture as well as the relative diffusion coefficients. First, the amount of the substrate $n_{substrate}$ is calculated from its density ρ and molar mass M (Equation 19).

$$n_{substrate} = \frac{V_{substrate} \times \rho}{M}$$
Equation 19

Next, the amount of He, n_{He}, in the gas-mixing chamber (GMC) is determined with the pressure p_{GMC}, the volume V_{GMC}, the temperature T_{GMC} and the universal gas constant R (Equation 20):

$$n_{He} = \frac{p_{GMC} \times V_{GMC}}{R \times T_{GMC}}$$
Equation 20

As He is pumped off more easily in the QIT, the relative amount of the gases $n_{substrate}/n_{He}$ needs to be corrected for their diffusion coefficients which are proportional to the square root of their molar masses M (Equation 21).

$$r_{QIT} = \frac{n_{substrate}}{n_{He}} \times \frac{\sqrt{M_{substrate}}}{\sqrt{M_{He}}}$$
Equation 21

The concentration of the substrate in the QIT, $N_{substrate}/V$, finally results from that adjusted ratio of the gases r_{QIT} with p_{QIT} and T_{QIT} being the pressure and temperature in the QIT and R and N_A being the universal gas constant and Avogadro constant, respectively (Equation 22).[101]

$$\frac{N_{substrate}}{V} = \frac{r_{QIT} \times p_{QIT} \times N_A}{R \times T_{QIT}}$$
Equation 22

5.1.3   Mass-spectrometric measurements

5.1.3.1   MS[1]

Sample solutions were infused either from a gas-tight syringe (Hamilton; 1000 µL) at flow rates of 0.50 mL h^{-1} at room temperature or by so-called pressurized sample infusion (PSI) if the sample solution was cooled. In the latter case, the Schlenk flask containing the sample solution was cooled at 195 K and connected to a gas cylinder (Ar) via its olive. The inlet line was introduced into the sample solution through an opening of the rubber septum. By generating an overpressure in the Schlenk flask, the sample solution was pushed out and injected into the mass spectrometer where it was electrosprayed.[151]

Negative ion-mode ESI mass spectra (MS[1]) were recorded for at least 1 min at the defined instrument settings (Table 13). The measurements were averaged with the program DataAnalysis 4.2 and analyzed with the program IsotopePattern (both by Bruker Daltonik). Every measurement was independently reproduced.

The original data of mass spectra can be found in the GRO.data repository.[166]

5.1.3.2   MS^n

Collision-induced dissociation (CID). Collision-induced dissociation experiments were carried out in the tandem-MS (MS^n) mode of the 3D QIT. First, the ion of interest was mass-selected and isolated (settings: *Isolation*, *Width*). One MS^n mass spectrum was recorded for 30 s. Afterwards, the ions were excited (settings: *Amplitude*, *FragTime* = 40 ms) and fragmented. An MS^n mass spectrum was recorded for at least 1 min and averaged with the program DataAnalysis 4.2 (Bruker Daltonik).

Kinetic measurements of ion-molecule reactions (IMR). Kinetic measurements were performed using the tandem mass-spectrometric (MS^n) feature of the 3D QIT. The species of interest was mass-selected (settings: *Isolation*, *Width*) and stored in the QIT for various reaction times t between 0 and 6000 ms (settings: *FragTime*, *FragDelay*). During that time period, the isolated ions reacted with an excess ($N_{substrate}/V$) of the substrate (proton donor R'OH) at a temperature of T = (310±20) K.[97,98] As a consequence, the signal intensity of the precursor ion decreased and the signal intensities of the product ions increased over the course of time. For each time step, mass spectra were recorded for at least 1 min and averaged with the program DataAnalysis 4.2 (Bruker Daltonik). Each measurement was reproduced independently.

The signal intensities of selected ions were extracted, normalized and plotted against the reaction time t. Species with relative signal intensities below 5% were neglected. The obtained time-dependent species profiles were fitted to a conceived reaction network using the software GEPASI 3.30 which gave effective rate constants k_{eff} of pseudo-first order for each input reaction. The effective rate constants k_{eff} were then converted into bimolecular rate constants k knowing the substrate concentration $N_{substrate}/V$ (Equation 23):

$$k = \frac{k_{eff}}{N_{substrate}/V} \qquad\qquad \text{Equation 23}$$

The experimental bimolecular rate constants k reported in this work are the mean value of two independent measurements. The experimental uncertainty corresponds to the relative error (statistical component within the 2σ confidence interval (95%)). The absolute errors are estimated to be ±30%.[101]

The research data of the kinetic measurements can be found in the GRO.data repository.[166]

5.2   Computational details

Exemplary input files for the calculations described below can be found in the GRO.data repository.[166]

5.2.1   Quantum-chemical calculations

5.2.1.1   Structure search and optimization

The initial structural guesses of the reactants, intermediates and products were created with the program Avogadro 1.2.0[167] and optimized using the implemented universal force field. Conformers were sampled either manually or with the software CREST 2.10.2 (settings: *cbonds* 0.05, *nci*) by the Grimme group.[168] The obtained structures were then optimized with the long-range corrected hybrid density functional ωB97X-D3[137–139] and Ahlrichs' def2-TZVP basis sets[140] as implemented in the software package ORCA 4.2.1 (*Grid7*, *FinalGrid7*, *VeryTightSCF*) by Neese and coworkers.[116,117]

The transition structures (TS) were located by performing a relaxed surface scan based on the pre-reactive complex structure guess in which either the distance between the acidic proton of the proton donor R'OH and the accepting site of the organometallic ion was reduced or the bond length between the hydroxy oxygen atom of the proton donor R'OH and the metal center of the organometallic ion was shortened. The structure being highest in energy in this scan was used for the TS optimization. The transition structure featured one single imaginary frequency which corresponded to the motion of the acidic proton between the donor and acceptor site. In some cases, the reactive mode was more similar to the vibration of the accepting residue being exchanged for the moiety of the proton donor. The final pre-reactive and product complexes of the reactions were searched for by using the implemented intrinsic reaction coordinate (IRC) method and subsequent geometry optimizations in ORCA 4.2.1.

To validate the geometries to be minimum-energy structures, analytical vibrational frequency calculations were carried out which found no imaginary frequencies. The structures served for the computation of the zero-point vibrational energy (ZPVE) and the electronic single-point energy (SPE) calculations with more sophisticated quantum-chemical methods.

5.2.1.2   Electronic single-point energy calculations

Electronic single-point energies (SPE) were calculated in ORCA 4.2.1[116,117] with the coupled-cluster method DLPNO-CCSD(T)[110,111] (*NormalPNO*) and Dunning's correlation-consistent cc-pVnZ basis sets extrapolated to the complete basis set (CBS) limit (n = T; Q). [141–144,169]

Energies in this work are given as enthalpies at 0 K (ZPVE + SPE), ΔH_0, relative to the reactants in kJ mol^{-1}. ΔH_0 is most representative for the energetics of microcanonical reaction ensembles under low-pressure conditions as they are present in the mass-spectrometric experiments carried out here.[128]

In some cases, atomic charges of reactant structures were calculated from the DLPNO-CCSD(T) electron distributions employing the natural population analysis (NPA) scheme by Weinhold[150] as implemented in ORCA 4.2.1 (*NBO*).

5.2.2 Kinetic modelling

5.2.2.1 Capture rates

The theoretical rates for the collision of the organometallic ions with the proton donors, k_{coll}, were calculated according to the capture theory by Su and Chesnavich[122–124] using the program COLRATE by Lim[170] for temperatures of T = 290, 310 and 330 K. For the sake of consistency, the dipole moments μ and polarizability volumina α' of the proton donors were computed from the DLPNO-CCSD(T) electron distributions in ORCA 4.2.1 (Table 14).[116,117]

Table 14: Calculated dipole moments and polarizability volumes used for the calculation of capture rates.

Proton donor	Dipole moment μ / D	Polarizability volume α' / Å^3
CF$_3$CH$_2$OH (R^{F3}OH)	1.95	4.38
CF$_2$HCH$_2$OH (R^{F2}OH)	0.72	4.37
CFH$_2$CH$_2$OH (R^{F1}OH)	1.59	4.38
CH$_3$CH$_2$OH (R^{F0}OH)	1.68	4.47
H$_2$O	1.99	1.09
HCOOH	1.72	2.78

Those capture rates pose the upper limit for the rate constants of the protonation reactions as the encounter of the reactants is the prerequisite. However, they underestimate the actual collision rates because the ions are treated as point charges and thus, their spatial extent is neglected.[126]

The capture rates k_{coll} were also used to calculate the reaction efficiencies φ_{exp} from the bimolecular reaction rate constants k (Equation 24).

$$\varphi_{exp} = \frac{k}{k_{coll}}$$

Equation 24

5.2.2.2 Reaction rates

The theoretical rate constants k_{theo} for the protonation reactions were computed with the Master-equation solver MESMER 6.0 by Glowacki et al.[131] The results of the quantum-chemical calculations (enthalpies at 0 K, rotational constants, vibrational frequencies) of the species along the reaction pathway served as the input data. The reaction conditions were chosen as in the experiment: T = 290, 310 and 330 K (T); p_{He} = 0.6 × 10^{-3} mbar (P), $N_{substrate}/V$ = 5.1 × 10^9 –1.8 × 10^{11} cm^{-3} (*excessReactantConc*). The program was set to *precision*: double-double, *grainSize*: 20 cm^{-1}, *energyAboveTheTopHill*: 50 kJ mol^{-1} and *simpleCalc*.

The reaction scheme for the kinetic modelling was simplified in that the last step of the double-well potential, i.e. the dissociation of the product complex into the products, was neglected. So, the reactants (*deficientReactant*, *excessReactant*) form the pre-reactive complex (*modelled*) and then react directly to the products (*sink*) via the transition structure (TS). The encountering of the reactants was computed with the built-in inverse Laplace transform (ILT) method (*MCRCMethod*: MesmerILT) with the capture rate as the rate constant (*preExponential*). The proton transfer step was modelled using standard RRKM theory (*MCRCMethod: RRKM*). The rotational symmetry and multiplicity of the species was accounted for. Densities of states were calculated in the frameworks of either classical rotors (*ClassicalRotors*) or quantum-mechanical rotors (*QMRotors*) if methyl torsions were considered as free rotors instead of as low-frequency vibrations.

MESMER 6.0 generated time-dependent species profiles which were fitted with GEPASI 3.30 to extract the effective rate constants k_{eff} of pseudo-first order. Afterwards, the effective rate constants k_{eff} were converted into the theoretical bimolecular rate constants k_{theo} according to Equation 23.

6   References

[1]   P. Y. Bruice, *Organische Chemie. Studieren kompakt,* 5th ed., Pearson Studium, Munich, **2011**.

[2]   a) J. Li, L. Ackermann, *Angew. Chem. Int. Ed*. **2015**, *54*, 3635; *Angew. Chem.* **2015**, *127*, 3706; b) D. Zell, M. Bursch, V. Müller, S. Grimme, L. Ackermann, *Angew. Chem. Int. Ed.* **2017**, *56*, 10378; *Angew. Chem.* **2017**, *129*, 10514.

[3]   J. Garcia-Alvarez, E. Hevia, V. Capriati, *Eur. J. Org. Chem.* **2015**, *2015*, 6779.

[4]   J. Garcia-Alvarez, E. Hevia, V. Capriati, *Chem. Eur. J.* **2018**, *24*, 14854.

[5]   F. M. Perna, P. Vitale, V. Capriati, *Current Op. Green Sust. Chem.* **2020**, *21*, 27.

[6]   F. M. Perna, P. Vitale, V. Capriati, *Current Op. Green Sust. Chem.* **2021**, *30*, 100487.

[7]   G. Dilauro, C. S. Azzollini, P. Vitale, A. Salomone, F. M. Perna, V. Capriati, *Angew. Chem. Int. Ed*. **2021**, *60*, 10632; *Angew. Chem.* **2021**, *133*, 10726.

[8]   R. P. Bell, *The proton in chemistry,* 2nd ed., Cornell University Press, Ithaca, New York, **1973**.

[9]   C. E. Mortimer, U. Müller, *Chemie. Das Basiswissen der Chemie,* 10th ed., Thieme, Stuttgart, **2010**.

[10]   S. Arrhenius, *Z. Phys. Chem.* **1887**, *1*, 631.

[11]   J. N. Brønsted, *Chem. Rev.* **1928**, *5*, 231.

[12]   a) J. N. Brønsted, K. Pedersen, *Z. Phys. Chem.* **1924**, *108*, 185; b) R. P. Bell, *Acid-Base Catalysis*, Oxford University Press (OUP), London, **1941**; c) A. J. Kresge, *Chem. Soc. Rev.* **1973**, *2*, 475.

[13]   C. L. Perrin, I. Agranat, A. Bagno, S. E. Braslavsky, P. A. Fernandes, J.-F. Gal, G. C. Lloyd-Jones, H. Mayr, J. R. Murdoch, N. S. Nudelman, L. Radom, Z. Rappoport, M.-F. Ruasse,H.-U. Siehl, Y. Takeuchi, T. T. Tidwell, E. Uggerud, I. H. Williams, *Pure Appl. Chem.* **2022**, *94*, 353.

[14]   C. D. Ritchie, *Physical organic chemistry. The fundamental concepts*, M. Dekker, Inc., New York, **1975**.

[15]   L. P. Hammett, *Physical Organic Chemistry. Reaction Rates, Equilibria, and Mechanisms,* 1st ed., McGraw-Hill Book Company, Inc., New York, **1940**.

[16]   Jack Hine, *Physical Organic Chemistry,* 2nd ed., McGraw-Hill Book Company, Inc., New York, **1962**.

[17]   a) M. G. Evans, M. Polanyi, *Trans. Faraday Soc.* **1936**, *32*, 1333; b) M. G. Evans, M. Polanyi, *Trans. Faraday Soc.* **1938**, *34*, 11; c) G. S. Hammond, *J. Am. Chem. Soc.* **1955**, *77*, 334.

[18]   L. P. Hammett, *Chem. Rev.* **1935**, *17*, 125.

[19]   L. P. Hammett, *J. Am. Chem. Soc.* **1937**, *59*, 96.

[20]   L. P. Hammett, *Trans. Faraday Soc.* **1938**, *34*, 156.

[21]   J. Shorter, *Chem. i. u. Z.* **1985**, *19*, 197.

[22]   C. Hansch, A. Leo, R. W. Taft, *Chem. Rev.* **1991**, *91*, 165.

[23]   M. Eigen, *Angew. Chem. Int. Ed.* **1964**, *3*, 1; *Angew. Chem.* **1963**, *75*, 489.

[24]   a) S. Cukierman, *Biochim. Biophys. Acta* **2006**, *1757*, 876; b) C. A. Reed, *Acc. Chem. Res.* **2013**, *46*, 2567.

[25]   M. Eigen, *Immeasurably fast reactions*. *Nobel Lecture*, **1967**.

[26]   M. Eigen, *Discuss. Faraday Soc.* **1965**, *39*, 7.

[27]   M. Eigen, *Die "unmessbar" schnellen Reaktionen*. *Frühe Arbeiten (1954-1967)*, Deutsch, Thun, Frankfurt am Main, **1995**.

[28] W. P. Jencks, *Chem. Rev.* **1985**, *85*, 511.

[29] a) W. P. Jencks, *Chem. Rev.* **1972**, *72*, 705; b) W. P. Jencks, *J. Am. Chem. Soc.* **1972**, *94*, 4731; c) W. P. Jencks, *Acc. Chem. Res.* **1976**, *9*, 425.

[30] W. P. Jencks, *Annu. Rev. Biochem.* **1997**, *66*, 1.

[31] F. G. Bordwell, W. J. Boyle, *J. Am. Chem. Soc.* **1972**, *94*, 3907.

[32] C. F. Bernasconi, *Acc. Chem. Res.* **1992**, *25*, 9.

[33] R. A. Marcus, *Annu. Rev. Phys. Chem.* **1964**, *15*, 155.

[34] J. A. Dodd, J. I. Brauman, *J. Phys. Chem.* **1986**, *90*, 3559.

[35] a) D. J. McLennan, *J. Chem. Educ.* **1976**, *53*, 348; b) W. H. Saunders, *J. Phys. Chem.* **1982**, *86*, 3321; c) J. P. Guthrie, *J. Am. Chem. Soc.* **1996**, *118*, 12886.

[36] E. J. Piechota, G. J. Meyer, *J. Chem. Educ.* **2019**, *96*, 2450.

[37] a) C. F. Bernasconi, *Pure Appl. Chem.* **1982**, *54*, 2335; b) C. F. Bernasconi, J. X. Ni, *J. Am. Chem. Soc.* **1993**, *115*, 5060.

[38] C. F. Bernasconi, *Tetrahedron* **1985**, *41*, 3219.

[39] C. F. Bernasconi, *Acc. Chem. Res.* **1987**, *20*, 301.

[40] C. Costentin, J.-M. Savéant, *J. Am. Chem. Soc.* **2004**, *126*, 14787.

[41] C. Costentin, J.-M. Savéant, *Chem. Sci.* **2020**, *11*, 1006.

[42] a) S. Gronert, *Chem. Rev.* **2001**, *101*, 329; b) S. Gronert, *Acc. Chem. Res.* **2003**, *36*, 848; c) R. A. J. O'Hair, N. Rijs, *Acc. Chem. Res.* **2015**, *48*, 329.

[43] S. Gronert, *Mass Spectrom. Rev.* **2005**, *24*, 100.

[44] J. K. Laerdahl, E. Uggerud, *Int. J. Mass Spectrom.* **2002**, *214*, 277.

[45] R. A. J. O'Hair, *Chem. Commun.* **2006**, 1469.

[46] V. Gold, *The IUPAC Compendium of Chemical Terminology*, International Union of Pure and Applied Chemistry (IUPAC), Research Triangle Park, North Carolina, **2019**.

[47] P. Linstrom, *NIST Chemistry WebBook, NIST Standard Reference Database 69*, National Institute of Standards and Technology, **1997**.

[48] a) C. H. DePuy, J. J. Grabowski, V. M. Bierbaum, *Science* **1982**, *218*, 955; b) R. R. Squires, V. M. Bierbaum, J. J. Grabowski, C. H. DePuy, *J. Am. Chem. Soc.* **1983**, *105*, 5185; c) T. Thanh Dang, E. L. Motell, M. J. Travers, E. P. Clifford, G. Barney Ellison, C. H. DePuy, V. M. Bierbaum, *Int. J. Mass Spectrom.* **1993**, *123*, 171; d) G. E. Davico, V. M. Bierbaum, C. H. DePuy, G. B. Ellison, R. R. Squires, *J. Am. Chem. Soc.* **1995**, *117*, 2590; e) S. Kato, T. T. Dang, S. E. Barlow, C. H. DePuy, V. M. Bierbaum, *Int. J. Mass Spectrom.* **2000**, *195-196*, 625; f) C. H. DePuy, *J. Org. Chem.* **2002**, *67*, 2393; g) S. Kato, K. E. Carrigan, C. H. DePuy, V. M. Bierbaum, *Chem. Eur. J.* **2004**, *10*, 225.

[49] J. M. van Doren, S. E. Barlow, C. H. DePuy, V. M. Bierbaum, *Int. J. Mass Spectrom.* **1987**, *81*, 85.

[50] a) C. C. Han, J. A. Dodd, J. I. Brauman, *J. Phys. Chem.* **1986**, *90*, 471; b) B. D. Wladkowski, A. L. L. East, J. E. Mihalick, W. D. Allen, J. I. Brauman, *J. Chem. Phys.* **1994**, *100*, 2058; c) M. L. Chabinyc, J. I. Brauman, *J. Am. Chem. Soc.* **1998**, *120*, 10863; d) X. Chen, J. I. Brauman, *J. Am. Chem. Soc.* **2008**, *130*, 15038; e) J. I. Brauman, *Science* **2008**, *319*, 168.

[51] G. A. Janaway, J. I. Brauman, *J. Phys. Chem. A* **2000**, *104*, 1795.

[52] K. F. Lim, J. I. Brauman, *J. Chem. Phys.* **1991**, *94*, 7164.

[53] F. K. Meyer, M. J. Pellerite, J. I. Brauman, *Helv. Chim. Acta* **1981**, *64*, 1058.

[54] K. F. Lim, J. I. Brauman, *Chem. Phys. Lett.* **1991**, *177*, 326.

[55] J. L. Wilbur, B. D. Wladkowski, J. I. Brauman, *J. Am. Chem. Soc.* **1993**, *115*, 10823.

[56] J. A. Dodd, S. Baer, C. R. Moylan, J. I. Brauman, *J. Am. Chem. Soc.* **1991**, *113*, 5942.

[57] W. E. Farneth, J. I. Brauman, *J. Am. Chem. Soc.* **1976**, *98*, 7891.

[58] C. C. Han, J. I. Brauman, *J. Am. Chem. Soc.* **1989**, *111*, 6491.

[59] a) H.-H. Bueker, E. Uggerud, *J. Phys. Chem.* **1995**, *99*, 5945; b) E. Uggerud, *J. Chem. Soc., Perkin Trans. 2* **1999**, 1459; c) E. Uggerud, *Eur. J. Mass Spectrom.* **2000**, *6*, 131; d) L. Bache-Andreassen, E. Uggerud, *Eur. J. Mass Spectrom.* **2004**, *10*, 233; e) E. Uggerud, *Chem. Eur. J.* **2006**, *12*, 1127; f) M. J. Ryding, P. U. Andersson, A. S. Zatula, E. Uggerud, *Eur. J. Mass Spectrom.* **2012**, *18*, 215; g) A. S. Zatula, M. J. Ryding, P. U. Andersson, E. Uggerud, *Int. J. Mass Spectrom.* **2012**, *330-332*, 191.

[60] S. Gronert, *J. Am. Chem. Soc.* **1993**, *115*, 10258.

[61] a) S. Gronert, J. R. Keeffe, *J. Am. Chem. Soc.* **2005**, *127*, 2324; b) S. Gronert, J. R. Keeffe, *J. Org. Chem.* **2006**, *71*, 5959.

[62] S. Gronert, C. Kimura, *J. Phys. Chem. A* **2003**, *107*, 8932.

[63] J. R. Keeffe, S. Gronert, M. E. Colvin, N. L. Tran, *J. Am. Chem. Soc.* **2003**, *125*, 11730.

[64] C. F. Bernasconi, P. J. Wenzel, J. R. Keeffe, S. Gronert, *J. Am. Chem. Soc.* **1997**, *119*, 4008.

[65] a) C. F. Bernasconi, P. J. Wenzel, *J. Am. Chem. Soc.* **1994**, *116*, 5405; b) C. F. Bernasconi, P. J. Wenzel, *J. Am. Chem. Soc.* **1996**, *118*, 10494; c) C. F. Bernasconi, P. J. Wenzel, *J. Org. Chem.* **2003**, *68*, 6870; d) C. F. Bernasconi, *J. Am. Chem. Soc.* **2003**, *125*, 151; e) C. F. Bernasconi, P. J. Wenzel, *J. Org. Chem.* **2010**, *75*, 8422.

[66] C. F. Bernasconi, P. J. Wenzel, *J. Am. Chem. Soc.* **2001**, *123*, 2430.

[67] C. F. Bernasconi, P. J. Wenzel, *J. Am. Chem. Soc.* **2001**, *123*, 7146.

[68] C. F. Bernasconi, P. J. Wenzel, *J. Org. Chem.* **2001**, *66*, 968.

[69] J. Mikosch, M. Weidemüller, R. Wester, *Int. Rev. Phys. Chem.* **2010**, *29*, 589.

[70] R. Wester, *Mass Spectrom. Rev.* **2022**, *41*, 627.

[71] a) E. S. Shubina, A. N. Krylov, N. V. Belkova, L. M. Epstein, A. P. Borisov, V. D. Mahaev, *J. Organomet. Chem.* **1995**, *493*, 275; b) R. M. Bullock, J.-S. Song, D. J. Szalda, *Organometallics* **1996**, *15*, 2504; c) B. F. M. Kimmich, R. M. Bullock, *Organometallics* **2002**, *21*, 1504.

[72] T. J. Johnson, B. E. Hauger, E. B. Lobkovsky, K. G. Caulton, *J. Organomet. Chem.* **1992**, *424*, 371.

[73] R. W. Johnson, R. G. Pearson, *Inorg. Chem.* **1971**, *10*, 2091.

[74] P. L. Bogdan, K. H. Whitmire, J. W. Kolis, D. F. Shriver, E. M. Holt, *J. Organomet. Chem.* **1984**, *272*, 169.

[75] G. J. P. Britovsek, R. A. Taylor, G. J. Sunley, D. J. Law, A. J. P. White, *Organometallics* **2006**, *25*, 2074.

[76] M. S. Foster, J. L. Beauchamp, *J. Am. Chem. Soc.* **1975**, *97*, 4814.

[77] R. R. Corderman, J. L. Beauchamp, *Inorg. Chem.* **1976**, *15*, 665.

[78] A. E. Stevens, J. L. Beauchamp, *J. Am. Chem. Soc.* **1979**, *101*, 245.

[79] a) R. A. J. O'Hair, A. K. Vrkic, P. F. James, *J. Am. Chem. Soc.* **2004**, *126*, 12173; b) M. M. Meyer, G. N. Khairallah, S. R. Kass, R. A. J. O'Hair, *Angew. Chem. Int. Ed.* **2009**, *48*, 2934; c) M. G. Leeming, G. N. Khairallah, G. Da Silva, R. A. J. O'Hair, *Organometallics* **2011**, *30*, 4297; d) M. J. Woolley, G. N. Khairallah, G. Da Silva, P. S. Donnelly, B. F. Yates, R. A. J. O'Hair, *Organometallics* **2013**, *32*, 6931; e) M. J. Woolley, G. N. Khairallah, G. Da Silva, P. S. Donnelly, R. A. J. O'Hair, *Organometallics* **2014**, *33*, 5185.

[80] G. N. Khairallah, G. Da Silva, R. A. J. O'Hair, *Angew. Chem. Int. Ed.* **2014**, *53*, 10979; *Angew. Chem*. **2014**, *126*, 11159.

[81] G. N. Khairallah, C. Thum, R. A. J. O'Hair, *Organometallics* **2009**, *28*, 5002.

[82] a) A. Zavras, G. N. Khairallah, T. U. Connell, J. M. White, A. J. Edwards, P. S. Donnelly, R. A. J. O'Hair, *Angew. Chem. Int. Ed.* **2013**, *52*, 8391; b) A. Zavras, H. Ghari, A. Ariafard, A. J. Canty, R. A. J. O'Hair, *Inorg. Chem.* **2017**, *56*, 2387.

[83] a) T. Waters, A. G. Wedd, R. A. J. O'Hair, *Chem. Eur. J.* **2007**, *13*, 8818; b) B. L. Harris, T. Waters, G. N. Khairallah, R. A. J. O'Hair, *J. Phys. Chem. A* **2013**, *117*, 1124.

[84] J. H. Gross, *Massenspektrometrie. Ein Lehrbuch*, Springer, Berlin, Heidelberg, **2013**.

[85] R. M. Caprioli, M. L. Gross, *The encyclopedia of mass spectrometry. Fundamentals of and Applications to Organic (and Organometallic) Compounds,* 1st ed., Elsevier, Amsterdam, **2009**.

[86] M. S. Foster, J. L. Beauchamp, *J. Am. Chem. Soc.* **1975**, *97*, 4808.

[87] V. M. Bierbaum, *Int. J. Mass Spectrom.* **2015**, *377*, 456.

[88] a) C. Collette, L. Drahos, E. de Pauw, K. Vékey, *Rapid Commun. Mass Spectrom.* **1998**, *12*, 1673; b) V. Gabelica, E. de Pauw, *Mass Spectrom. Rev.* **2005**, *24*, 566; c) D. Asakawa, K. Saikusa, *J. Am. Soc. Mass Spectrom.* **2022**, *33*, 1548; d) D. Asakawa, *J. Am. Soc. Mass Spectrom.* **2023**, *34*, 435.

[89] R. Rahrt, T. Auth, M. Demireva, P. B. Armentrout, K. Koszinowski, *Anal. Chem.* **2019**, *91*, 11703.

[90] R. A. J. O'Hair, *Mass Spectrom. Rev.* **2021**, *40*, 782.

[91] M. Dole, L. L. Mack, R. L. Hines, R. C. Mobley, L. D. Ferguson, M. B. Alice, *J. Chem. Phys.* **1968**, *49*, 2240.

[92] a) M. Yamashita, J. B. Fenn, *J. Phys. Chem.* **1984**, *88*, 4451; b) M. Yamashita, J. B. Fenn, *J. Phys. Chem.* **1984**, *88*, 4671.

[93] J. B. Fenn, *Angew. Chem. Int. Ed.* **2003**, *42*, 3871.

[94] P. Kebarle, U. H. Verkerk, *Mass Spectrom. Rev.* **2009**, *28*, 898.

[95] P. B. Armentrout, M. L. Gross, R. M. Caprioli, *The encyclopedia of mass spectrometry. Theory and Ion Chemistry*, 1st ed., Elsevier, Amsterdam, **2003**.

[96] S. Gronert, L. M. Pratt, S. Mogali, *J. Am. Chem. Soc.* **2001**, *123*, 3081.

[97] S. Gronert, *J. Am. Soc. Mass Spectrom.* **1998**, *9*, 845.

[98] T. Waters, R. A. J. O'Hair, A. G. Wedd, *J. Am. Chem. Soc.* **2003**, *125*, 3384.

[99] G. E. Reid, R. A. J. O'Hair, M. L. Styles, W. D. McFadyen, R. J. Simpson, *Rapid Commun. Mass Spectrom.* **1998**, *12*, 1701.

[100] a) C. H. DePuy, V. M. Bierbaum, *Acc. Chem. Res.* **1981**, *14*, 146; b) S. T. Graul, R. R. Squires, *Mass Spectrom. Rev.* **1988**, *7*, 263.

[101] T. Parchomyk, K. Koszinowski, *J. Mass Spectrom.* **2019**, *54*, 81.

[102] R. Rahrt, K. Koszinowski, *J. Phys. Chem. A* **2021**, *125*, 10725.

[103] S. Lülf, L. Guo, T. Parchomyk, J. N. Harvey, K. Koszinowski, *Chem. Eur. J.* **2022**, *28*, e202202030.

[104] F. Jensen, *Introduction to computational chemistry*, Wiley, Chichester, UK, Hoboken, New Jersey, **2017**.

[105] P. L. Houston, *Chemical kinetics and reaction dynamics*, Dover Publications, Mineola, New York, **2001**.

[106] A. Szabo, N. S. Ostlund, *Modern quantum chemistry. Introduction to advanced electronic structure theory*, Dover Publications, Inc, Garden City, New York, **2020**.

[107] C. Møller, M. S. Plesset, *Phys. Rev.* **1934**, *46*, 618.

[108] R. J. Bartlett, M. Musiał, *Rev. Mod. Phys.* **2007**, *79*, 291.

[109] D. G. Liakos, M. Sparta, M. K. Kesharwani, J. M. L. Martin, F. Neese, *J. Chem. Theory Comput.* **2015**, *11*, 1525.

[110] Y. Guo, C. Riplinger, U. Becker, D. G. Liakos, Y. Minenkov, L. Cavallo, F. Neese, *J. Chem. Phys.* **2018**, *148*, 11101.

[111] Y. Guo, C. Riplinger, D. G. Liakos, U. Becker, M. Saitow, F. Neese, *J. Chem. Phys.* **2020**, *152*, 24116.

[112] P. Hohenberg, W. Kohn, *Phys. Rev.* **1964**, *136*, B864-B871.

[113] J. P. Perdew, *AIP Conference Proceedings* **2001**, *577*, 1.

[114] a) L. Goerigk, S. Grimme, *Phys. Chem. Chem. Phys.* **2011**, *13*, 6670; b) L. Goerigk, A. Hansen, C. Bauer, S. Ehrlich, A. Najibi, S. Grimme, *Phys. Chem. Chem. Phys.* **2017**, *19*, 32184.

[115] a) S. Grimme, S. Ehrlich, L. Goerigk, *J. Comput. Chem.* **2011**, *32*, 1456; b) L. Goerigk in *Non-covalent Interactions in Quantum Chemistry and Physics*, Elsevier, **2017**, 195–219.

[116] F. Neese, *WIREs Comput. Mol. Sci.* **2012**, *2*, 73.

[117] F. Neese, *WIREs Comput. Mol. Sci.* **2018**, *8*, e1327.

[118] M. Bursch, J.-M. Mewes, A. Hansen, S. Grimme, *Angew. Chem. Int. Ed.* **2022**, e202205735.

[119] R. A. Mata, M. A. Suhm, *Angew. Chem. Int. Ed.* **2017**, *56*, 11011.

[120] T. F. Moran, W. H. Hamill, *J. Chem. Phys.* **1963**, *39*, 1413.

[121] T. Su, M. T. Bowers, *Int. J. Mass Spectrom.* **1973**, *12*, 347.

[122] T. Su, W. J. Chesnavich, *J. Chem. Phys.* **1982**, *76*, 5183.

[123] T. Su, *J. Chem. Phys.* **1988**, *88*, 4102.

[124] T. Su, *J. Chem. Phys.* **1988**, *89*, 5355.

[125] a) M. T. Bowers, T. Su in *Advances in Electronics and Electron Physics* Academic Press, **1973**, 223–279; b) T. Su, E. C. F. Su, M. T. Bowers, *Int. J. Mass Spectrom.* **1978**, *28*, 285.

[126] G. Kummerlöwe, M. K. Beyer, *Int. J. Mass Spectrom.* **2005**, *244*, 84.

[127] G. Wedler, H.-J. Freund, *Lehrbuch der Physikalischen Chemie,* 6th ed., Wiley-VCH, Weinheim, **2012**.

[128] P. D. Dau, P. B. Armentrout, M. C. Michelini, J. K. Gibson, *Phys. Chem. Chem. Phys.* **2016**, *18*, 7334.

[129] J. A. Miller, S. J. Klippenstein, *J. Phys. Chem. A* **2006**, *110*, 10528.

[130] Y. Georgievskii, J. A. Miller, M. P. Burke, S. J. Klippenstein, *J. Phys. Chem. A* **2013**, *117*, 12146.

[131] D. R. Glowacki, C.-H. Liang, C. Morley, M. J. Pilling, S. H. Robertson, *J. Phys. Chem. A* **2012**, *116*, 9545.

[132] R. Mata, M. A. Suhm, *RTG 2455 – Benchmark experiments for numerical quantum chemistry*, URL: https://uni-goettingen.de/en/587836.html, **2022**.

[133] P. Knochel, J. J. Almena Perea, P. Jones, *Tetrahedron* **1998**, *54*, 8275.

[134] a) K. Koszinowski, P. Böhrer, *Organometallics* **2009**, *28*, 771; b) J. E. Fleckenstein, K. Koszinowski, *Organometallics* **2011**, *30*, 5018; c) K. Koszinowski, C. Müller, H. Brand, J. E. Fleckenstein, *Organometallics* **2012**, *31*, 7165; d) A. Hernán-Gómez, E. Herd, E. Hevia, A. R. Kennedy, P. Knochel, K. Koszinowski, S. M. Manolikakes, R.

E. Mulvey, C. Schnegelsberg, *Angew. Chem. Int. Ed.* **2014**, *53*, 2706; *Angew. Chem.* **2014**, *126*, 2744.

[135] K. Koszinowski, P. Böhrer, *Organometallics* **2009**, *28*, 100.

[136] W. A. Donald, G. N. Khairallah, R. A. J. O'Hair, *J. Am. Soc. Mass Spectrom.* **2013**, *24*, 811.

[137] J.-D. Chai, M. Head-Gordon, *Phys. Chem. Chem. Phys.* **2008**, *10*, 6615.

[138] Y.-S. Lin, G.-D. Li, S.-P. Mao, J.-D. Chai, *J. Chem. Theory Comput.* **2013**, *9*, 263.

[139] S. Grimme, J. Antony, S. Ehrlich, H. Krieg, *J. Chem. Phys.* **2010**, *132*, 154104.

[140] F. Weigend, R. Ahlrichs, *Phys. Chem. Chem. Phys.* **2005**, *7*, 3297.

[141] T. H. Dunning, *J. Chem. Phys.* **1989**, *90*, 1007.

[142] F. Weigend, A. Köhn, C. Hättig, *J. Chem. Phys.* **2002**, *116*, 3175.

[143] N. B. Balabanov, K. A. Peterson, *J. Chem. Phys.* **2005**, *123*, 64107.

[144] N. B. Balabanov, K. A. Peterson, *J. Chem. Phys.* **2006**, *125*, 74110.

[145] S. Kozuch, J. M. L. Martin, *J. Comput. Chem.* **2013**, *34*, 2327.

[146] a) R. A. Kendall, T. H. Dunning, R. J. Harrison, *J. Chem. Phys.* **1992**, *96*, 6796; b) c) D. E. Woon, T. H. Dunning, *J. Chem. Phys.* **1993**, *98*, 1358; c) B. P. Prascher, D. E. Woon, K. A. Peterson, T. H. Dunning, A. K. Wilson, *Theor. Chem. Acc* **2011**, *128*, 69.

[147] E. Paulechka, A. Kazakov, *J. Phys. Chem. A* **2017**, *121*, 4379.

[148] I. Sandler, J. Chen, M. Taylor, S. Sharma, J. Ho, *J. Phys. Chem. A* **2021**, *125*, 1553.

[149] S. Mallick, B. Roy, P. Kumar, *Comput. Theor. Chem.* **2020**, *1187*, 112934.

[150] A. E. Reed, R. B. Weinstock, F. Weinhold, *J. Chem. Phys.* **1985**, *83*, 735.

[151] G. T. Thomas, S. Donnecke, I. C. Chagunda, J. S. McIndoe, *Chemistry Methods* **2022**, *2*.

[152] a) C. A. Schalley, D. Schröder, H. Schwarz, K. Möbus, G. Boche, *Chem. Ber.* **1997**, *130*, 1085; b) M. Rauser, D. P. Warzecha, M. Niggemann, *Angew. Chem. Int. Ed.* **2018**, *57*, 5903.

[153] R. Rahrt, K. Koszinowski, *Chem. Eur. J.* **2023**, *29*, e202203611.

[154] a) C. H. DePuy, S. Gronert, S. E. Barlow, V. M. Bierbaum, R. Damrauer, *J. Am. Chem. Soc.* **1989**, 1968; b) J. R. Smith, J. B. Kim, W. C. Lineberger, *Phys. Rev. A* **1997**, *55*, 2036.

[155] a) P. Garcia-Alvarez, R. E. Mulvey, J. A. Parkinson, *Angew. Chem. Int. Ed.* **2011**, *50*, 9668; *Angew. Chem.* **2011**, *123*, 9842 b) C. Schnegelsberg, S. Bachmann, M. Kolter, T. Auth, M. John, D. Stalke, K. Koszinowski, *Chem. Eur. J.* **2016**, *22*, 7752.

[156] C. Vidal, J. García-Álvarez, A. Hernán-Gómez, A. R. Kennedy, E. Hevia, *Angew. Chem. Int. Ed.* **2014**, *53*, 5969; *Angew. Chem.* **2014**, *126*, 6079.

[157] a) I. Bauer, H.-J. Knölker, *Chem. Rev.* **2015**, *115*, 3170; b) T. Parchomyk, K. Koszinowski, *Synthesis* **2017**, *49*, 3269; c) S. Rana, J. P. Biswas, S. Paul, A. Paik, D. Maiti, *Chem. Soc. Rev.* **2021**, *50*, 243.

[158] T. Parchomyk, K. Koszinowski, *Chem. Eur. J.* **2016**, *22*, 15609.

[159] T. Parchomyk, K. Koszinowski, *Chem. Eur. J.* **2017**, *23*, 3213.

[160] T. Parchomyk, S. Demeshko, F. Meyer, K. Koszinowski, *J. Am. Chem. Soc.* **2018**, *140*, 9709.

[161] T. Parchomyk, K. Koszinowski, *Chem. Eur. J.* **2018**, *24*, 16342.

[162] J. Loup, T. Parchomyk, S. Lülf, S. Demeshko, F. Meyer, K. Koszinowski, L. Ackermann, *Dalton Trans.* **2019**, *48*, 5135.

[163] R. Rahrt, B. Hein-Janke, K. Koszinowski, R. Mata, *Fe-MAN challenge. Ferrates – Microkinetic Assessment of Numerical quantum chemistry*, URL: https://qmbench.net/challenges/feman/feman, **2023**.

[164] a) S. L. Daifuku, M. H. Al-Afyouni, B. E. R. Snyder, J. L. Kneebone, M. L. Neidig, *J. Am. Chem. Soc.* **2014**, *136*, 9132; b) R. B. Bedford, P. B. Brenner, E. Carter, P. M. Cogswell, M. F. Haddow, J. N. Harvey, D. M. Murphy, J. Nunn, C. H. Woodall, *Angew. Chem. Int. Ed.* **2014**, *53*, 1804.

[165] Bruker Daltonik GmbH, „esquire series HCT series: User Manual – Volume 1 Theory, Bremen, **2008**.

[166] R. Rahrt, K. Koszinowski, *Protonation of Organometallics Dataverse*, URL: https://data.goettingen-research-online.de/dataverse/rahrt-01, **2023**.

[167] M. D. Hanwell, D. E. Curtis, D. C. Lonie, T. Vandermeersch, E. Zurek, G. R. Hutchison, *J. Cheminform.* **2012**, *4*, 17.

[168] a) S. Grimme, *J. Chem. Theory Comput.* **2019**, *15*, 2847; b) P. Pracht, F. Bohle, S. Grimme, *Phys. Chem. Chem. Phys.* **2020**, *22*, 7169.

[169] J. G. Hill, J. A. Platts, *J. Chem. Phys.* **2008**, *128*, 44104.

[170] K. F. Lim, *Program Colrate*, **1989**.